

SYNTHESIS AND CHARACTERIZATION OF $\text{TlNi}_{1+x}\text{Sn}$
THERMOELECTRIC ALLOYS

by

JACOB STEELE YOUNG

RAMANA G. REDDY, COMMITTEE CHAIR
MARK WEAVER
DANIEL FONSECA

A THESIS

Submitted in partial fulfillment of the requirements
for the degree of Master of Science in the
Department of Metallurgical and Materials Engineering
in the Graduate School of
The University of Alabama

TUSCALOOSA, ALABAMA

2017

Copyright Jacob Steele Young 2017
ALL RIGHTS RESERVED

ABSTRACT

Thermoelectric materials, a unique semiconductor-like class of materials, can convert waste heat into electricity and vice versa. An investigation into the synthesis and characterization of half-Heusler $\text{TiNi}_{1+x}\text{Sn}$ alloys was conducted. An arc-melting and annealing procedure was conducted to achieve the desired phase equilibrium. Additional Ni was added as an interstitial dopant to form a small amount of full-Heusler TiNi_2Sn phase, which has been seen to improve upon thermoelectric properties in the literature. Annealing time (0 to 21 days), annealing temperature (700 to 900 °C), and nickel content ($x = 0, 0.15$) were investigated as key synthesis parameters. Results illustrate that before annealing, many binary and ternary phases are present. The final phase distribution after annealing, a two-phase mixture containing TiNiSn and TiNi_2Sn , was analyzed using XRD, SEM, EBSD, and EDS techniques. The electrical conductivity (1515 to 1618 S cm^{-1} from 30 to 340 °C), Seebeck coefficient (-25 to -53 $\mu\text{V K}^{-1}$ from 30 to 414 °C), thermal conductivity (6.68 to 6.90 $\text{W m}^{-1} \text{K}^{-1}$ from 318 to 414 °C), and thermoelectric figure of merit, ZT, (0.009 to 0.046 from 30 to 430 °C) of single phase TiNiSn using the arc-melting and annealing synthesis method was measured and compared to other methods found in literature. The lattice constants of TiNiSn and TiNi_2Sn as a function of annealing time, annealing temperature, and composition were calculated based on XRD and deviated slightly from the ICDD standards due to Ni-defect behavior (TiNiSn : +0.04 to 0.47% deviation, TiNi_2Sn : -0.09 to -0.40%). The activation energy for conduction (bandgap) of TiNiSn was derived from the measured electrical conductivity and was approximately 0 eV, implying a

metallic conduction behavior. Optimum annealing conditions were determined in order to achieve phase equilibrium with minimum time (14 to 21 days) and temperature required (700°C).

ACKNOWLEDGMENTS

I am pleased to express my heartfelt thanks to my advisor, Dr. Ramana Reddy. Without his extensive knowledge and consistent support, I could not have completed this work. For their insightful discussions and involvement with resolving issues with my experiments, I would like to acknowledge my group members, both past and present: Malli Bogala, Haoxing Yang, Andy Kim, Yudong Li, Yuxiang Peng, and Muhammad Imam.

I would like to express my appreciation for the financial support from the Department of Metallurgical & Materials Engineering at The University of Alabama and the National Science Foundation Grant No. DMR-1310072.

Finally, I would like to thank my family and friends who have supported me throughout this study.

CONTENTS

ABSTRACT.....	ii
ACKNOWLEDGMENTS	iv
LIST OF TABLES.....	viii
LIST OF FIGURES	ix
CHAPTER 1 INTRODUCTION	1
CHAPTER 2 LITERATURE REVIEW	3
2.1 <i>Thermoelectric Effect</i>	3
2.2 <i>Thermoelectric Properties</i>	4
2.2.1 <i>Electrical Conductivity</i>	4
2.2.2 <i>Seebeck Coefficient</i>	7
2.2.3 <i>Thermal Conductivity</i>	10
2.2.4 <i>Figure of Merit</i>	11
2.3 <i>Thermoelectric Device</i>	11
2.3.1 <i>Material Selection and Criteria</i>	12
2.3.2 <i>Heusler and Half-Heusler Alloys</i>	14

2.3.3 <i>Ti-Ni-Sn System</i>	15
2.4 <i>Current Synthesis Methods</i>	17
2.4.1 <i>Arc Melting</i>	17
2.4.2 <i>Mechanical Alloying</i>	17
2.4.3 <i>Spark Plasma Synthesis</i>	18
2.4.4 <i>Induction Levitation Melting</i>	18
2.4.5 <i>Hot Isostatic Press</i>	19
2.4.6 <i>Microwave Processing</i>	19
2.4.7 <i>Annealing</i>	20
2.4.8 <i>TE Properties vs. Synthesis Processes of TiNiSn Alloys</i>	21
CHAPTER 3 RESEARCH OBJECTIVES	29
CHAPTER 4 EXPERIMENTAL PROCEDURES	30
4.1 <i>Sample Preparation</i>	30
4.1.1 <i>Materials</i>	30
4.1.2 <i>Arc Melting</i>	30
4.1.3 <i>Annealing</i>	31
4.2 <i>Microstructural Characterization Techniques</i>	32
4.2.1 <i>X-Ray Diffraction</i>	32
4.2.2 <i>Scanning Electron Microscopy</i>	33
4.3 <i>Thermoelectric Property Measurement</i>	33

CHAPTER 5 RESULTS AND DISCUSSION.....	34
5.1 Elemental Analysis of $TiNi_{1+x}Sn$ Samples	34
5.2 Effect of Annealing Time for $TiNiSn$ Alloy.....	37
5.3 Effect of Annealing Time for $TiNi_{1.15}Sn$ Alloy	41
5.4 Effect of Annealing Temperature for $TiNiSn$ Alloy	45
5.5 Effect of Annealing Temperature for $TiNi_{1.15}Sn$ Alloy	49
5.6 Lattice Parameter Calculation for $TiNiSn$ and $TiNi_2Sn$ Phases	52
5.7 Ni-defects in $TiNi_{1+x}Sn$ Compounds	56
5.8 Experimental Thermoelectric Properties of $TiNiSn$ Alloy	63
5.9 Bandgap Calculation of Experimental $TiNiSn$	67
CHAPTER 6 CONCLUSIONS	70
REFERENCES	72
APPENDIX A – Lattice Constants	77
APPENDIX B – Final Elemental Compositions	80

LIST OF TABLES

Table 1: Synthesis methods used to make TiNiSn-based alloys.....	22
Table 2: Experimental parameters for arc-melted TiNi _{1+x} Sn sample annealing.....	31
Table 3: Calculated lattice constant (Å) from XRD for TiNiSn ternary phase with X = 0 after annealing at 800 °C.....	77
Table 4: Calculated lattice constants (Å) from XRD for TiNiSn ternary phase at X=0.15 after annealing at 800 °C.....	77
Table 5: Calculated lattice constants (Å) from XRD for TiNi ₂ Sn ternary phase at X=0.15 after annealing at 800 °C.	78
Table 6: Calculated lattice constants (Å) from XRD for TiNiSn ternary phase at X=0 after annealing for 14 days.....	78
Table 7: Calculated lattice constants (Å) from XRD for TiNiSn ternary phase at X=0.15 after annealing for 14 days.....	79
Table 8: Calculated lattice constants (Å) from XRD for TiNi ₂ Sn ternary phase at X=0.15 after annealing for 14 days.....	79
Table 9: Elemental mole fraction from EDS for TiNiSn samples, shown in Figure 13.	80
Table 10: Elemental mole fraction from EDS for TiNi _{1.15} Sn samples, shown in Figure 13.	80

LIST OF FIGURES

Figure 1: Electronic band structure of a metal, semiconductor, and insulator [10].....	5
Figure 2: Effective area, S, and mean path, L, for a fully dense and porous sample [14].....	7
Figure 3: Illustration of Seebeck effect for n-type and p-type materials [16].	8
Figure 4: Example of how Seebeck coefficient changes with doping concentration and temperature with a bandgap of 0.13 eV. Smaller quantity of doping is blue and large amount of doping is red. The dashed line is the Goldsmid-Sharp estimation [18].....	9
Figure 5: Typical thermoelectric generator consisting of n- and p-type semiconductors with an applied temperature difference [21].	12
Figure 6: Schematic of the (a) half- and (b) full-Heusler compounds [26].	14
Figure 7: Ti-Ni-Sn ternary phase diagram with solidus projection lines and corresponding temperatures [28]. Black regions are single phase, white are binary regions, and grey are ternary regions.	16
Figure 8: Electrical conductivity of TiNiSn as a function of temperature and synthesis method – (1) BM-SPS [31], (2) AM-AN [38], (3) AM-G-HP-AN [38], (4) CP-AM-AN1-AN2-BM-HP [39], (5) CP-MW-BM-HP [39], (6) AM-AN-BM-SPS [33], (7) AM-AN1-BM-SPS-AN2 [33], (8) IL-AN1-AN2 [35], (9) IL-AN1-AN2 (TiNi _{1.15} Sn) [35].	24
Figure 9: Seebeck coefficient of TiNiSn as a function of temperature and synthesis method – (1) BM-SPS [31], (2) AM-AN [38], (3) AM-G-HP-AN [38], (4) CP-AM-AN1-AN2-BM-HP [39], (5) CP-MW-BM-HP [39], (6) AM-AN-BM-SPS [33], (7) AM-AN1-BM-SPS-AN2 [33], (8) IL-AN1-AN2 [35], (9) IL-AN1-AN2 (TiNi _{1.15} Sn) [35].	25
Figure 10: Thermal conductivity of TiNiSn as a function of temperature and synthesis method – (1) BM-SPS [31], (2) AM-AN [38], (3) AM-G-HP-AN [38], (4) CP-AM-AN1-AN2-BM-HP [39], (5) CP-MW-BM-HP [39], (6) AM-AN-BM-SPS [33], (7) AM-AN1-BM-SPS-AN2 [33], (8) IL-AN1-AN2 [35], (9) IL-AN1-AN2 (TiNi _{1.15} Sn) [35].	26
Figure 11: Figure of merit of TiNiSn as a function of temperature and synthesis method – (1) BM-SPS [31], (2) AM-AN [38], (3) AM-G-HP-AN [38], (4) CP-AM-AN1-AN2-BM-HP [39], (5) CP-MW-BM-HP [39], (6) AM-AN-BM-SPS [33], (7) AM-AN1-BM-SPS-AN2 [33], (8) IL-AN1-AN2 [35], (9) IL-AN1-AN2 (TiNi _{1.15} Sn) [35].	27

Figure 12: (a) Horizontal furnace profile and (b) measured temperature profile at a set point of 800 °C.	32
Figure 13: (a) Complete phase diagram with all 12 sample compositions; (b) Phase diagram section including samples where $x = 0$ and (c) phase diagram section including samples where $x = 0.15$. For (b) and (c), black diamonds are sample conditions 0-5 (Table 2), red circles ‘a’ and ‘b’ are target elemental compositions TiNiSn and TiNi _{1.15} Sn.	36
Figure 14: XRD (Co K α) of TiNiSn alloy annealed at 800 °C for (a) 0 days; (b) 7 days; (c) 14 days; (d) 21 days.	37
Figure 15: Mole fraction of phases present in TiNiSn alloy after annealing at 800 °C for different durations.	38
Figure 16: SEM/EBSD images of TiNiSn alloy samples annealed at 800 °C for (a) 0 days; (b) 7 days; (c) 14 days; (d) 21 days. Gray regions are a mixture of TiNiSn and TiNi ₂ Sn while impurity phases are highlighted.	39
Figure 17: EDS of Ni K α of TiNiSn alloy samples annealed at 800 °C for (a) 0 days; (b) 7 days; (c) 14 days; (d) 21 days, corresponding to SEM images in Figure 18. Bright gray regions are Ni-rich (TiNi ₂ Sn), while darker-gray is TiNiSn and black is void of Ni.	40
Figure 18: XRD (Co K α) of TiNi _{1.15} Sn alloy annealed at 800 °C for (a) 0 days; (b) 7 days; (c) 14 days; (d) 21 days.	41
Figure 19: Mole fraction of phases present in TiNi _{1.15} Sn alloy after annealing at 800 °C for different durations.	42
Figure 20: SEM/EBSD images of TiNi _{1.15} Sn alloy samples annealed at 800 °C for (a) 0 days; (b) 7 days; (c) 14 days; (d) 21 days. Gray regions are a mixture of TiNiSn and TiNi ₂ Sn while impurity phases are highlighted.	43
Figure 21: EDS of Ni K α of TiNi _{1.15} Sn alloy samples annealed at 800 °C for (a) 0 days; (b) 7 days; (c) 14 days; (d) 21 days, corresponding to SEM images in Figure 22. Bright gray regions are Ni-rich (TiNi ₂ Sn), while darker-gray is TiNiSn and black is void of Ni.	44
Figure 22: XRD (Co K α) of TiNiSn alloy samples annealed for 14 days at (a) 700 °C; (b) 800 °C; (c) 900 °C.	45
Figure 23: Mole fraction of phases present in TiNiSn alloy after annealing for 14 days at different temperatures.	46
Figure 24: SEM/EBSD images of TiNiSn alloy samples annealed for 14 days at (a) 700 °C; (b) 800 °C; (c) 900 °C. Gray regions are a mixture of TiNiSn and TiNi ₂ Sn while impurity phases are highlighted.	47

Figure 25: EDS of Ni $K\alpha$ of TiNiSn alloy samples annealed for 14 days at (a) 700 °C; (b) 800 °C; (c) 900 °C, corresponding to SEM images in Figure 26. Bright gray regions are Ni-rich (TiNi ₂ Sn), while darker-gray is TiNiSn and black is void of Ni.	48
Figure 26: XRD (Co $K\alpha$) of TiNi _{1.15} Sn alloy samples annealed for 14 days at (a) 700 °C; (b) 800 °C; (c) 900 °C.....	49
Figure 27: Mole fraction of phases present in TiNi _{1.15} Sn alloy after annealing for 14 days at different temperatures.	50
Figure 28: SEM/EBSD images of TiNi _{1.15} Sn alloy samples annealed for 14 days at (a) 700 °C; (b) 800 °C; (c) 900 °C. Gray regions are a mixture of TiNiSn and TiNi ₂ Sn while impurity phases are highlighted.....	51
Figure 29: EDS of Ni $K\alpha$ of TiNi _{1.15} Sn alloy samples annealed for 14 days at (a) 700 °C; (b) 800 °C; (c) 900 °C, corresponding to SEM images in Figure 30. Bright gray regions are Ni-rich (TiNi ₂ Sn), while darker-gray is TiNiSn and black is void of Ni.....	52
Figure 30: Theta differences for XRD of (220) plane for TiNiSn phase in (a) TiNiSn alloy with annealing duration; (b) TiNiSn alloy with annealing temperature; (c) TiNi _{1.15} Sn alloy with annealing duration; (d) TiNi _{1.15} Sn alloy with annealing temperature.....	53
Figure 31: Theta differences for XRD of (220) plane for TiNi ₂ Sn phase in TiNi _{1.15} Sn alloy (a) with annealing duration; (b) with annealing temperature.....	54
Figure 32: Changes in lattice constant with increasing annealing duration at 800 °C calculated from XRD.	55
Figure 33: Changes in lattice constant with annealing temperature for two weeks calculated from XRD.	56
Figure 34: DFT values of the enthalpy of formation (ΔH_f) at T = 0 K for TiNi _{1+x} Sn compounds [28].	57
Figure 35: Defect formation energy and lattice parameter change of a TiNiSn perfect crystal for defect models: (1) Point defect at Sn-site, (2) Point defect at Ti-site, (3) Substitution of Ni for Ti atom, (4) Substitution of Ni for Sn atom, (5) Interstitial Ni atom in natural vacancy [46].	59
Figure 36: Difference in energy of Ni interstitial defect configuration from random distribution in 2x2x2, 96+n atom, TiNi _{1+x} Sn supercell where n = 4 [47].....	60
Figure 37: Free energy of formation of ordered TiNiSn and disordered Ti(Vacancy) _{1-x} Ni _{1+x} Sn solid solution at T = 1027 °C. The dotted line is the tangent line for composition equilibrium, c_{eq} [48].	61
Figure 38: Binary phase diagram illustrating the stability of TiNiSn and disordered Ti(Vacancy) _{1-x} Ni _{1+x} Sn [48].	62

Figure 39: Experimental electrical conductivity of TiNiSn annealed for 3 weeks at 800 °C..... 63

Figure 40: Experimental Seebeck coefficient of TiNiSn annealed for 3 weeks at 800 °C..... 64

Figure 41: Experimental thermal conductivity of TiNiSn annealed for 3 weeks at 800 °C..... 65

Figure 42: Calculated figure of merit of TiNiSn annealed for 3 weeks at 800 °C. 66

Figure 43: Linear relationship between $\ln(\sigma)$ and $1/T$ for bandgap determination. 68

CHAPTER 1 INTRODUCTION

In 2016, about 65% of the electricity in the United States was generated from thermal energy of power plants using fossil fuels (coal, natural gas, and petroleum), 20% from nuclear sources, and 15% from renewable energy sources [1]. Up to 50% of the energy input can be lost as waste heat during the energy generation process [2]. There is a huge demand to develop renewable technologies that can utilize the abundant wasted thermal energy and convert it into electricity. In recent years, the renewed interest in thermoelectric (TE) materials has been driven by environmental concerns caused by global warming and a strong need to develop alternative energy sources from fossil fuels [3]. TE materials are an attractive alternative energy source since they only require a temperature difference to generate power and have no moving parts, making them less prone to failure. Current TE devices are limited by their low power conversion efficiencies.

Most research regarding thermoelectric devices is within the fields of power generation and electronic refrigeration. Improvements on these technologies are geared toward reducing thermal conductivity within the lattice and improving the power factor and energy conversion efficiency. Additionally, there has been an increased activity toward producing TE materials that can be used in high temperature environments. The primary courses of research to develop these materials are through novel alloy development or improvement (doping) of current known alloys.

Thermoelectric applications for power-generation and energy recovery are being investigated by the automotive industry as a way to convert waste engine heat and improve fuel efficiency. Only about 25% of the fuel energy in a vehicle is used, while the remainder is lost via waste heat from the exhaust and coolant, friction, drag, and wheel misalignment [4]. Additionally, the amount of electronic features (navigation systems, collision-avoidance systems, stability control, vehicle safety features) in current vehicles increases over time, requiring additional electrical power. Small thermoelectric luxury features are already being included in vehicles such as seat and beverage heating and cooling. Major benefits of adding thermoelectric devices to automobiles are greenhouse gas elimination, silent operation, increased energy efficiency, and a potential reduction in weight [5].

Thermoelectric materials are also being investigated for more efficient large-scale refrigeration and localized cooling. In general, the use of thermoelectric modules as cooling devices is currently far more common than the power-generators [6]. Modern TE cooling devices are used in small scale applications, primarily within electronic structures, where the benefits of solid state cooling outweigh any performance and cost limitations. TE devices are not used for large-scale cooling due to their comparatively low efficiencies, high cost per watt of cooling, and higher developmental cost when compared to current refrigeration technologies.

CHAPTER 2 LITERATURE REVIEW

2.1 Thermoelectric Effect

Thermoelectric (TE) materials are a class of materials being investigated thoroughly that has the unique capability of converting thermal energy into electricity (current) and vice versa. Current thermoelectric technology is limited in its application due to low energy conversion efficiencies, higher development costs, and low usability in high temperatures. This conversion phenomenon, known as the thermoelectric effect, is defined by three separate effects discovered from 1821 to 1851: the Seebeck effect, Peltier effect, and Thomson effect.

The Seebeck effect, named after German physicist Thomas Johann Seebeck, is the conversion of a temperature difference into electricity. It was discovered when Seebeck connected two dissimilar metals into a series circuit and observed a compass needle being deflected [7]. A voltage, the thermoelectric electromotive force (EMF), is produced which in turn causes a current loop and a magnetic field. The Seebeck coefficient is a value describing the magnitude of the voltage induced by the Seebeck effect and is the primary material property for determining the effectiveness of a thermoelectric device.

The Peltier effect is the opposite of the Seebeck effect: an applied potential difference (and therefore a current) on two connected dissimilar metals can produce a temperature difference [8]. Heating or cooling of the junctions depends upon the direction of the current flow and can therefore be controlled by the polarity of the current. The Peltier effect is commonly

used for thermoelectric cooling in refrigeration, computer components, and heat sinks because it can cool an object with a solid-state process.

The Thomson effect concludes that the sources of EMF exist in the thermoelectric circuit in addition to those at the junctions of connected metals. William Thomson found that an EMF could be observed within a single conductor with an applied temperature gradient. Therefore, any conductor carrying a current could be heated or cooled with a temperature difference applied between two points. Absorption of heat is evidence for an EMF that is in the same direction as the current flow. Simply put, electrical energy is being supplied to the circuit at the expense of heat energy of the environment [9]. The emission of heat occurs when the EMF is opposed by the current, which transforms electrical energy into heat energy.

2.2 Thermoelectric Properties

2.2.1 Electrical Conductivity

Electrical conductance is determined by the electronic structure of a material, also known as the band structure, shown in Figure 1.

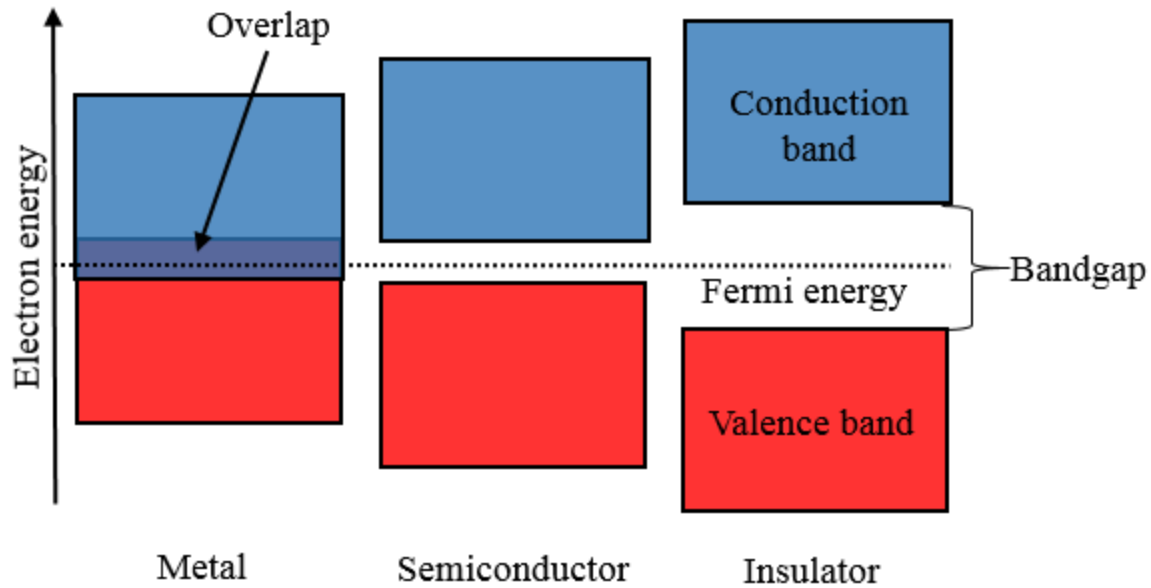


Figure 1: Electronic band structure of a metal, semiconductor, and insulator [10].

An energy band is a range of energy in which an electron is allowed to have, while a band gap is a forbidden energy range. The valence band is the highest energy band completely filled with electrons and is stable at absolute zero temperature. The conduction band, either empty or partially filled with electrons, is the energy state in which electrons can move freely through the material [11]. These bands are separated by the band gap which is an amount of energy, E_g . The number of electrons, N_c , in the conduction band is directly related to the frequency, f , for electrons to move bands [12]:

$$f \sim e^{\left(-\frac{E_g}{kT}\right)}.$$

Insulators, such as ceramic materials (e.g. 5.47 eV for diamond [13]), have a large band gap and empty conduction band which means that large temperatures, T , is needed for promotion of electrons to the conduction band. Metals are excellent conductors due to an overlap of the valence and conduction bands, which allows for a portion of the valence electrons to move freely through the material with no thermal activation required.

Semiconductors have a partially filled conduction band and a small band gap (e.g. 0.67 – 1.11 eV for SiGe [13]). At 0 K, there are no electrons in the conduction band, but at higher temperatures there is a finite number of electrons contributing to conduction which can be estimated based on the Fermi level of the material. Semiconductors are also characterized by a strong increase of conductivity with increasing temperature due to their small band gap. A small energy gap requires less thermal energy for electrons to become activated into the conduction band.

Doping with impurities can drastically increase the conductance of a semiconductor by decreasing E_g . Additionally, impurities can heighten the amounts of positive or negative charge carriers (holes or electrons). When an electron is promoted to the conduction band through thermal activation, the vacancy created in the valence band is a “hole,” which is a positive charge carrier and contributes to electrical conductivity. Doping with impurities eliminates the natural balance between positive and negative charge carriers by introducing additional holes or electrons that can be created or transferred. *P*-type semiconductors are doped with atoms containing fewer valence electrons than the parent atoms, decreasing available free electrons and creating holes, making the majority charge carrier type as positive. *N*-type semiconductors introduce atoms with additional free electrons, which means the majority of charge carriers are negative [12].

Electrical conductivity can also be reduced due to porosity within a sample. As illustrated in Figure 2, porosity increases the length of the mean path as well as reducing the cross sectional area for electrical flow to pass.

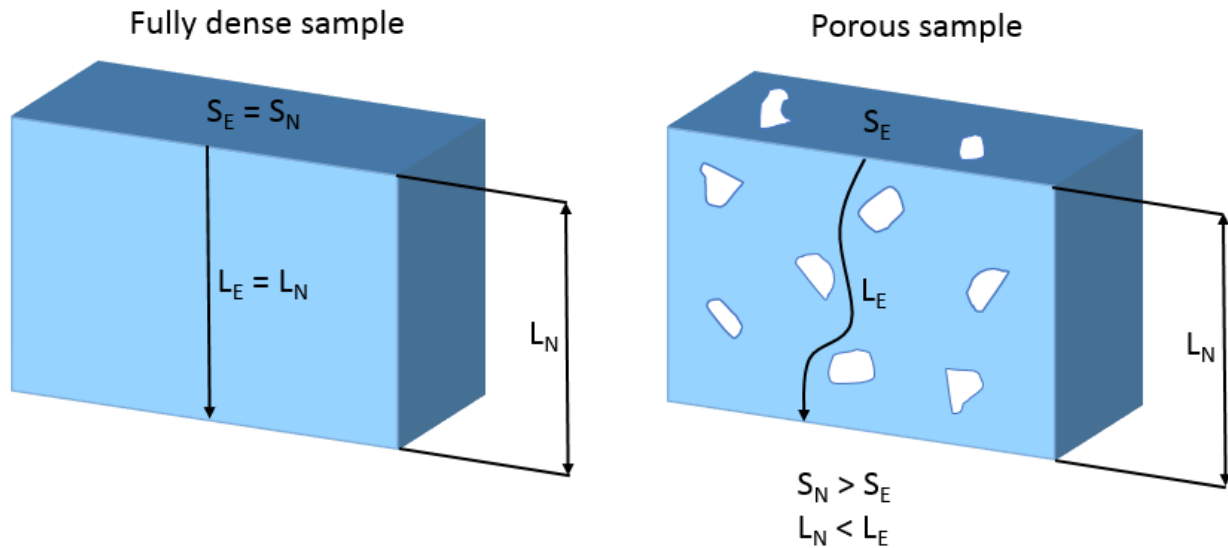


Figure 2: Effective area, S , and mean path, L , for a fully dense and porous sample [14].

Finally, grain size has a pronounced effect on the electrical conductivity of a material. Grain refinement, which reduces the average grain size of a material, can also reduce conductivity as well. Most grain refinement techniques introduce various defects (grain boundaries, dislocations, point defects, etc.) which increase the scattering of conducting electrons, decreasing the electrical conductivity [15].

2.2.2 Seebeck Coefficient

The Seebeck coefficient is a measure of the magnitude of an induced voltage in response to a temperature difference across a material, which is a product of the Seebeck effect. The Seebeck coefficient can be positive or negative depending on the majority type of electric charge carriers (holes or electrons). Ultimately, the Seebeck effect and coefficient is controlled by charge-carrier diffusion, illustrated in Figure 3.

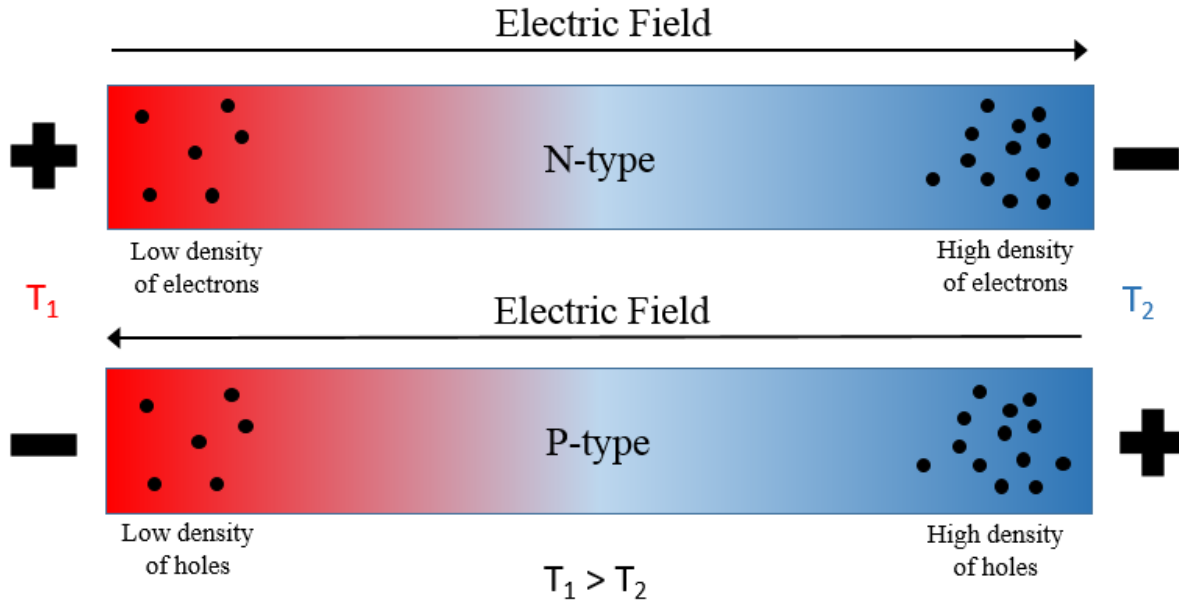


Figure 3: Illustration of Seebeck effect for *n*-type and *p*-type materials [16].

With an applied temperature gradient, charge carriers will move faster from the hot temperature side than those from the colder side. The hot side carriers will therefore diffuse further than the cold carriers, producing a density gradient and a buildup of carriers at the cold end. The buildup of free charge at the cold end produces a repulsive electrostatic force (and therefore an electric potential or voltage) to push the charge pack to the hot end.

Seebeck coefficient can be related to both thermal and electrical conductivities via its relationship to the Lorenz number. The Lorenz number can be estimated using the Seebeck coefficient [17]:

$$L = 1.5 + \exp \left[-\frac{|S|}{116} \right]$$

where L is in $10^{-8} \text{ W}\Omega\text{K}^{-2}$ and S is in $\mu\text{V}/\text{K}$.

The maximum Seebeck coefficient of a semiconductor can be measured as a function of temperature, illustrated in Figure 4.

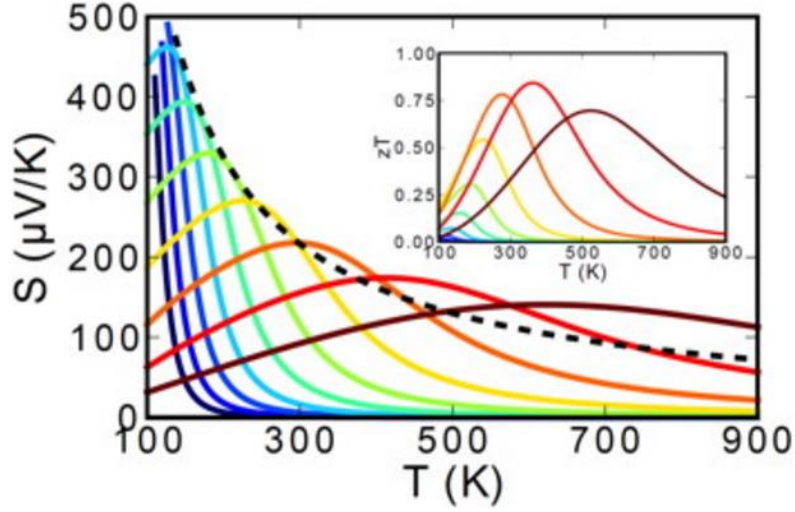


Figure 4: Example of how Seebeck coefficient changes with doping concentration and temperature with a bandgap of 0.13 eV. Smaller quantity of doping is blue and large amount of doping is red. The dashed line is the Goldsmid-Sharp estimation [18].

Additionally, the overall contribution to Seebeck coefficient by positive and negative charge carriers can be defined as a function of electrical conductivity [18]:

$$S = \frac{\sigma_p S_p - \sigma_n |S_n|}{\sigma_p + \sigma_n}$$

For a doped semiconductor, either electrons (p) or holes (n) will be the minority charge carrier. At low temperatures, the ratio of majority to minority carriers promoted into the conduction band will be large, creating a large Seebeck coefficient. At elevated temperatures, the minority carrier conductivity will increase, producing both n- and p-type carriers in the conduction band, which results in a peak and ultimate reduction in Seebeck coefficient. The combination of carriers interferes with each other and reduces $|S|$. Regardless of doping concentration, the Goldsmid-Sharp formula provides an estimate of maximum Seebeck coefficient:

$$|S|_{max} = \frac{E_g}{2eT_{max}}$$

Which relates the band gap, E_g , and maximum thermopower, $|S|$, to the temperature at which it occurs, T_{\max} [18]. It is important to note that the estimation can break down when $S_{\max} < 150 \mu\text{V/K}$ in heavily doped samples.

2.2.3 Thermal Conductivity

Temperature gradients applied to a solid material produce a heat flux:

$$\dot{q} = -\lambda \frac{dT}{dx}$$

where \dot{q} is the heat flux density, T is temperature, and λ is thermal conductivity [12]. Thermal conductivity determines how good a material is at transferring heat. The SI unit for thermal conductivity is $\text{W/m} \cdot \text{K}$. Temperature is a measure of the intensity of lattice vibrations. When a thermal gradient exists, a heat flux is caused by the transmission of lattice vibrations (phonons) or free electrons to less excited regions (hot to cold temperatures).

Thermal conduction through the lattice of a crystal is due to the exchange of these high energy vibrations among atoms. Insulators have few freely moving charge carriers (electrons and holes) so thermal conduction almost exclusively occurs through phonon exchange in the lattice. Free electrons contribute to thermal conductivity through the collision of electrons with atoms which absorb the collision energy and transform it into more intense vibrations (higher temperature). In pure metals, the free electron contribution is significantly higher than that of lattice vibrations. Alloys and semiconductors have measurable contributions from both types of transmission.

Thermal conductivity and electrical conductivity have a direct correlation to one another via the Wiedemann-Franz Law [19]:

$$\frac{\lambda}{\sigma} = LT$$

where L is the Lorenz number, which is typically $2.45 \cdot 10^{-8} \text{ W} \cdot \Omega / \text{K}^2$ for all metals. Due to the need to minimize thermal conductivity and maximize electrical conductivity for improving ZT , tuning these properties through carrier concentration is necessary. Additionally, thermal conductivity can be lowered through phonon scattering. Phonon scattering is associated with the reduction in the mean-free path of electrons and is caused by introducing defects into a perfect crystal, such as point defects, dislocations, impurities, and grain boundaries [12].

2.2.4 Figure of Merit

The figure of merit (ZT) of a thermoelectric device is a dimensionless value associated with the performance and efficiency of the conversion from temperature differences to electricity, calculated as [20]:

$$ZT = \frac{S^2 \sigma T}{\kappa}$$

where S , or α , is Seebeck coefficient, σ is electrical conductivity, κ is total thermal conductivity, and T is absolute temperature. As a rule of thumb, both Seebeck coefficient and electrical conductivity must be maximized, while thermal conductivity is minimized in order to obtain the maximum ZT . With higher ZT and larger temperature differences, the conversion efficiency is heightened.

2.3 Thermoelectric Device

Thermoelectric modules are designed for the conversion of thermal and electrical energy in either direction, utilizing either the Seebeck or Peltier effect. This means that thermoelectric devices are primarily used in temperature extremes (refrigerated or waste heat environments).

Figure 5 presents an example of a typical thermoelectric energy recovery device.

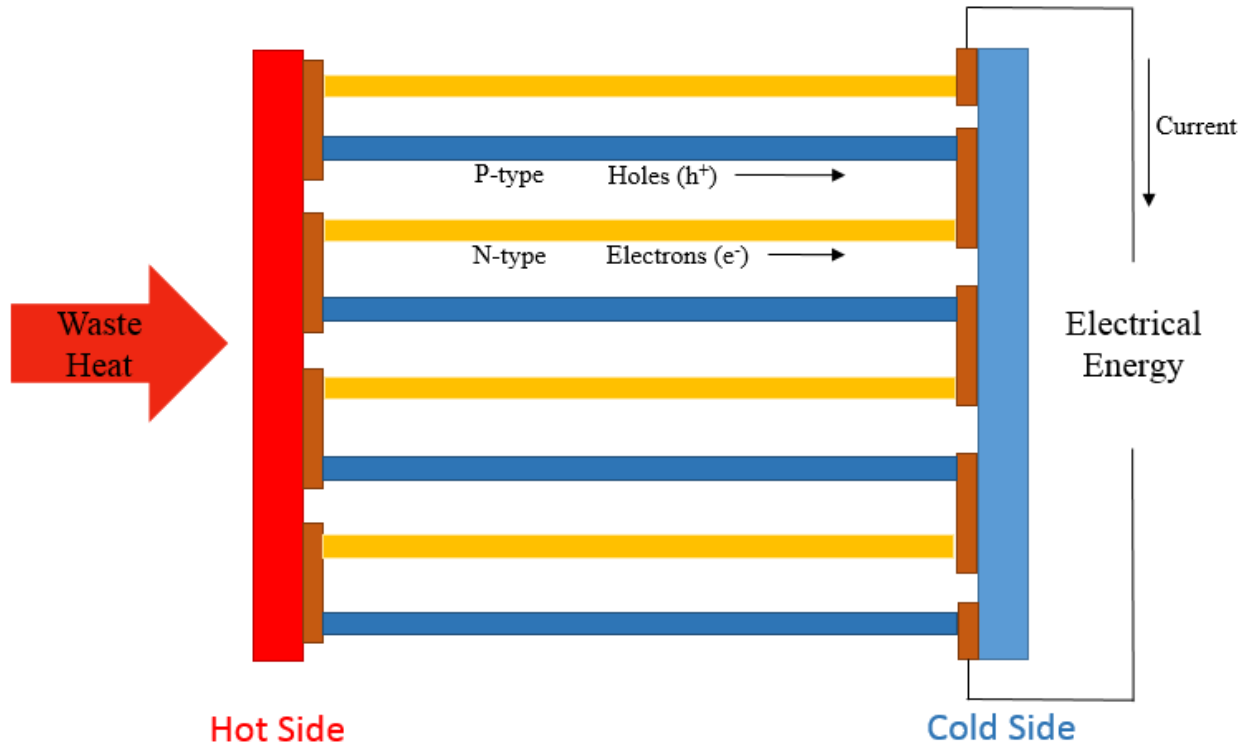


Figure 5: Typical thermoelectric generator consisting of *n*- and *p*-type semiconductors with an applied temperature difference [21].

Multiple pairs of *n*-type and *p*-type semiconductors, arranged in an array, are placed in between electrical conducting substrate plates, often metals such as copper, which connect the pairs together in series. Surrounding the entire device is a ceramic substrate commonly made of alumina. In addition to providing a strong foundation for the device, the ceramic provides excellent thermal and electrical resistivity, which ensures that the temperature difference on each side is stable and not influenced by the device.

2.3.1 Material Selection and Criteria

Thermoelectric devices today have a number of limiting factors that prevent them from being used in commercial applications. The primary focus of modern TE research is improving the low conversion efficiency and raising the power output and density of TE devices, which can be summarized as the continual hunt for higher *ZT*, in order to be commercially viable.

Synthesizing high ZT materials in a laboratory setting is only possible by ignoring cost, environmental consequences, and large-scale preparation ease, which eliminates their potential commercial value. The majority of current TE materials used commercially have low ZT (~1) and are easy to manufacture, such as Bi_2Te_3 , PbTe , and SiGe . In order to be competitive with today's power generation systems, TE devices should have a ZT of 2-4. The promise of increased fuel efficiency in the automotive industry has led to much research by BMW and Ford, which have so far designed a TE generator which provides a 1.2% improvement in efficiency at ~110 kph [22].

A secondary limitation of present TE technology is thermal stability and thermochemical performance at elevated temperatures. Many TE materials studied contain elements with high vapor pressure, such as Pb, Ge, Sb, Sn, and Te, which lead to high sublimation and diffusion rates of atoms, promoting oxidation, dislocation motion, and creep [23]. This reduces the working temperature of many devices. Such elements are also susceptible to the diffusion or reaction to oxygen or nitrogen in the atmosphere at higher temperatures, leading to a degradation of performance. Possible solutions are using an inert atmosphere around the device or doping to improve stability.

Finally, the mechanical properties at elevated temperature are a severe constraint to take into account when designing a TE device. Bi_2Te_3 and PbTe currently have excellent ZT values, but are brittle in nature which reduces their applicability. Strength, hardness, and toughness of a device has to be taken into account for commercial applications. TE devices need to have a sufficiently high strength and stiffness (Young's modulus) in order to prevent surface defects, such as chipping and fracture, during the manufacturing process. Moderate hardness is necessary to prevent surface damage during handling and use. Last, high thermal toughness is

required to prevent failure from thermal fatigue or shock during the inevitable thermal cycling experienced during a device's lifetime. Improving mechanical properties while maintaining a high ZT can be challenging because of the inverse relationships between many mechanical, electrical, and thermal properties [24].

2.3.2 Heusler and Half-Heusler Alloys

Originally studied and named by Friedrich Heusler in 1903, Heusler-structured alloys are a class of intermetallic ferromagnetic materials that exhibit a plethora of magnetic qualities as well as shape-memory effects. Additionally, half-Heusler alloys show many similarities to semiconductors due to their band gap around the Fermi level, which provides a lower thermal conductivity and large Seebeck coefficient [25]. Pictured in Figure 6, Heusler alloys consist of four interpenetrating fcc sublattices with the formula X_2YZ , where X and Y are transition metals and Z is a main group element. Half-Heusler alloys leave one of the X sublattices unoccupied as structural vacancies.

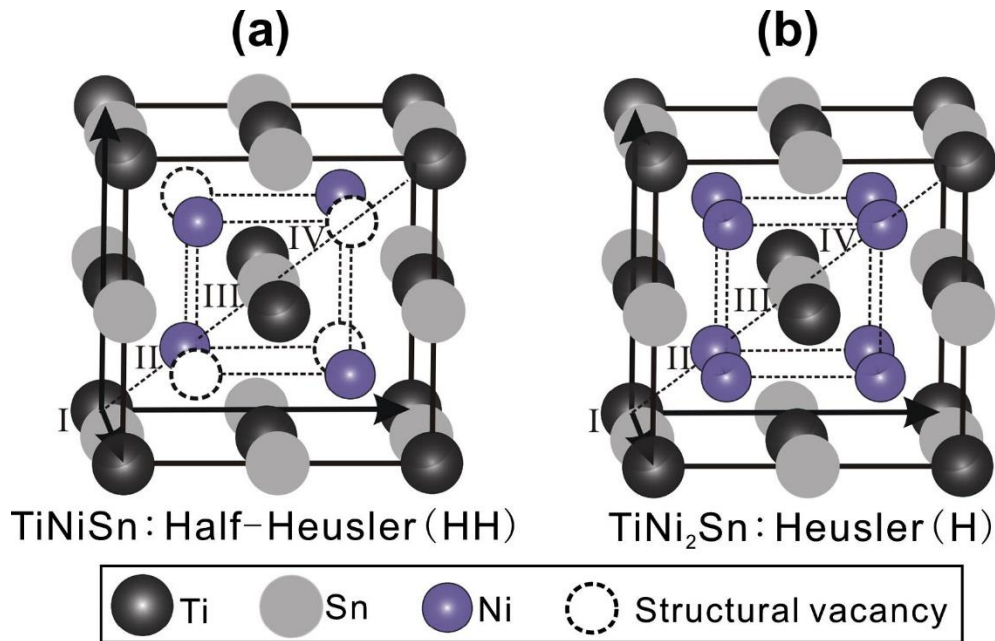


Figure 6: Schematic of the (a) half- and (b) full-Heusler compounds [26].

Half-Heusler (HH) alloys are a primary focus of thermoelectric materials research for high temperature energy generation applications. They have high mechanical strength, thermal stability, electrical conductivity, and average Seebeck coefficient when compared to other thermoelectric materials. Additionally, the natural vacancies within the unit cell favor doping and substitution of either impurity or parent elements, strengthening the electronic properties. Half-Heusler alloys contain non-toxic, less expensive elements with high melting points such as Ti, Ni, Hf, Zr, Mn, and Fe as well as low melting point elements such as Sn, Sb, and Al. Synthesis of HH materials requires a high temperature process. A general procedure used for most HH alloys is a melt, such as arc-melting or induction-levitation melting, followed by a secondary heat treatment anneal in order to produce a single phase material. Densification using hot isostatic pressing (HIP) or spark plasma synthesis (SPS) is often implemented in order to reduce the quantity of porosity and for grain refinement [27].

2.3.3 Ti-Ni-Sn System

TiNiSn-based half-Heusler compounds have been a research focus for potential thermoelectric materials due to their excellent thermal stability, non-toxicity, high ZT at elevated temperatures, and impurity doping ease through vacancy or substitution defects. The phase diagram of the Ti-Ni-Sn ternary system is shown in Figure 7.

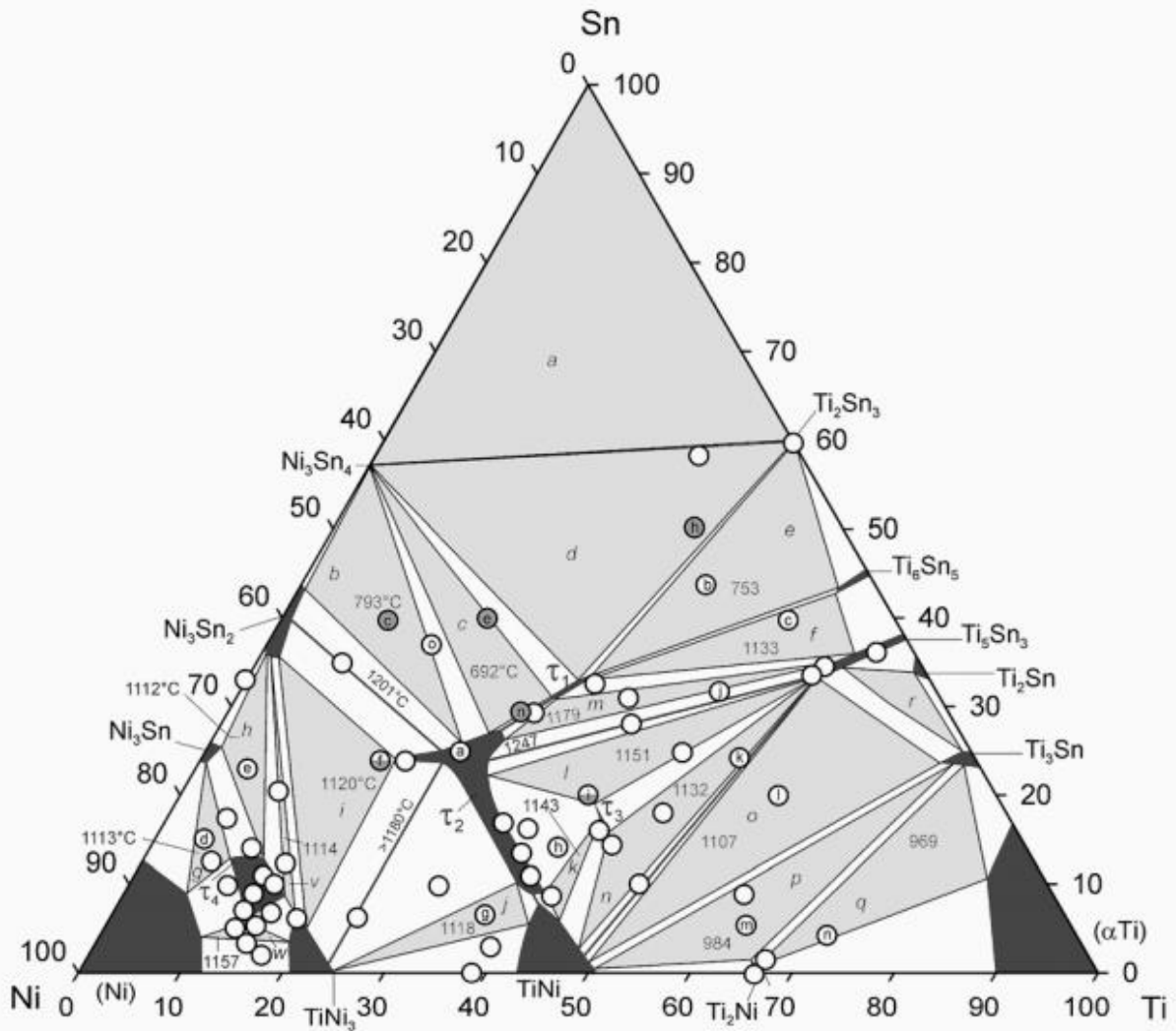


Figure 7: Ti-Ni-Sn ternary phase diagram with solidus projection lines and corresponding temperatures [28]. Black regions are single phase, white are binary regions, and grey are ternary regions.

The Ti-Ni-Sn system has four stable single phase ternary alloys, labeled τ_1 to τ_4 . Two ternary compounds, τ_1 (TiNiSn) and τ_3 (Ti₂Ni₂Sn), have small homogeneity regions while τ_2 (Ti_{1+y}Ni_{2-x}Sn_{1-y}) and τ_4 ((Ti_{1-x-y}Sn_xNi_y)Ni₃) contain large solid solution ranges. The largest field of crystallization belongs to τ_2 , the Heusler phase, which melts congruently at 1447 °C [29] has an extended homogeneity range toward Ni₃Sn₂, TiNi, and τ_1 , the half-Heusler phase. The half-Heusler phase melts incongruently by the reaction $l + \tau_2 \leftrightarrow \tau_1$ at 1180 °C and its small

homogeneity region tends toward the Heusler phase based on its solubility with Ni. Therefore, Sn-rich samples near this single phase regions will contain small amounts of nearby binary phases, such as Ti_5Sn_3 or Ti_6Sn_5 .

2.4 Current Synthesis Methods

2.4.1 Arc Melting

Vacuum arc melting is a primary method used for melting metals in order to form alloys. In a laboratory setting, a tungsten inert gas (TIG) welding unit is used to provide power to an electrode. An arc is struck between the electrode (typically tungsten) and the sample on a water-cooled copper hearth. The electric arc generates a large amount of heat concentrated near the sample, which melts the metal together into an ingot or pellet. Chamber evacuation and backfill with argon gas prevent unwanted oxidation of the sample while molten. Often an oxygen getter (titanium) is used as a secondary method to preemptively react trace amounts of O_2 . Repeated melting and flipping of the sample improves the phase homogeneity of the final alloy, but small localized regions of elemental non-homogeneity is common.

2.4.2 Mechanical Alloying

Mechanical alloying (MA) is a solid state process in which powder is constantly welded together and fractured in a rotating ball mill, which provides an extremely high energy environment. This process is used to synthesize both equilibrium and non-equilibrium (metastable) phases from elemental powders. Mechanical alloying can also be used to form compounds that prove troublesome to use with other methods, such as multiple elements with large melting point differences or volatile elements with low melting points [30]. Zou et al [31] found that mechanical alloying enhanced the formation of TiNiSn compounds during secondary processes, such as SPS, by forming binary phases from the initial elemental powders. They were

unable to form TiNiSn after 20 hours of mechanical alloying, therefore an additional high temperature process was necessary to form TiNiSn.

2.4.3 Spark Plasma Synthesis

Spark plasma synthesis (SPS), also known as pulsed electric current sintering (PECS), is a method of powder consolidation in which powders are subjected to high pressure and a pulsed DC current simultaneously. This in turn leads to a very high heating rate (up to 1000 K/s), densification of powders, and production of desired phases without excessive grain growth. Munir, Anselmi-Tamburini, and Ohyanagi [32] summarized that grain size decreased with increasing heating rate, while applied pressure increased densification at a given temperature. Also, the pulsed DC current flowed through the sample created the high heating rate and an amount of plasma which provides a cleansing effect on the surface of the sample particles which enhances sintering. Additionally, the applied current decreased the activation energy for defect mobility.

For the formation of TiNiSn phase, SPS has been used to form TiNiSn and eliminate impurity phases, as well as for final densification. Gelbstein et al [33] used SPS after arc melting, annealing, and ball milling in order to synthesize dense samples (>99%) with no lateral cracks.

2.4.4 Induction Levitation Melting

Levitation melting is a technique which melts high melting point alloys without contamination from the crucible material. Electromagnetic forces generated by a coil are used to levitate the molten sample and inductively mix simultaneously. Benefits of this process include prevention of impurities from contacting other materials, negligible temperature differences within the sample, and a thoroughly mixed sample while molten. The primary disadvantage is

the smaller sample quantity that can be melted at one time compared to other methods [34].

Douglas et al [35] synthesized TiNiSn with a small (<3 mol. %) amount of secondary phases (TiNi₂Sn, Ti₆Sn, and Ni₃Sn₄) due to the crystallization path and narrow phase field of TiNiSn.

2.4.5 Hot Isostatic Press

Pressureless sintering is the method of particle fusion in which a powder compact is exposed to an elevated temperature ($2/3 T_m$). Generally, sintering undergoes three stages of geometric change [36]. First, neck growth occurs, which is the increase of interparticle contact area from zero to ~0.2% of the cross-sectional area of the tangential particles. Second, grain growth occurs which causes a transition from individual particles to a pore and grain boundary matrix. Finally, pores are eventually closed due to the growth of grains. When all pores are closed and eliminated, the sample is fully dense. Hot isostatic pressing (HIP) is the sintering of powders at high temperatures with an applied pressure. This combination enhances the driving forces for diffusion and effects of pressureless sintering, such as capillary forces, rearrangement of particles, surface tension, and induced creep and plasticity in the powder sample [37]. Kim et al [38] successfully synthesized TiNiSn-based compounds using arc melting, grinding, HIP, and annealing process. It was found that the thermal conductivities of hot pressed samples were reduced with respect to samples that were just arc melted and annealed.

2.4.6 Microwave Processing

Solid state reactions using microwaves have been used since the 1980s to synthesize metallic, ceramic, and thermoelectric materials. Microwave processing involves the sample material coupling to the microwave radiation, which is termed as its dielectric loss tangent. This coupling enables additional heating within the material, leading to enhanced atom diffusion and

rapid grain growth. Birkel et al [39] created TiNiSn and TiCoSb compounds using microwave processing followed by crushing, ball milling, and SPS for densification.

2.4.7 Annealing

Annealing is a secondary heat treatment process meant to transform the physical and chemical properties of a material to their equilibrium states through the application of heat. The annealing process changes a distorted lattice structure back to a strain-free state and promotes a state of phase equilibrium, all of which occurs at solid state below the melting point. These material changes occur due to an increased rate of atom diffusion due to the heat providing the necessary energy to break bonds. The elimination and redistribution of defects, such as dislocations, reduces the internal strain of a material as well. Annealing can be broken down into three main stages: recovery, recrystallization, and grain growth [40]. All stages of annealing are thermodynamically driven towards equilibrium by reducing the total Gibbs energy within the material structure, whether that's from dislocation, grain boundaries, or free surfaces.

The first stage, recovery, is the interaction and redistribution of dislocations via their stress fields. The deformed state of a material is not in thermodynamic equilibrium, but can be mechanically stable and in equilibrium. Given the application of heat, the mechanical stability can be overcome by the heat activated energy for dislocation movement, moving and annihilating dislocations to minimize the stress and strain in the lattice structure. Since the recovery stage is solely thermally activated, it happens spontaneously and without an incubation time.

After recovery is complete and when the upper temperature range has been reached, recrystallization is initiated. The recrystallization process is the nucleation of new strain-free grains and subsequent growth of these grains to absorb the deformed parent material. There is

usually an incubation period in which energy needs to be stored to allow the strain-free nuclei to reach a critical size [41].

The third and final stage, grain growth, takes place after recovery and crystallization have completed and any additional reduction in internal energy can only be completed by the reduction of the total amount of grain boundary. Large grains promote less grain boundaries and are more thermodynamically stable than smaller grain sizes. Under ideal conditions, the lowest equilibrium energy state for a metal would be a single crystal structure. This reduction in internal energy is the driving force for grain growth, which is balanced by opposing forces such as grain boundary orientation angle, impurities and precipitates, and free surfaces.

2.4.8 TE Properties vs. Synthesis Processes of TiNiSn Alloys

Many synthesis methods for TiNiSn-based alloys have been employed in literature, but there has been no direct comparison published of thermoelectric properties between the processes. Table 1 outlines the parameters used for many of the synthesis methods.

Table 1: Synthesis methods used to make TiNiSn-based alloys.

Method #	Ref.	Synthesis Method	Product	Grain Size
1	[31]	Planetary ball mill (BM) powders at 300 rpm for 2.5 h; SPS at 800-850 °C for 10 min.	TiNiSn	200-400 nm
2	[38]	Arc melt (AM) powders several times; wrapped in Ta foil and annealed (AN) at 800 °C for 336 h.	TiNiSn	-
3	[38]	Arc melt powders; mortar ground (G) and separated under 45 µm; hot-pressed (HP) at 800 °C for 5 h under 35 MPa; annealed at 800 °C for 336 h in evacuated quartz tube.	TiNiSn	-
4	[39]	Cold press (CP) powders; arc melt once; button wrapped in Ta foil; annealed at 900 °C for 24 h; second anneal at 850 °C for 192 h; mortar and ball mill into powder; hot-pressed at 900 °C for 1 h at 84 MPa.	TiNiSn	110 – 130 nm
5	[39]	Cold press powders into bar shape; sealed in evacuated quartz tube; placed in crucible filled with granular carbon; processed in microwave (MW) reactor at 700 W for 1 min; mortar and ball mill into powder; hot-pressed at 900 °C for 1 h at 84 MPa.	TiNiSn	100 – 130 nm

6	[33]	Arc melt powders several times; annealed at 800 C for 72 h and quenched; ball milled for 5 h under argon; SPS at 1050 C for 10 min at 50 MPa.	TiNiSn	~42 μm
7	[33]	Arc melt powders several times; annealed at 800 C for 72 h and quenched; ball milled for 5 h under argon; SPS at 1050 C for 10 min at 50 MPa; annealed at 890 C for 48 h.	TiNiSn	~75 μm
8	[35]	Induction levitation melting (IL) for 120s; ingots wrapped in Ta foil; annealed at 900 C for 24 h; second anneal at 850 C for 192 h.	TiNiSn	-
9	[35]	Induction levitation melting (IL) for 120s; ingots wrapped in Ta foil; annealed at 900 C for 24 h; second anneal at 850 C for 192 h.	TiNi _{1.15} Sn	TiNiSn: 100 nm – 2 μm TiNi ₂ Sn: 20 – 30 μm

Most synthesis methods consist of an initial melting stage, usually arc melting, followed by a heat treatment to produce a single phase alloy. Some synthesis methods employ a densification stage either using hot pressing or SPS in order to eliminate internal voids in the sample and to promote grain refinement. Each of the thermoelectric properties can vary depending on synthesis method. The electrical conductivity of each process is shown in Figure 8.

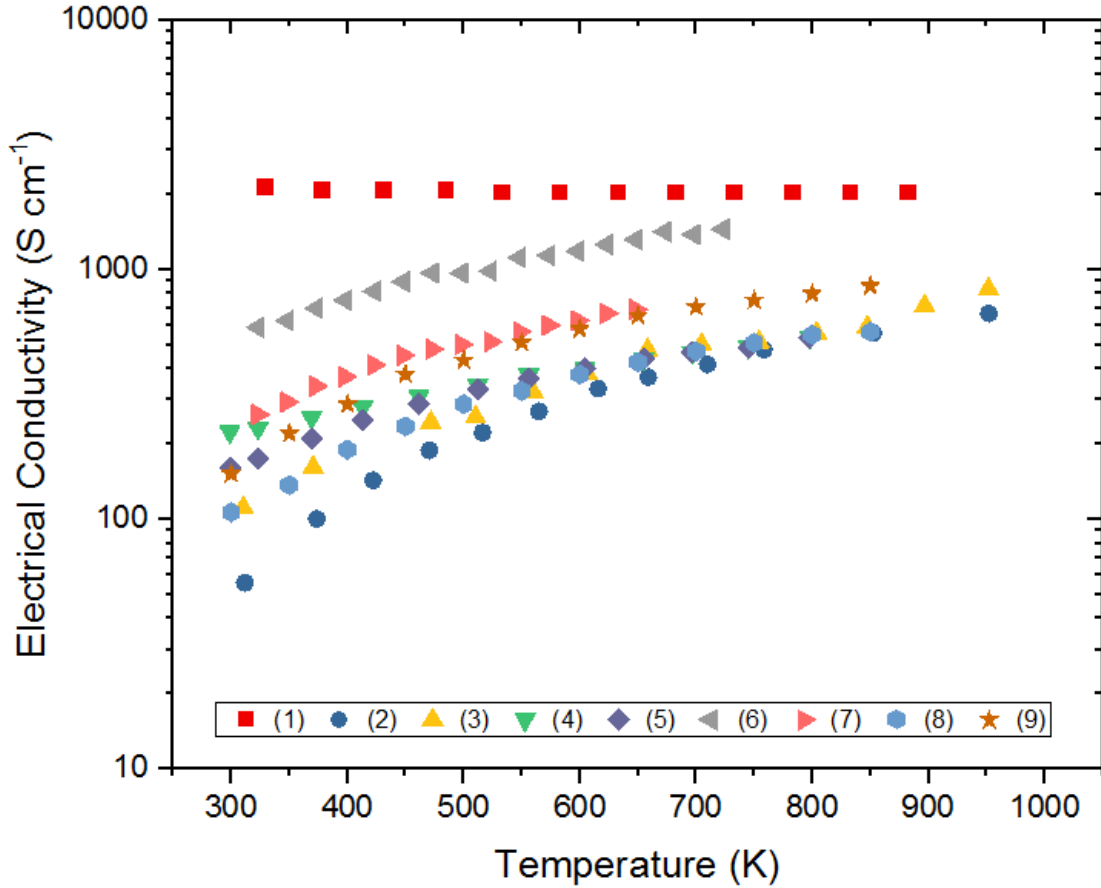


Figure 8: Electrical conductivity of TiNiSn as a function of temperature and synthesis method – (1) BM-SPS [31], (2) AM-AN [38], (3) AM-G-HP-AN [38], (4) CP-AM-AN1-AN2-BM-HP [39], (5) CP-MW-BM-HP [39], (6) AM-AN-BM-SPS [33], (7) AM-AN1-BM-SPS-AN2 [33], (8) IL-AN1-AN2 [35], (9) IL-AN1-AN2 (TiNi_{1.15}Sn) [35].

The electrical conductivity can range over two orders of magnitude dependent upon the synthesis method used. To maximize ZT, the electrical conductivity should be as large as possible. Based on the examples in literature in Table 1, using a densification method, such as SPS or hot pressing, can have benefits toward electrical conductivity by eliminating porosity. It is known that a porous specimen lowers the electrical conductivity of a sample due to a lengthening of the mean path and a smaller mean transfer section, illustrated in Figure 2 above. Conversely, smaller grain sizes, due to shorter duration heat treatments and anneals, have a negative effect on conductivity due to electron scattering at grain boundary defects.

Seebeck coefficient, arguably the most crucial parameter for maximizing ZT due to being squared, varies greatly according to processing parameters and is related to the electrical conductivity. Figure 9 shows the relationship between Seebeck coefficient, synthesis method, and temperature.

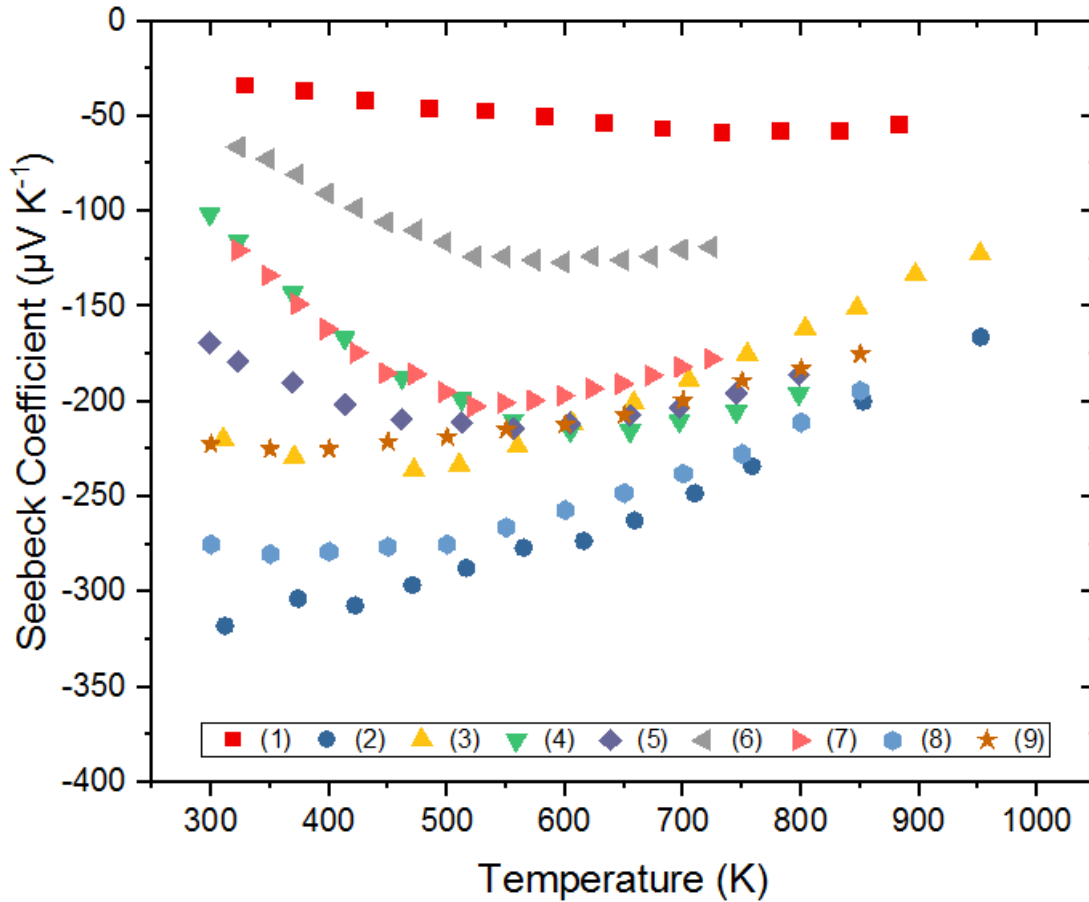


Figure 9: Seebeck coefficient of TiNiSn as a function of temperature and synthesis method – (1) BM-SPS [31], (2) AM-AN [38], (3) AM-G-HP-AN [38], (4) CP-AM-AN1-AN2-BM-HP [39], (5) CP-MW-BM-HP [39], (6) AM-AN-BM-SPS [33], (7) AM-AN1-BM-SPS-AN2 [33], (8) IL-AN1-AN2 [35], (9) IL-AN1-AN2 (TiNi_{1.15}Sn) [35].

From Figures 8 and 9, there is an inverse relationship seen between electrical conductivity and Seebeck coefficient: as conductivity decreases, the magnitude of Seebeck coefficient increases. This relationship can be explained by the effect of bandgap size on both properties. With a large bandgap, a material becomes similar to an insulator with high

resistivity. A large bandgap also only enables the primary charge carrier in a material to excite across the bandgap, leading to a large Seebeck coefficient. As conductivity increases, the bandgap decreases until the material becomes semiconductor-like and finally metallic, promoting both majority and minority charge carrier excitement, which gives a negative impact toward Seebeck coefficient. Densification processes which can eliminate internal defects and porosity in a sample greatly improve the electrical conductivity, at the expense of Seebeck coefficient. It is important to balance the two properties in order to achieve the maximum ZT.

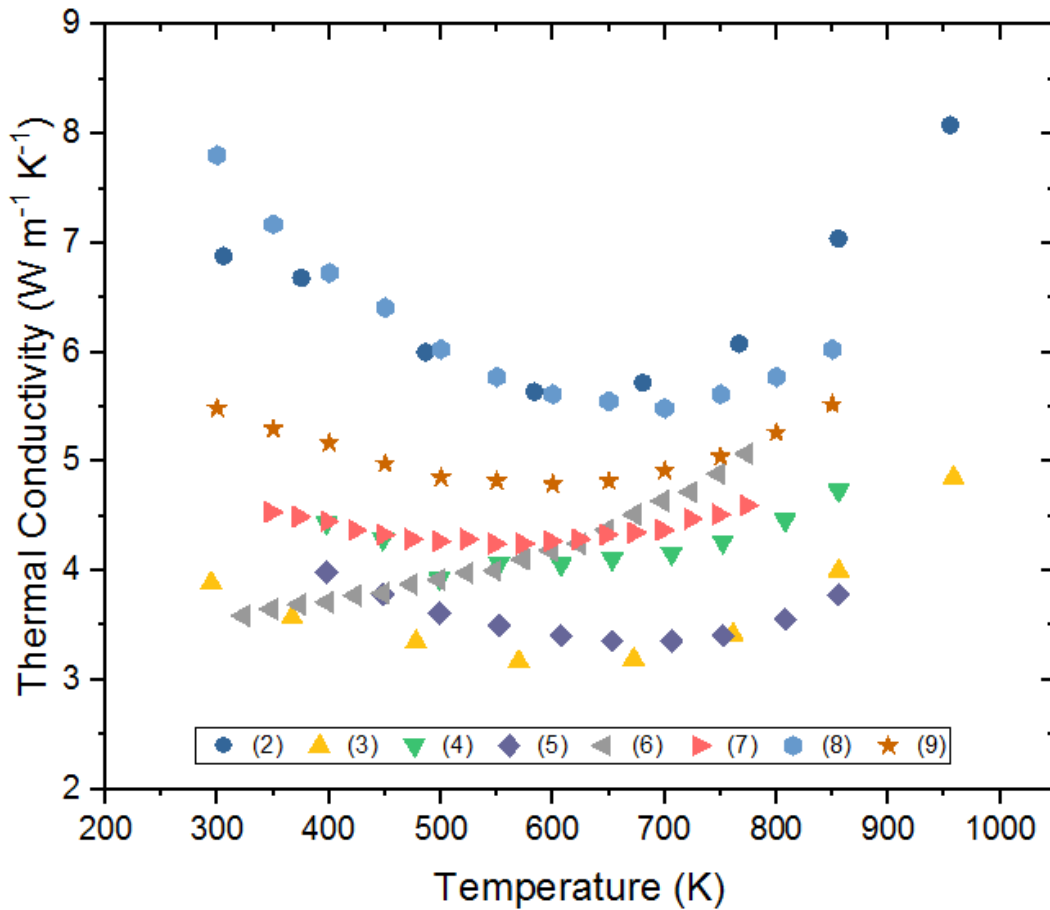


Figure 10: Thermal conductivity of TiNiSn as a function of temperature and synthesis method – (1) BM-SPS [31], (2) AM-AN [38], (3) AM-G-HP-AN [38], (4) CP-AM-AN1-AN2-BM-HP [39], (5) CP-MW-BM-HP [39], (6) AM-AN-BM-SPS [33], (7) AM-AN1-BM-SPS-AN2 [33], (8) IL-AN1-AN2 [35], (9) IL-AN1-AN2 (TiNi_{1.15}Sn) [35].

Thermal conductivity is not nearly as sensitive to synthesis method as electrical conductivity or Seebeck coefficient, shown to only have a range between 3 – 8 W/mK. It is important to note that the majority of pure metals have a conductivity of >20 W/mK. Interestingly, the highest thermal conductivities, literature examples 2, 8, and 9 in Figure 10, occurred when the synthesis procedure included no final densification process to eliminate porosity. Defects are known to reduce thermal conductivity due to an increase in phonon scattering. It is likely that the small variance in thermal conductivity between methods is due to a combination of testing methods, grain size, and final sample density.

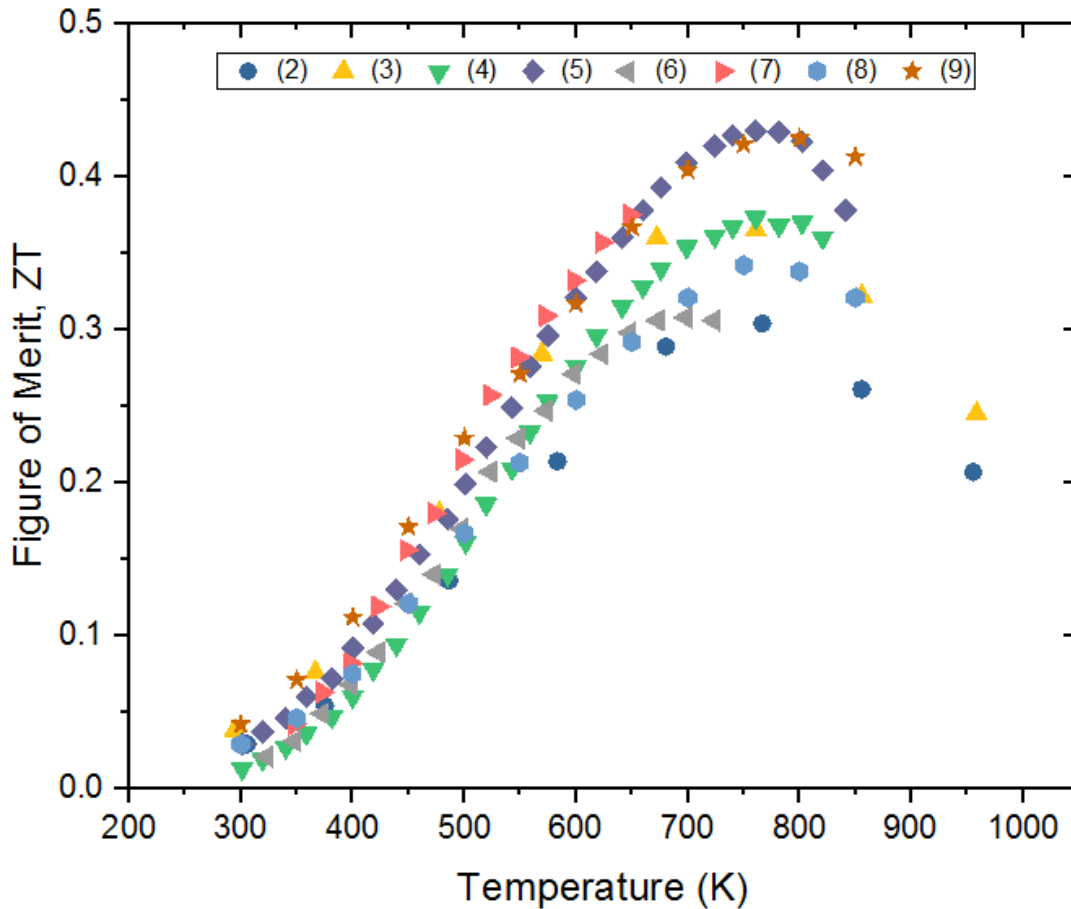


Figure 11: Figure of merit of TiNiSn as a function of temperature and synthesis method – (1) BM-SPS [31], (2) AM-AN [38], (3) AM-G-HP-AN [38], (4) CP-AM-AN1-AN2-BM-HP [39], (5) CP-MW-BM-HP [39], (6) AM-AN-BM-SPS [33], (7) AM-AN1-BM-SPS-AN2 [33], (8) IL-AN1-AN2 [35], (9) IL-AN1-AN2 (TiNi_{1.15}Sn) [35].

The figure of merit, ZT , is a function of electrical conductivity, thermal conductivity, and Seebeck coefficient, as defined in section 2.2.1. Regardless of method, the peak ZT for undoped or Ni-doped TiNiSn alloys was in the range of 600 – 800 K. In general, processes that eliminated porosity, such as by using SPS or hot pressing, produced a higher ZT material. Additionally, n-type doping with Ni to synthesize TiNi_{1.15}Sn using induction levitation melting (IL) had heightened ZT when compared to the identical process for TiNiSn.

CHAPTER 3 RESEARCH OBJECTIVES

The main objective of this research is to contribute to the development of thermoelectric metal alloys with a good figure of merit for high temperature applications. Half-Heusler alloys are a semiconducting class of materials that are being considered for thermoelectric devices in this study. The alloys chosen for this investigation are ternary TiNiSn and TiNi_{1.15}Sn due to their thermal stability, cheaper raw materials, and promising thermoelectric capabilities at high temperatures from literature. This study focuses on the effect of synthesis procedure on phase evolution and thermoelectric properties.

The specific objectives of this research project are:

1. To evaluate modern synthesis methods in literature for making TiNi_{1+x}Sn half-Heusler alloys. Comparison of synthesis methods was done with respect to thermal conductivity, electrical resistivity, Seebeck coefficient, and ZT.
2. To synthesize TiNiSn and TiNi_{1.15}Sn thermoelectric alloys using cold-pressing, arc-melting, and annealing methods. The annealing temperature and time was optimized with respect to phase equilibria. Characterization of phase and grain morphology was completed using XRD, SEM, EBSD, and EDS techniques.
3. To determine and compare the thermoelectric properties of arc-melted and annealed samples of TiNi_{1+x}Sn using a ZT-Scanner instrument for simultaneous Harman-based measurements. Optimization of thermoelectric properties was determined based on synthesis methods and experimental variables.

CHAPTER 4 EXPERIMENTAL PROCEDURES

4.1 Sample Preparation

4.1.1 Materials

Twelve samples using two amounts of nickel ($X=0$ and $X=0.15$) were chosen to investigate the effects of additional nickel content in $\text{TiNi}_{1+x}\text{Sn}$ during the synthesis process and on the final product. The predicted equilibrium phase composition is comprised of TiNiSn and TiNi_2Sn Heusler-type phases. The metal powders used for this experiment were nickel (Alfa Aesar, APS 3-7 micron, 99.9%), titanium (Alfa Aesar ~325 mesh, 99%), and tin (Alfa Aesar, ~325 mesh, 99.8%). Stoichiometric amounts of metal powders were initially mixed in a glass vial using a jar mill for 2 hours to obtain a uniform mixture of Ni, Ti, and Sn. The mixed powder was isostatically cold-pressed at 2 tons for 5 minutes into a cylindrical shape with approximately 3 grams of powder per sample. This was to reduce the scattering of metal powders during initialization of the arc during melting which can decrease phase homogenization.

4.1.2 Arc Melting

The obtained pellets were arc-melted using a small bell jar arc melt furnace (ABJ338, Materials Research Furnaces Inc.) under an ultra-high pure argon atmosphere. The arc furnace consists of a Cu stringer or handle with its inside end attached to a pointed thorium-doped tungsten rod electrode. The sample pellets were placed onto a custom-made cavity of a water cooled ($<50^\circ\text{C}$) copper hearth place (8.5 cm diameter). Prior to the start of the experiment, an evacuation pump (56 LPM) was used to cycle three times between vacuum and 30 mmHg of Ar

to remove any ambient air present within the chamber. A titanium oxygen getter was used to react with any residual oxygen left inside the chamber after evacuation. Under a positive argon pressure of 2 psi and 150 A current, each pressed pellet was melted using an electric plasma arc three times, flipping the button sample between melts to ensure a homogeneous composition of the alloy.

4.1.3 Annealing

A heat treatment process was required after arc melting to produce a state of phase equilibrium for each sample based on the Ti-Ni-Sn ternary phase diagram. Individual arc melted buttons were wrapped with tantalum foil to help prevent oxidation during annealing. Additionally, the foil-wrapped samples were encapsulated within quartz tubes under vacuum. Annealing temperatures from 700 to 900 °C were used for this study in order to compare well with other synthesis methods in literature. The annealing parameters used are shown in Table 2.

Table 2: Experimental parameters for arc-melted $\text{TiNi}_{1+x}\text{Sn}$ sample annealing.

Condition #	Annealing Temperature, °C	Annealing Duration, Weeks
0 (Control)	N/A	0
1	800	1
2	800	2
3	800	3
4	900	2
5	700	2

Temperature measurement within the annealing tube furnace was completed in order to determine the deviation between programmed set point and actual temperature using a

thermocouple. Figure 12 illustrates the horizontal furnace profile as well as the temperature measurements at an 800 °C set point.

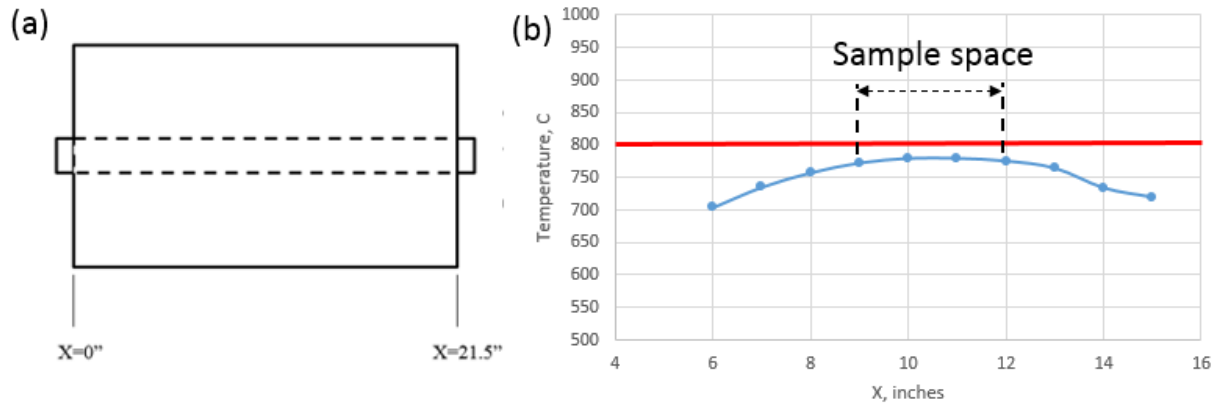


Figure 12: (a) Horizontal furnace profile and (b) measured temperature profile at a set point of 800 °C.

The deviation from set point was found to be -21 to -28 °C for a 3 inch distance in the middle of the furnace. All pellets were annealed within this furnace space in order to minimize temperature variances and to assure the correct annealing conditions for each sample.

4.2 Microstructural Characterization Techniques

4.2.1 X-Ray Diffraction

The annealed products were characterized using the X-ray diffraction (XRD) technique. Each sample pellet was cut in half and mounted using a low-temperature polymer resin. The mounted samples were ground with abrasive papers (SiC papers with grits 60 – 1200). Automatic polishing was completed using multiple diamond suspensions from 9 – 0.5 μm . Phase analysis of the polished samples was done on a Bruker D8 Discover XRD using Co K-alpha radiation at 45 kV and 40 mA. Mole fractions of the phases present was calculated using the Rietveld analysis with TOPAS 4 software.

4.2.2 Scanning Electron Microscopy

Chemical etching of each samples was completed in order to identify any grain boundaries, grain sizes, and phase differences. The samples were swabbed for 30 seconds using Kroll's Reagent (94.5% H₂O, 1.5% HF, and 4% HNO₃). The surface morphology and elemental composition of the polished samples was analyzed using a JEOL 7000 FE scanning electron microscope (SEM) with equipped energy-dispersive X-ray spectroscopy (EDS).

4.3 Thermoelectric Property Measurement

All thermoelectric property measurements of thermal conductivity, electrical conductivity, and Seebeck coefficient for the TiNiSn alloy were measured using a ZT-Scanner instrument for simultaneous Harman-based measurements from TEMTE Inc. in Montreal, Canada [42].

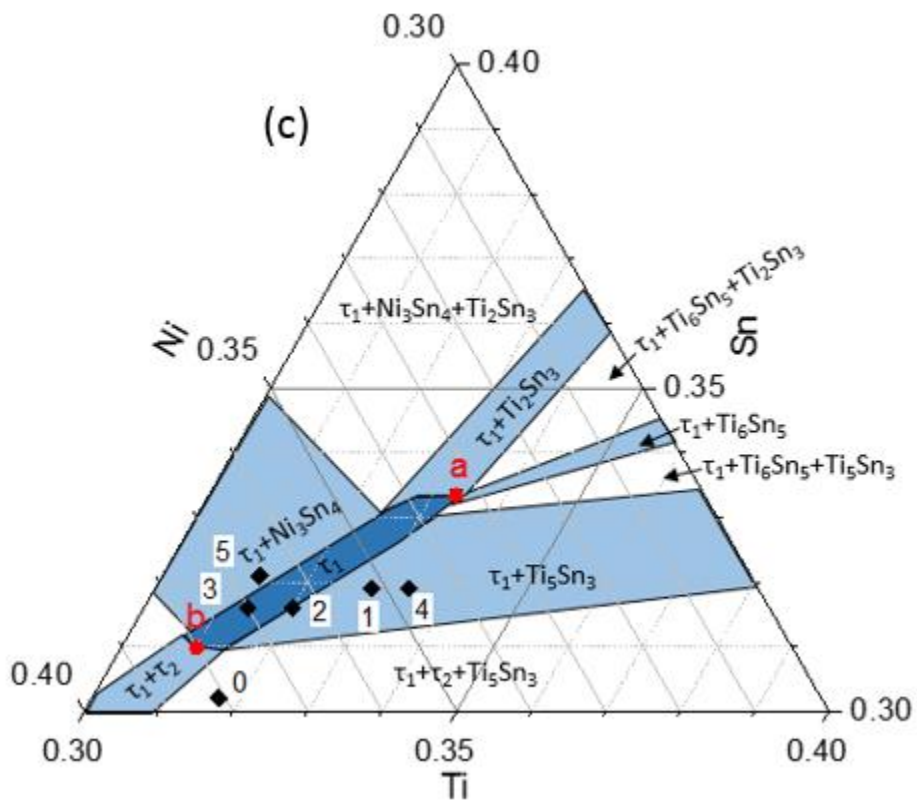
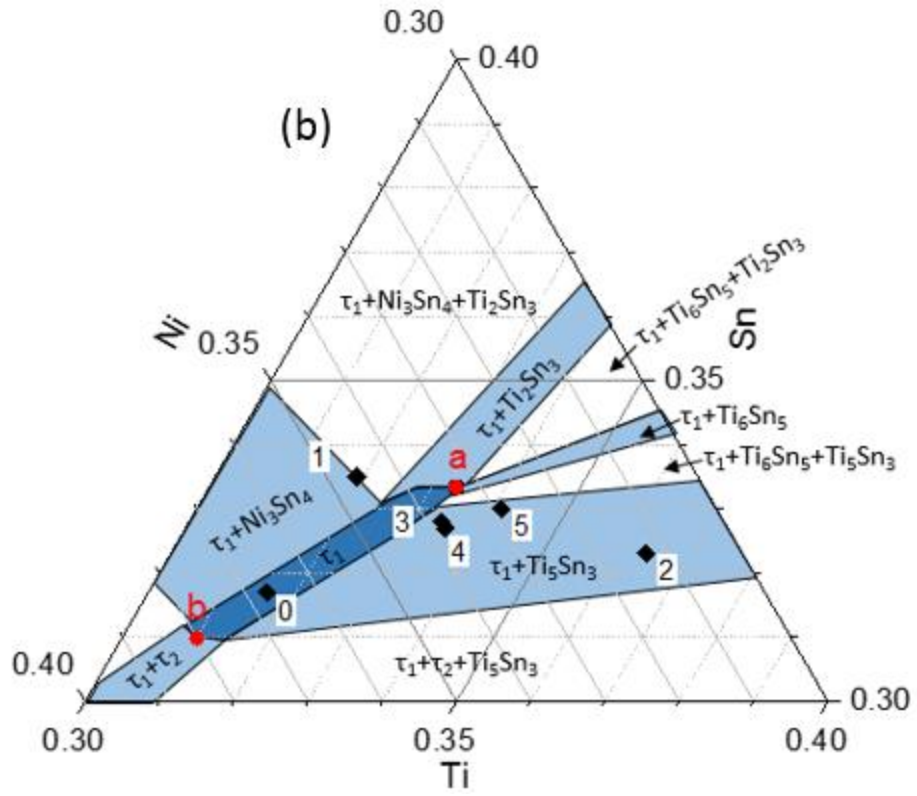


Figure 13: (a) Complete phase diagram with all 12 sample compositions; (b) Phase diagram section including samples where $x = 0$ and (c) phase diagram section including samples where $x = 0.15$. For (b) and (c), black diamonds are sample conditions 0-5 (Table 2), red circles 'a' and 'b' are target elemental compositions TiNiSn and $\text{TiNi}_{1.15}\text{Sn}$.

Based on the Ti-Ni-Sn ternary phase diagram by M. Gürth et al, each composition resides within or very near the homogeneity region for TiNiSn single phase. Points 'a' and 'b' in Figure 13, which lie on the extreme ends of Ni solid solubility within TiNiSn , mark where $x = 0$ and $x = 0.15$ for $\text{TiNi}_{1+x}\text{Sn}$ would be. The average compositional deviation for $x = 0$ from point 'a' was $0.45 \pm 0.052\%$ Ti, $-2.00 \pm 0.019\%$ Sn, and $1.55 \pm 0.053\%$ Ni, while $x = 0.15$ from point 'b' was $1.22 \pm 0.027\%$ Ti, $-0.62 \pm 0.022\%$ Sn, and $-0.52 \pm 0.034\%$ Ni. Deviations from the target composition is due to the high current from the arc melting process, which when exposed to powders, can cause vaporization and material scattering.

5.2 Effect of Annealing Time for TiNiSn Alloy

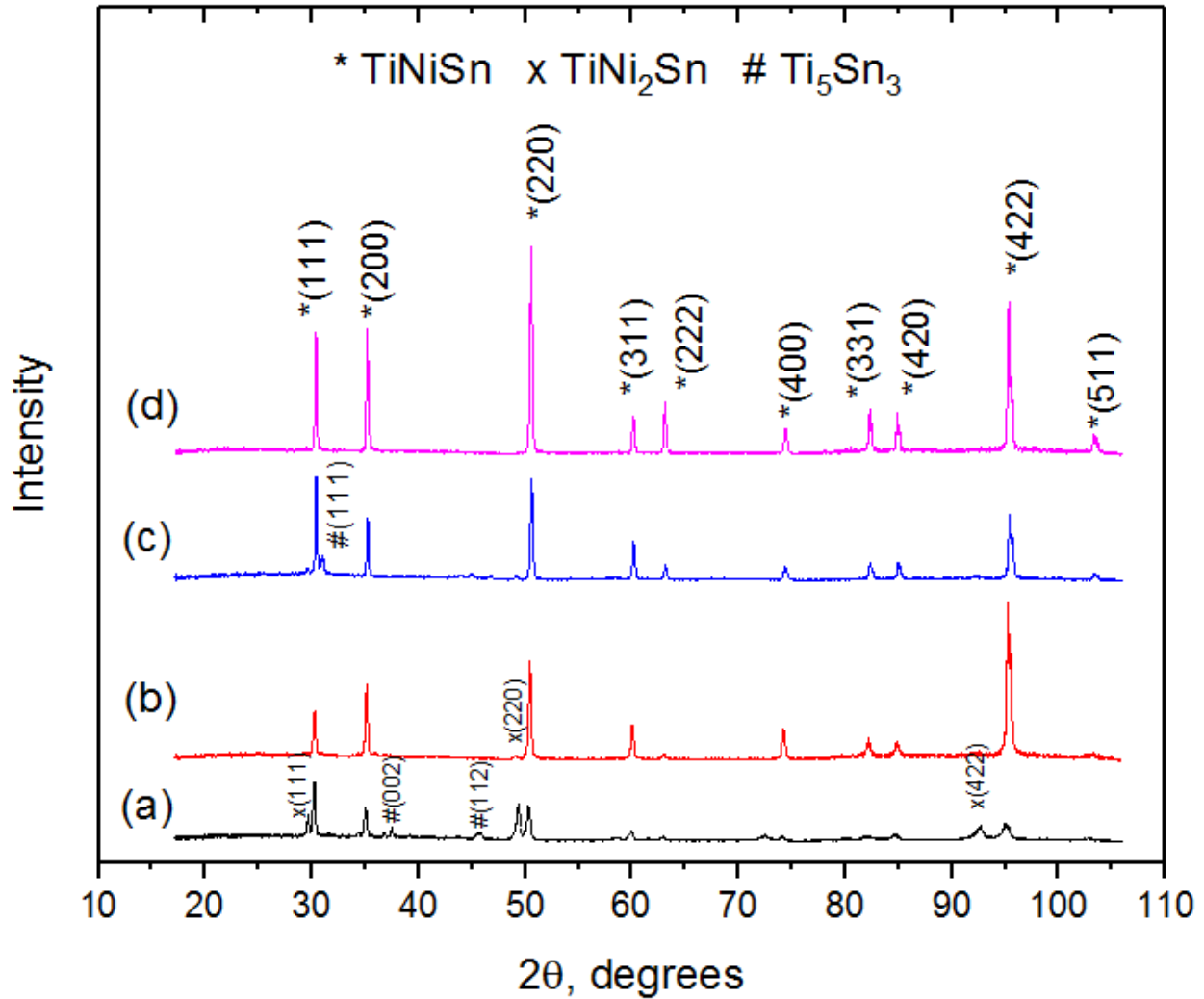


Figure 14: XRD (Co $K\alpha$) of TiNiSn alloy annealed at 800 °C for (a) 0 days; (b) 7 days; (c) 14 days; (d) 21 days.

Figure 14 above presents the phases present in the TiNiSn alloy samples based on their peak existence from X-ray diffraction with varying annealing durations at 800 °C. Without annealing, the arc-melted TiNiSn sample exhibited many small impurity XRD peaks which signify the existence of many undesired binary and ternary phases. This varies greatly from the theoretical prediction of pure TiNiSn based on the ternary phase diagram. The existence of phases other than TiNiSn can be explained by the non-homogeneity of the powders during the

arc-melting process, which creates localized zones that are not the overall elemental ratio, effectively creating different starting locations for cooling paths on the phase diagram. After one and two weeks of annealing, the alloy progresses towards phase equilibrium and most of the small impurity peaks are eliminated. TiNiSn is the primary phase, while TiNi₂Sn and Ti₅Sn₃ are seen as very small single peaks on the curve. After three weeks of annealing, only TiNiSn peaks were seen.

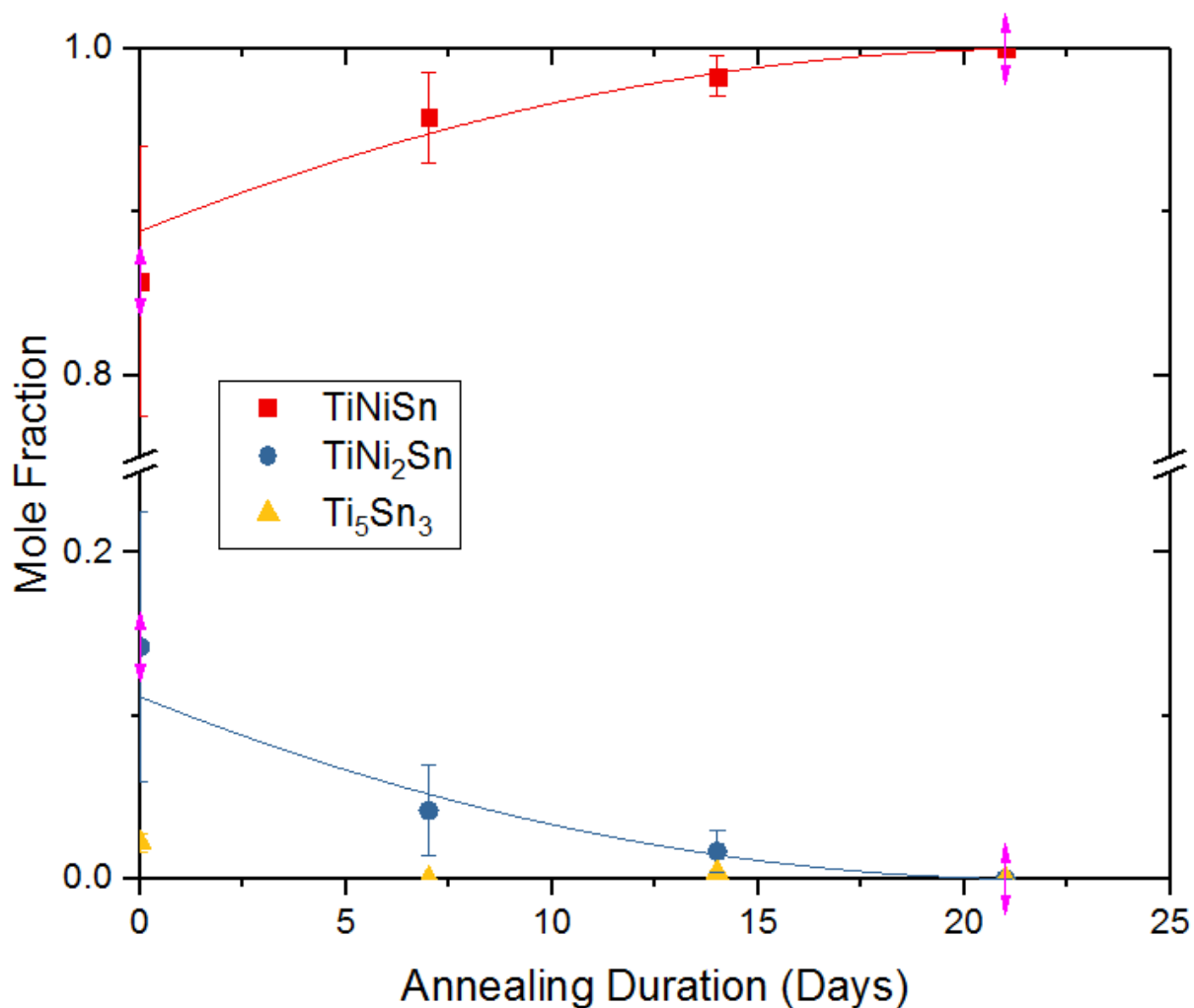


Figure 15: Mole fraction of phases present in TiNiSn alloy after annealing at 800 °C for different durations.

The mole fractions of the phases present in the TiNiSn alloy samples after annealing at 800°C, shown in Figure 15, were calculated using Rietveld analysis from five different XRD

sites from each sample. TiNiSn phase was initially present above 80 mol% and increased with annealing duration to approximately 100% after three weeks. TiNi₂Sn and binary phases, such as Ti₅Sn₃, were present at approximately 15% and 2%, and gradually were eliminated.

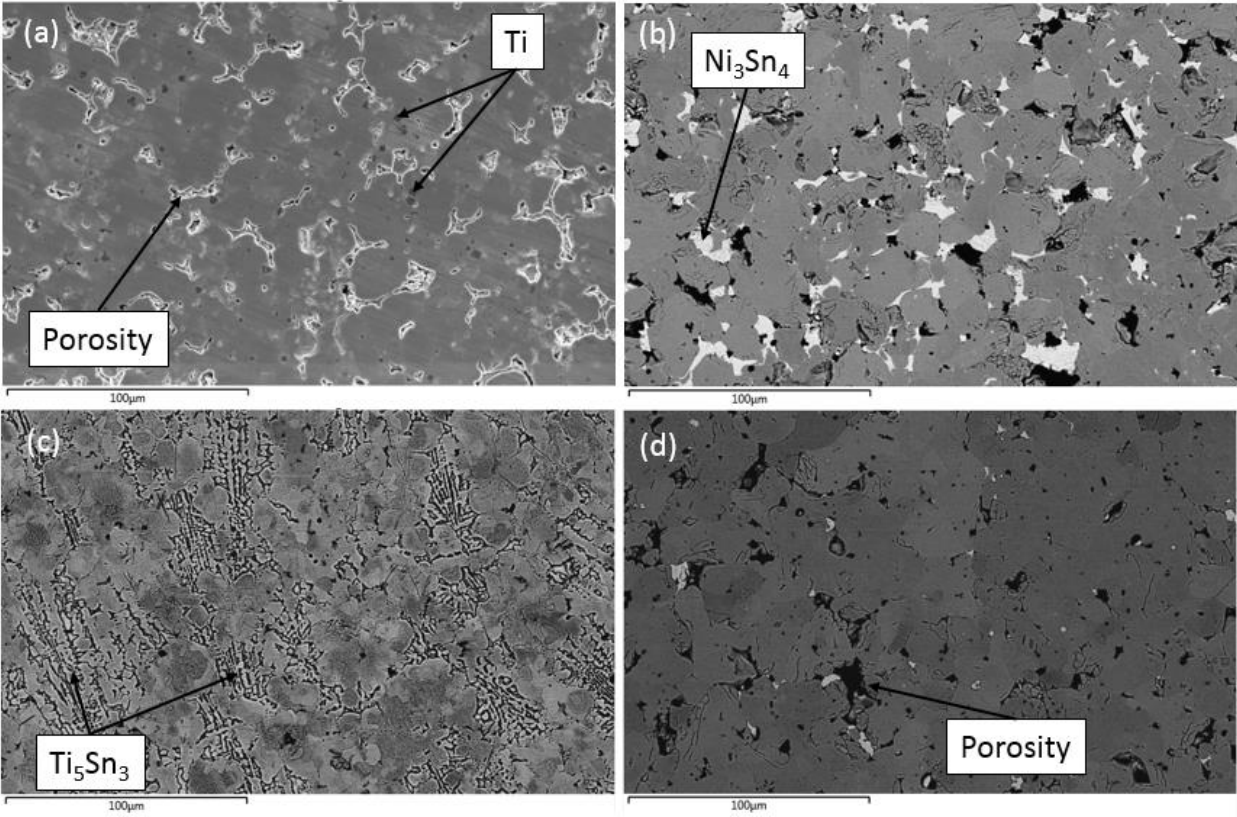


Figure 16: SEM/EBSD images of TiNiSn alloy samples annealed at 800 °C for (a) 0 days; (b) 7 days; (c) 14 days; (d) 21 days. Gray regions are a mixture of TiNiSn and TiNi₂Sn while impurity phases are highlighted.

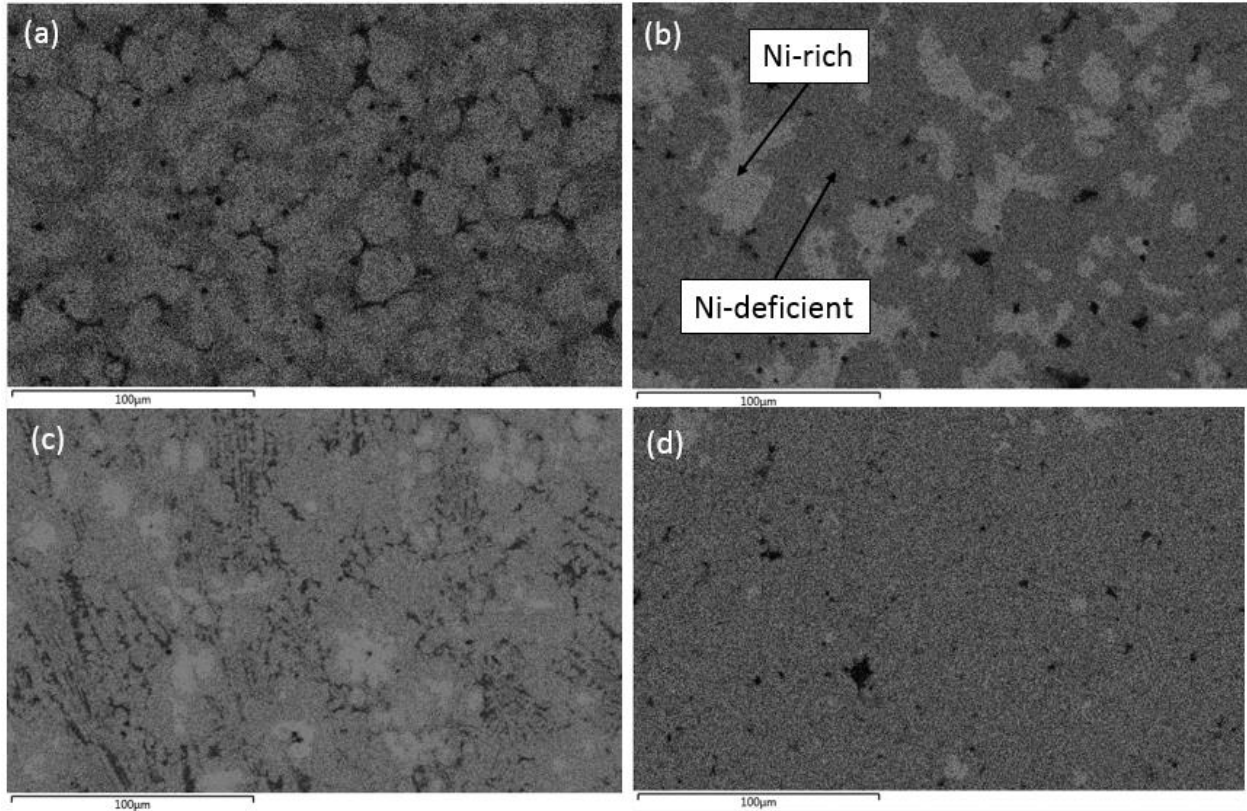


Figure 17: EDS of Ni $K\alpha$ of TiNiSn alloy samples annealed at 800 °C for (a) 0 days; (b) 7 days; (c) 14 days; (d) 21 days, corresponding to SEM images in Figure 18. Bright gray regions are Ni-rich ($TiNi_2Sn$), while darker-gray is TiNiSn and black is void of Ni.

SEM and EDS was completed, shown in Figures 16 and 17, in order to verify the phases present from XRD while also estimating the grain size of the alloy. EDS was necessary due to the similarity of the Heusler and half-Heusler crystal structures and their resultant brightness in SEM. From the SEM/EBSD pictures in Figure 16, the gray portions are TiNiSn and $TiNi_2Sn$, the white is Sn-rich, and the black spots are porosity. In order to differentiate between the TiNiSn and $TiNi_2Sn$, which have similar colored grains, EDS was completed to comparatively quantify the amount of Ni in each grain. In Figure 17, the brighter areas are more Ni-rich grains, concluding that it is $TiNi_2Sn$. Additionally, with increasing annealing duration, there is a decreasing amount of Ni-rich bright areas, corroborating with the XRD and mole fraction Rietveld analysis. The grain size can be interpreted from the $TiNi_2Sn$ areas, which is on the

order of tens of microns. This is about an order of magnitude larger than most literature examples.

5.3 Effect of Annealing Time for $\text{TiNi}_{1.15}\text{Sn}$ Alloy

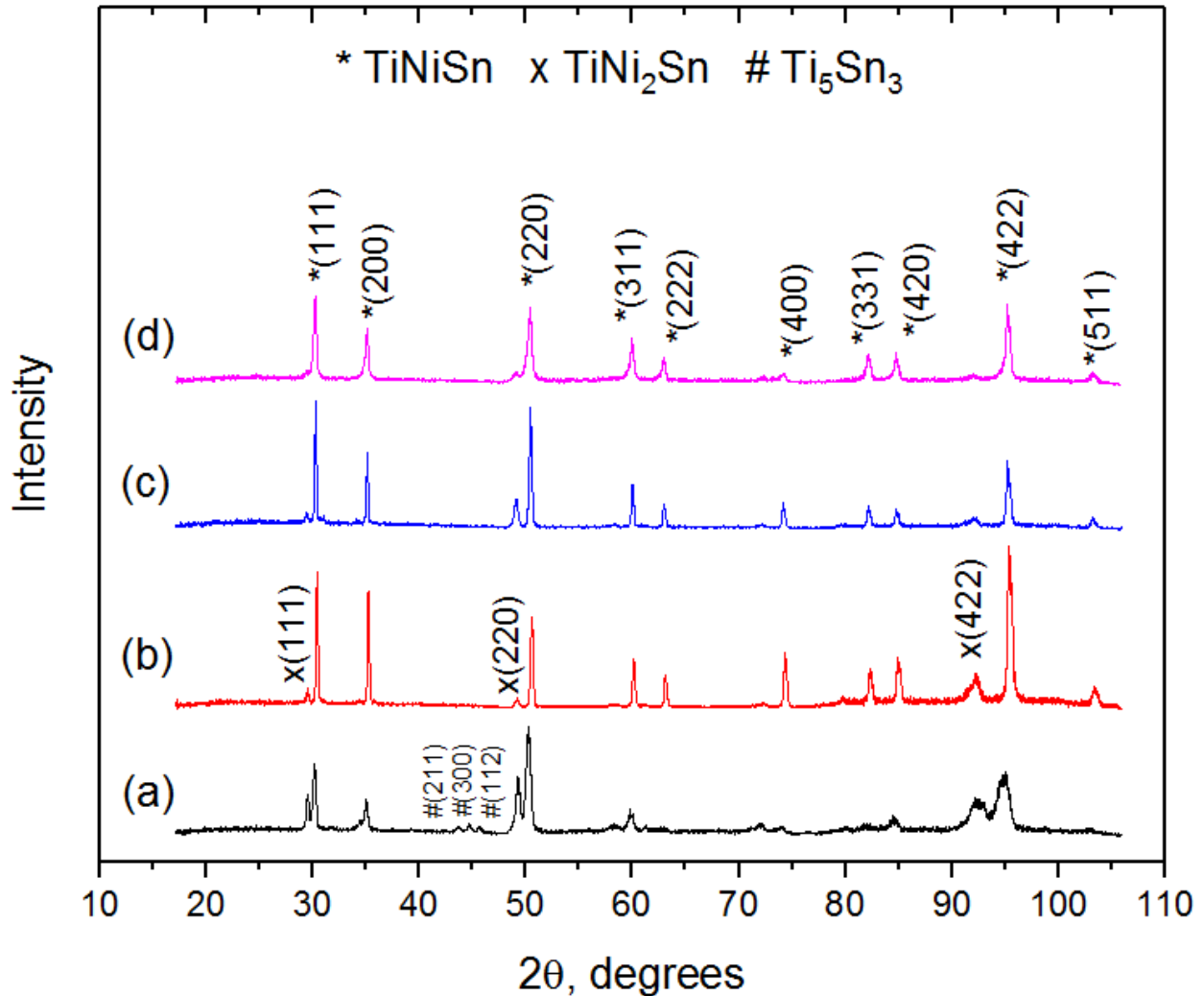


Figure 18: XRD ($\text{Co K}\alpha$) of $\text{TiNi}_{1.15}\text{Sn}$ alloy annealed at $800\text{ }^\circ\text{C}$ for (a) 0 days; (b) 7 days; (c) 14 days; (d) 21 days.

The phases present in the $\text{TiNi}_{1.15}\text{Sn}$ alloy after annealing for various durations at $800\text{ }^\circ\text{C}$ is shown in Figure 18. Similar to the TiNiSn alloy samples, the pre-annealed, arc-melted sample contained multiple impurity phases in addition to the expected two ternary phases, TiNiSn and TiNi_2Sn . After only one week of annealing, the impurity phase peaks were eliminated and only

TiNiSn and TiNi₂Sn are remaining, which corresponds well with the estimated final composition from the ternary phase diagram.

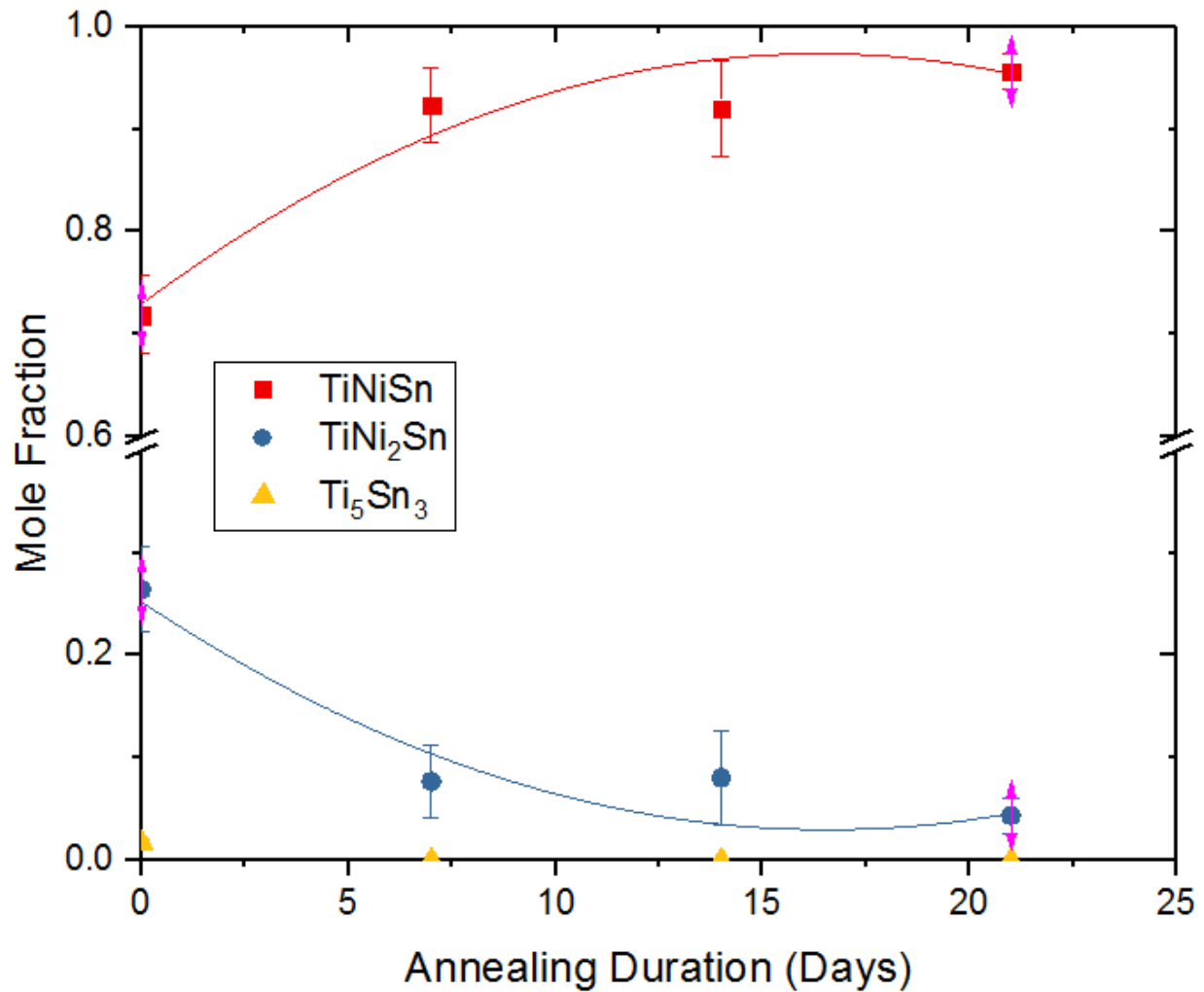


Figure 19: Mole fraction of phases present in TiNi_{1.15}Sn alloy after annealing at 800 °C for different durations.

The mole fraction of the phases present in the TiNi_{1.15}Sn alloy samples after annealing at 800°C, shown in Figure 19, was calculated using five different XRD sites from each sample, similar to the TiNiSn alloy. TiNiSn phase was initially present around 70 mol% and increased with annealing to approximately 90-95 mol% after 3 weeks. Impurity binary phases present in the unannealed sample were eliminated after 1 week of annealing. TiNi₂Sn, which is expected to be present in a significant amount, is initially about 25 mol% and decreases over three weeks of

annealing to approximately 5-10 mol%. The experimental amount of TiNi_2Sn is less than predicted (21 mol%) using the isopleth model in Figure 8, which could be due to a small loss of material during arc-melting.

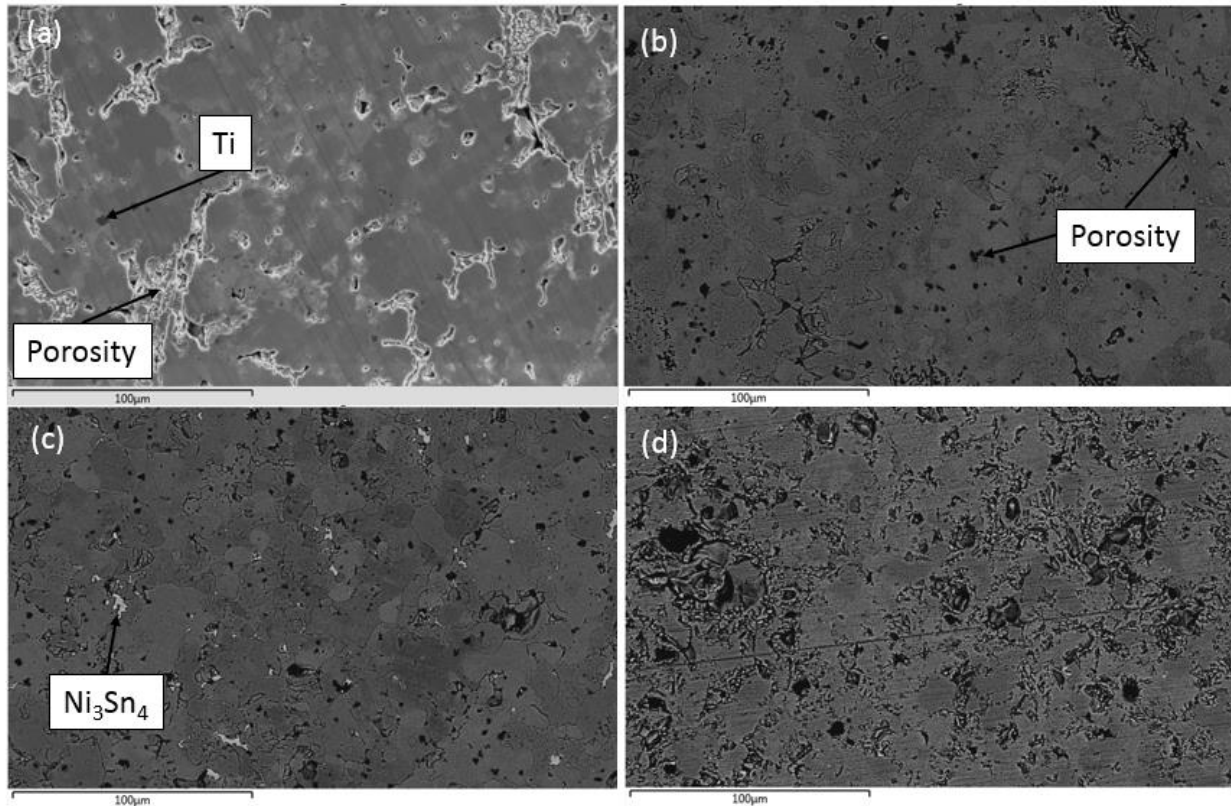


Figure 20: SEM/EBSD images of $\text{TiNi}_{1.15}\text{Sn}$ alloy samples annealed at $800\text{ }^\circ\text{C}$ for (a) 0 days; (b) 7 days; (c) 14 days; (d) 21 days. Gray regions are a mixture of TiNiSn and TiNi_2Sn while impurity phases are highlighted.

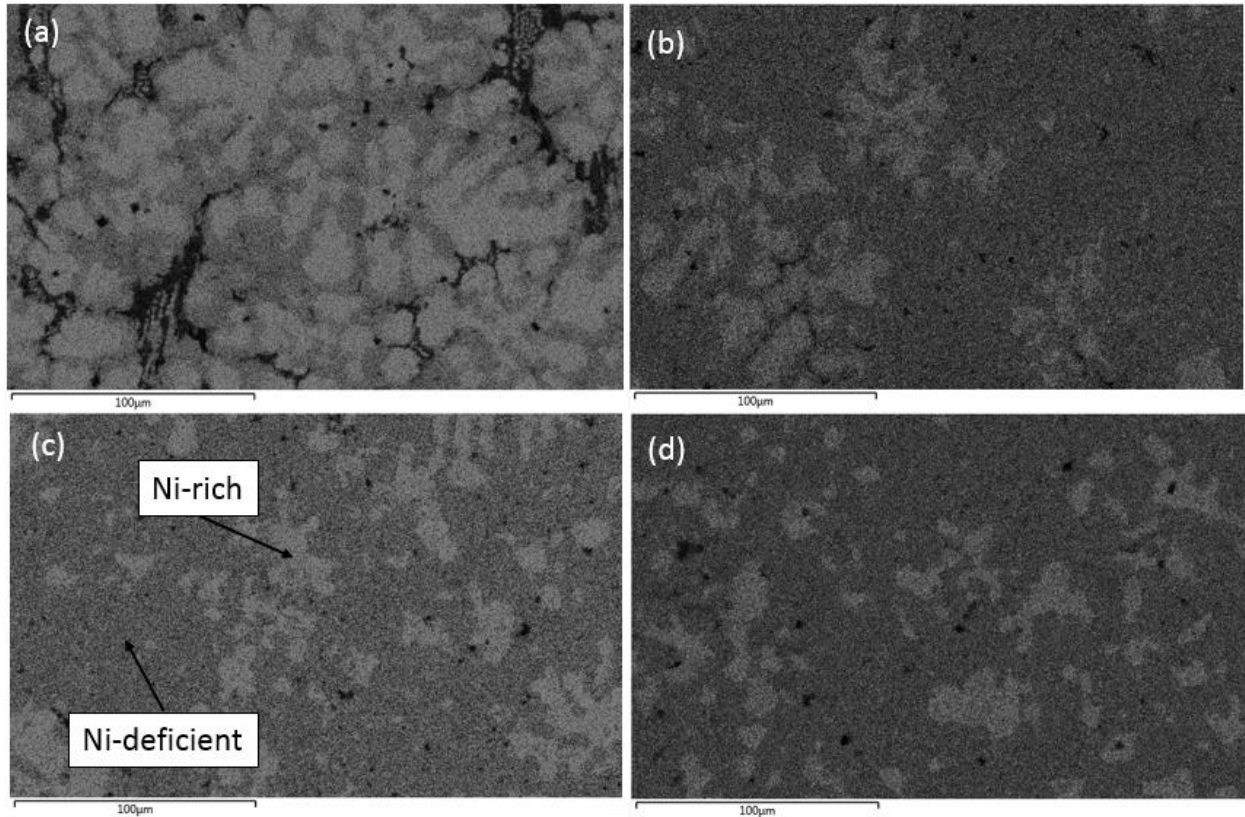


Figure 21: EDS of Ni K α of TiNi_{1.15}Sn alloy samples annealed at 800 °C for (a) 0 days; (b) 7 days; (c) 14 days; (d) 21 days, corresponding to SEM images in Figure 22. Bright gray regions are Ni-rich (TiNi₂Sn), while darker-gray is TiNiSn and black is void of Ni.

From SEM/EBSD and EDS analysis in Figures 20 and 21, the grain size, estimated from the TiNi₂Sn bright areas in EDS, is on the order of tens of microns with extremely irregular shapes. The quantity and density of Ni-rich areas is initially large, but quickly decreases to a moderately steady amount following one week of annealing, agreeing with the mole fraction trend in Figure 19.

5.4 Effect of Annealing Temperature for TiNiSn Alloy

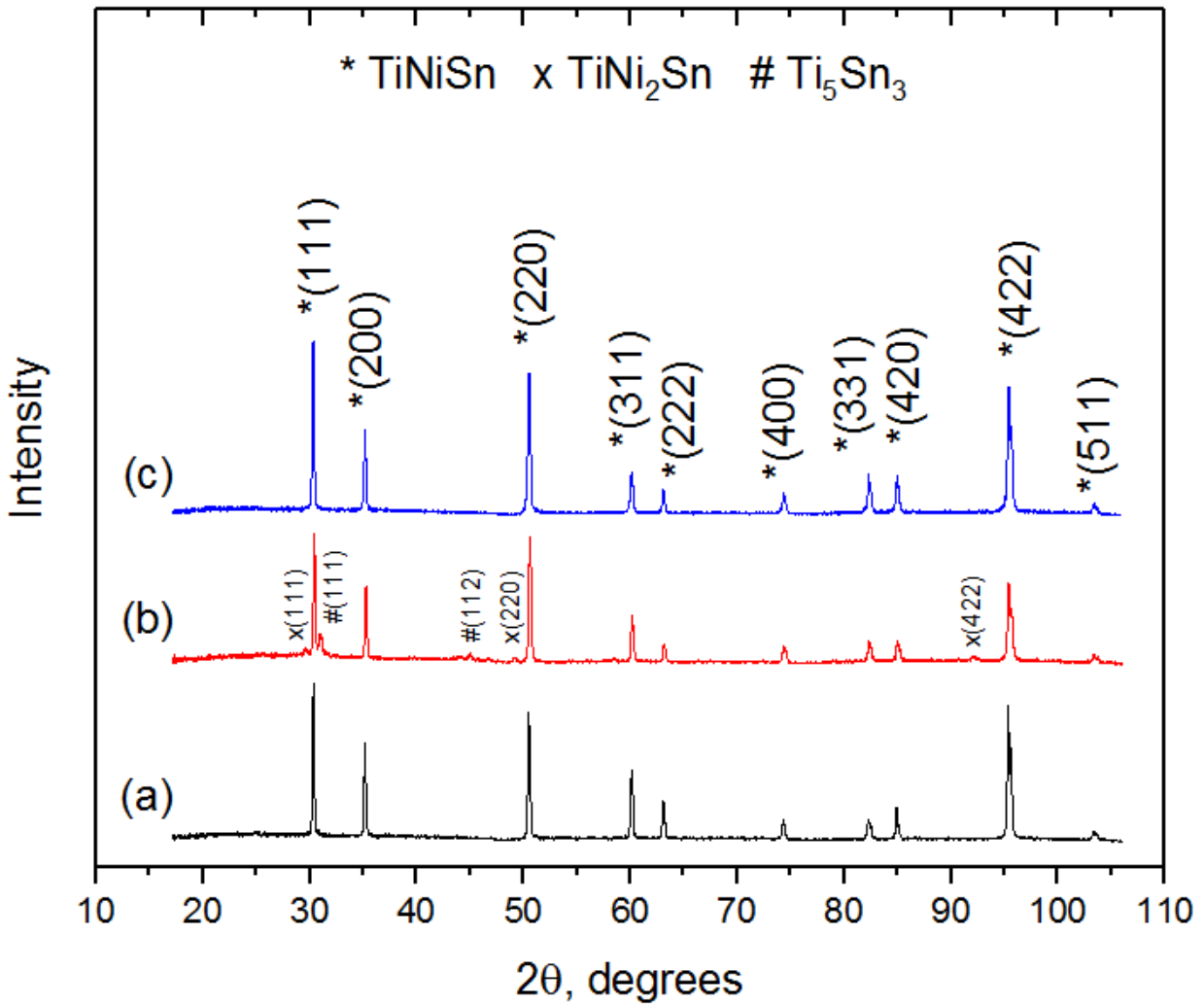


Figure 22: XRD (Co $K\alpha$) of TiNiSn alloy samples annealed for 14 days at (a) 700 °C; (b) 800 °C; (c) 900 °C.

The effect of annealing temperature on the phases present in the TiNiSn alloy is shown in Figure 22. Annealing temperature was varied from 700 – 900 °C for two weeks. From the XRD peaks, TiNiSn is the only major phase remaining after two weeks of heat treatment. Very small peaks for TiNi₂Sn and Ti₅Sn₃ were seen in the 800 °C sample, but can't be found in 700 and 900 °C graphs. These impurities may be due to experimental variance of phase changes during the isoplethal cooling.

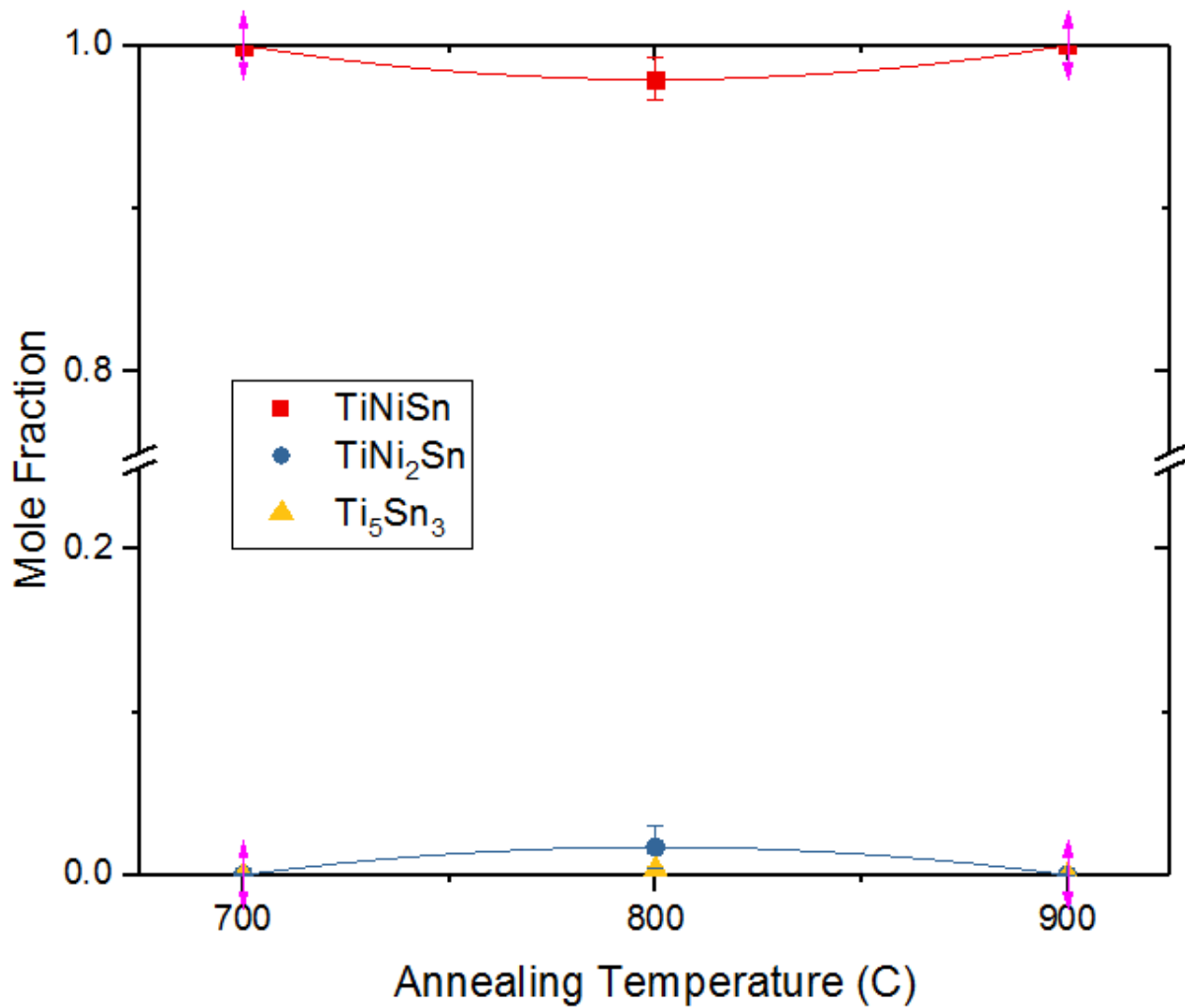


Figure 23: Mole fraction of phases present in TiNiSn alloy after annealing for 14 days at different temperatures.

Mole fraction of phases present was calculated from XRD for the TiNiSn alloy with changing temperature in Figure 23. Similar to the XRD in Figure 24, TiNiSn was the primary phase with almost 100% present at each annealing temperature with very small amounts of secondary phases. For only the 800 °C sample, a measureable amount of secondary phases were present, which can be associated with arc-melting variance. It can be reasonably concluded that change in annealing temperature for two weeks does not have a significant effect on the phase equilibria.

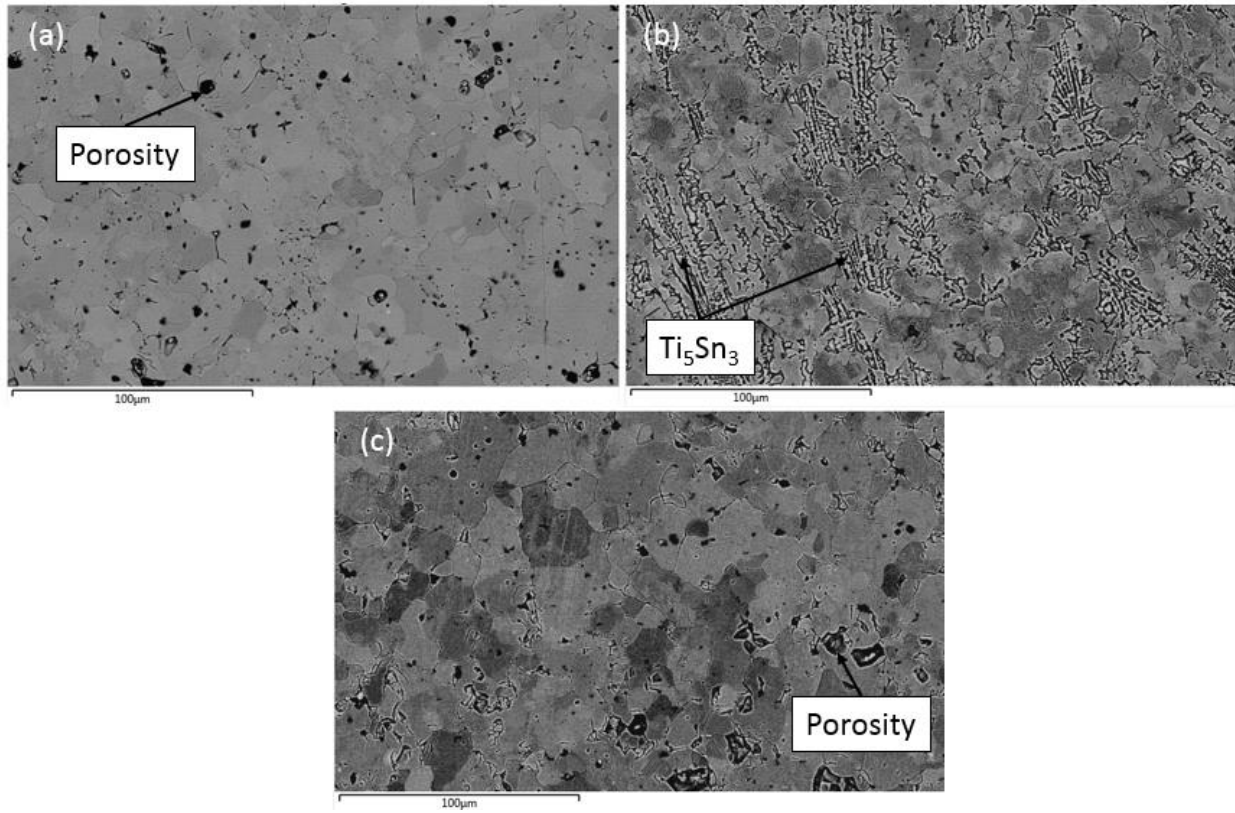


Figure 24: SEM/EBSD images of TiNiSn alloy samples annealed for 14 days at (a) 700 °C; (b) 800 °C; (c) 900 °C. Gray regions are a mixture of TiNiSn and TiNi₂Sn while impurity phases are highlighted.

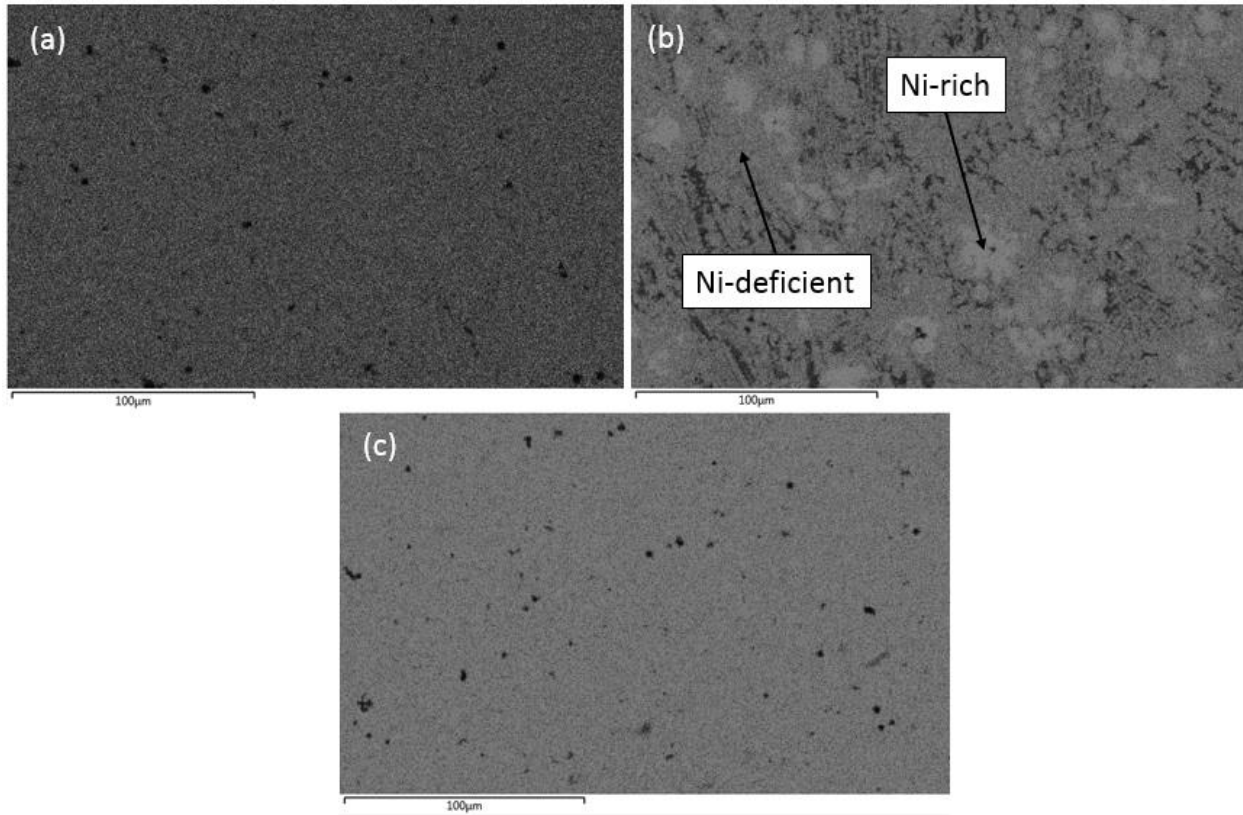


Figure 25: EDS of Ni $K\alpha$ of TiNiSn alloy samples annealed for 14 days at (a) 700 °C; (b) 800 °C; (c) 900 °C, corresponding to SEM images in Figure 26. Bright gray regions are Ni-rich ($TiNi_2Sn$), while darker-gray is TiNiSn and black is void of Ni.

Comparing images (a) and (c) from SEM/EBSD and EDS in Figures 24 and 25, little to no Sn- or Ni-rich areas are observed, proving the pure TiNiSn phase. Image (b) contains some bright spots as well as additional porosity, which can be assumed to be an outlier based on the behavior at the other annealing temperatures due to arc-melting differences. All three samples correspond well with the XRD and Rietveld analysis completed. From the EBSD images, the grain size is on the order of tens of microns.

5.5 Effect of Annealing Temperature for $\text{TiNi}_{1.15}\text{Sn}$ Alloy

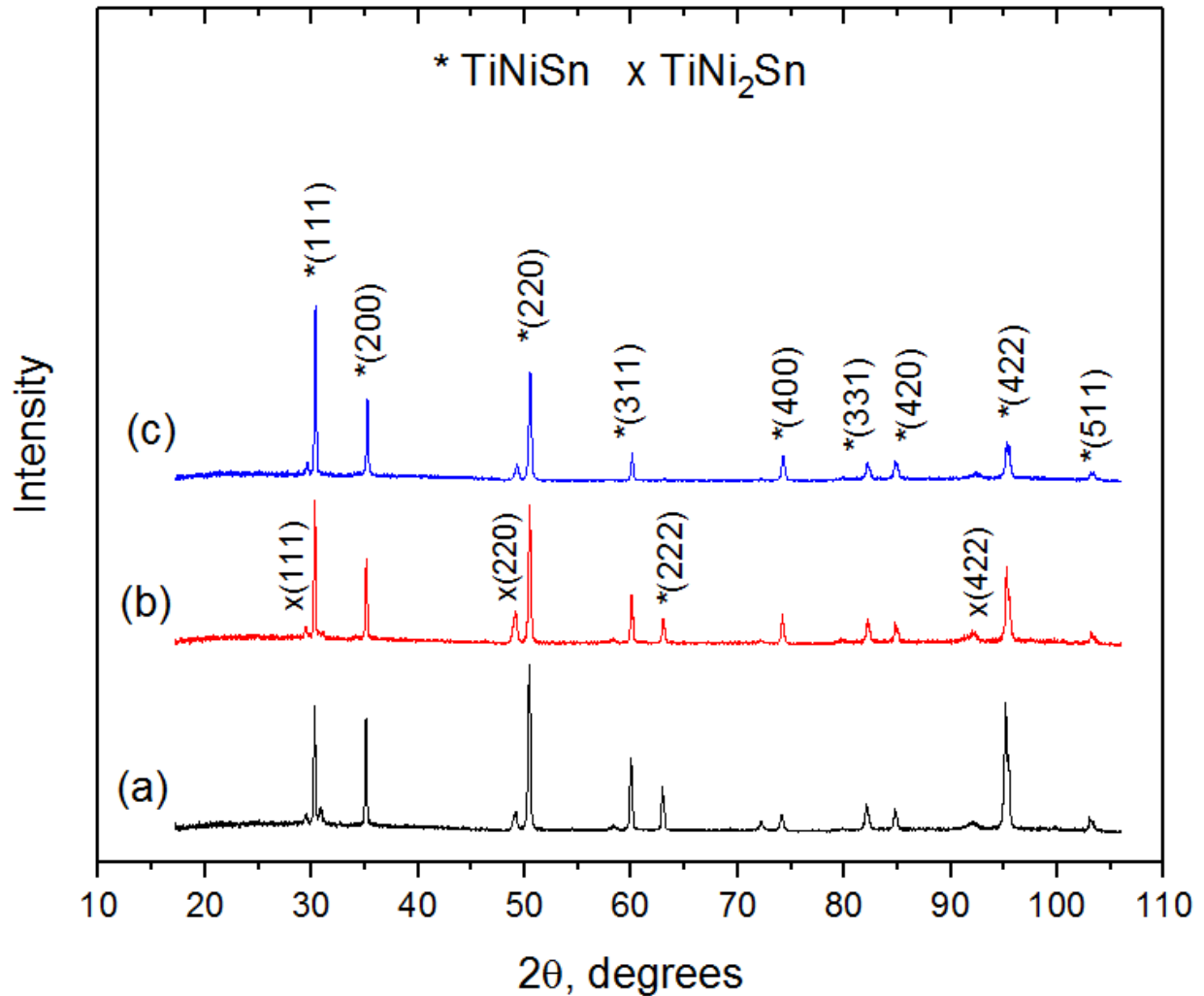


Figure 26: XRD (Co $K\alpha$) of $\text{TiNi}_{1.15}\text{Sn}$ alloy samples annealed for 14 days at (a) 700 °C; (b) 800 °C; (c) 900 °C.

For the $\text{TiNi}_{1.15}\text{Sn}$ alloy, the effect of annealing temperature (700 – 900 °C) on the phase equilibria is shown in Figure 26. At each temperature, both TiNiSn and TiNi_2Sn ternary phases are present with multiple peaks. No other ternary or binary phases are seen. Based on the XRD, it can be concluded that two weeks is sufficient duration regardless of temperature in order to produce the desired two phase alloy.

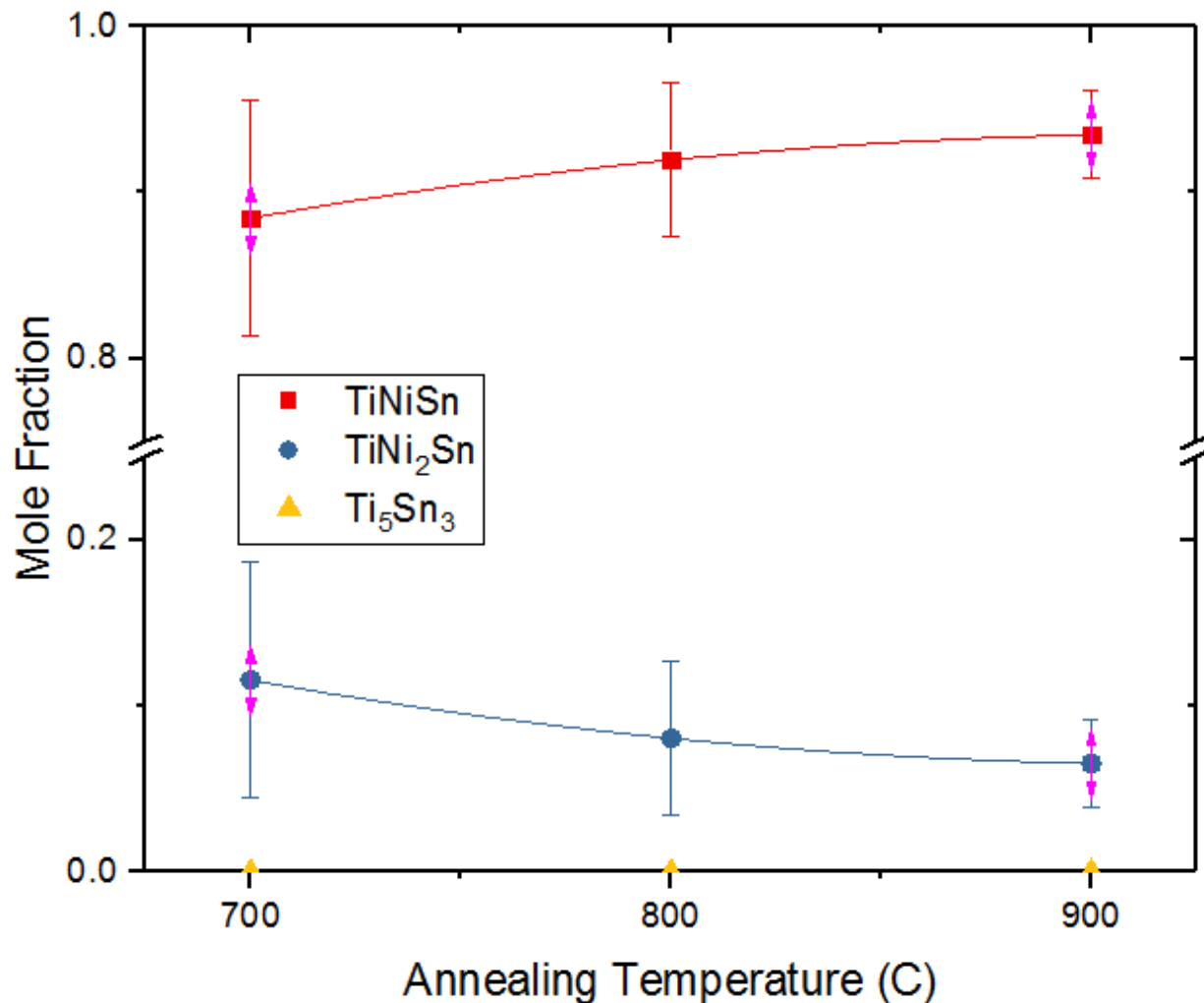


Figure 27: Mole fraction of phases present in TiNi_{1.15}Sn alloy after annealing for 14 days at different temperatures.

The mole fraction of phases in the TiNi_{1.15}Sn alloy was calculated using Rietveld analysis from XRD for each annealing temperature. For each annealing temperature, both TiNiSn and TiNi₂Sn phases were present. The mole fraction average values of TiNiSn slightly increase with increasing temperature while TiNi₂Sn decreases with the same change in temperature. Despite the average values, it cannot be said if temperature has an effect on mole fraction based on the overlapping standard deviations.

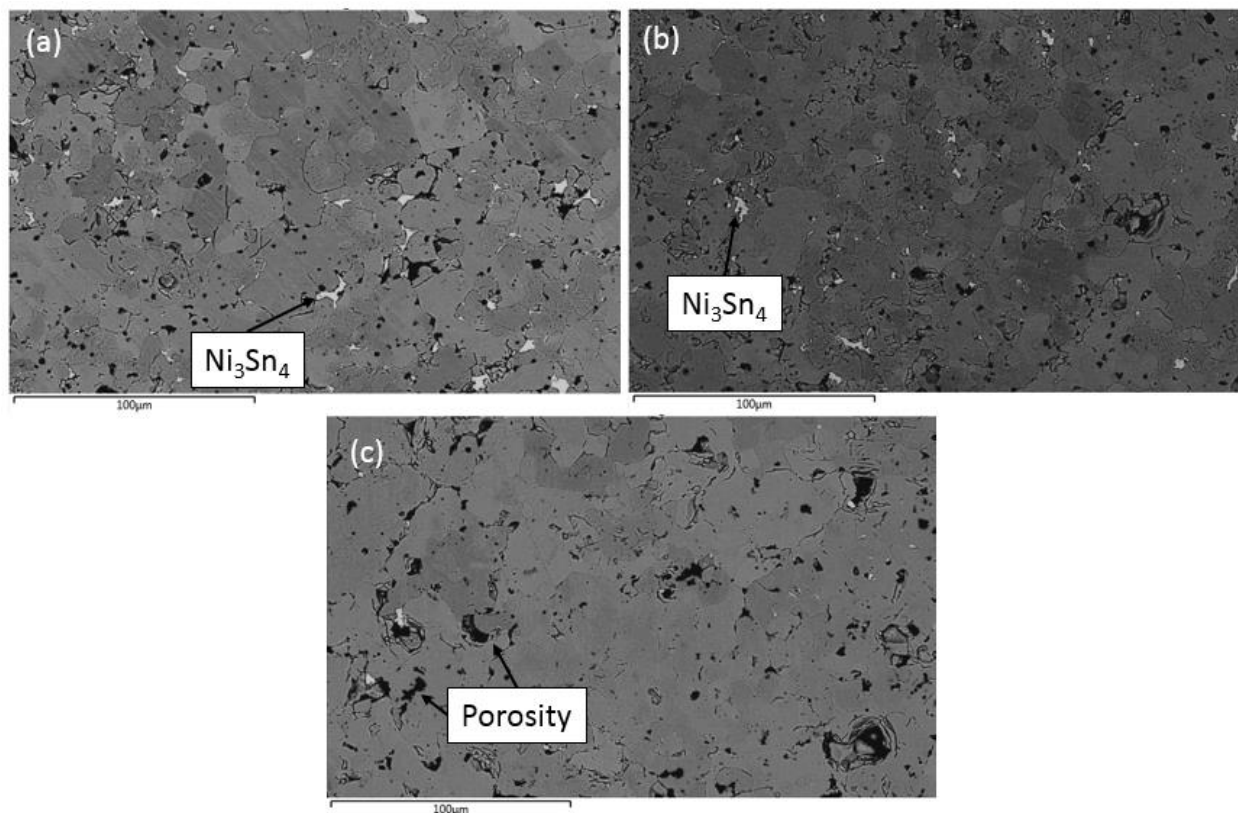


Figure 28: SEM/EBSD images of TiNi_{1.15}Sn alloy samples annealed for 14 days at (a) 700 °C; (b) 800 °C; (c) 900 °C. Gray regions are a mixture of TiNiSn and TiNi₂Sn while impurity phases are highlighted.

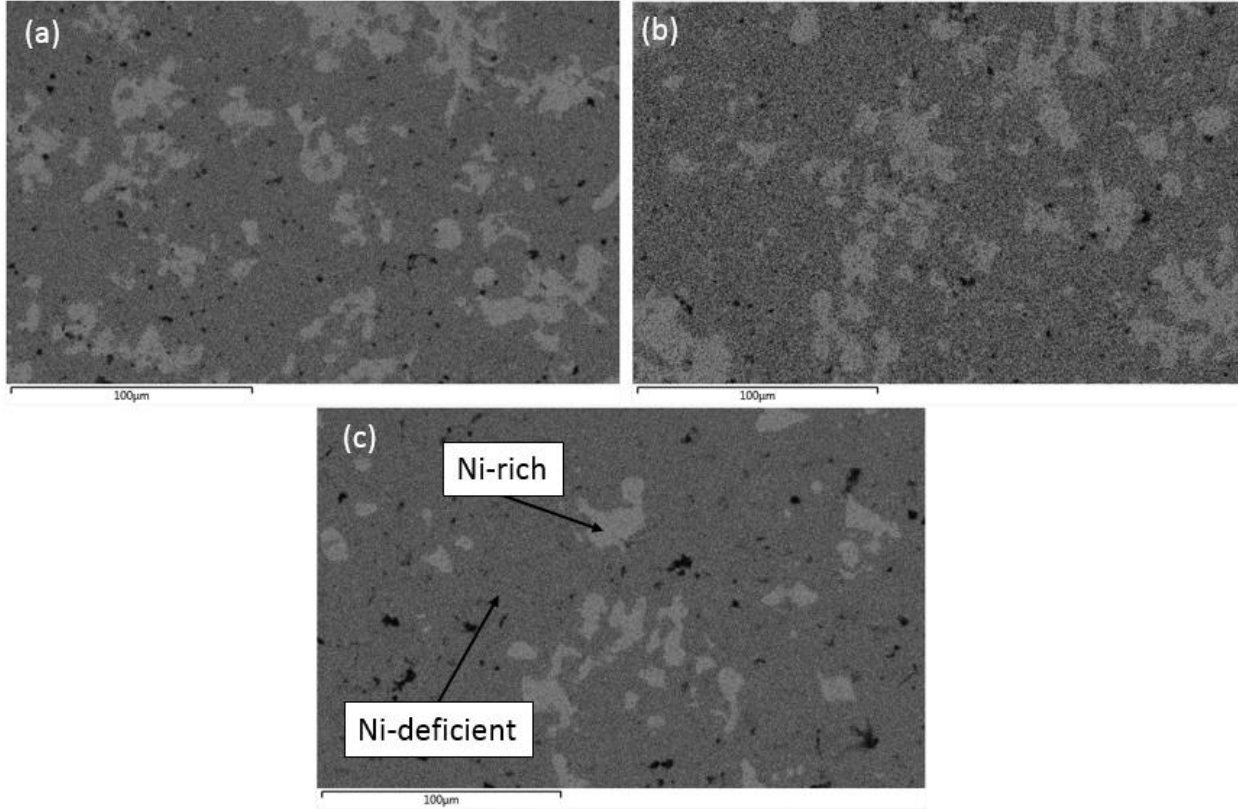


Figure 29: EDS of Ni $K\alpha$ of $TiNi_{1.15}Sn$ alloy samples annealed for 14 days at (a) 700 °C; (b) 800 °C; (c) 900 °C, corresponding to SEM images in Figure 30. Bright gray regions are Ni-rich ($TiNi_2Sn$), while darker-gray is $TiNiSn$ and black is void of Ni.

Comparing the three samples with SEM/EBSD and EDS in Figures 28 and 29, there is a small change in grain shape, size, or phase distribution with change in annealing temperature. The grain size for all three samples, estimated from the $TiNi_2Sn$ bright areas in EDS, is on the order of tens of microns with extremely irregular shapes. One minor variance with increasing temperature is the decreasing amount of Sn-rich (white) spots from SEM. This can either be attributed to increased energy for Sn diffusion or small variances from the arc-melting process.

5.6 Lattice Parameter Calculation for $TiNiSn$ and $TiNi_2Sn$ Phases

Based on the primary 100% peaks from XRD, d-spacing, and lattice parameter can be calculated where:

$$2d \sin \theta = n\lambda$$

And

$$d_{hkl} = \frac{a}{\sqrt{h^2 + k^2 + l^2}}$$

Where d is the interplanar distance, n is a positive integer (assumed $n=1$), λ is the wavelength of incident wave (Co), θ is the Bragg angle, and a is the lattice parameter, which is the physical length of the cubic unit cell. Using the (220) primary planes for both TiNiSn and TiNi₂Sn phases, the observed Bragg angle was measured, shown in Figure 30 and 31.

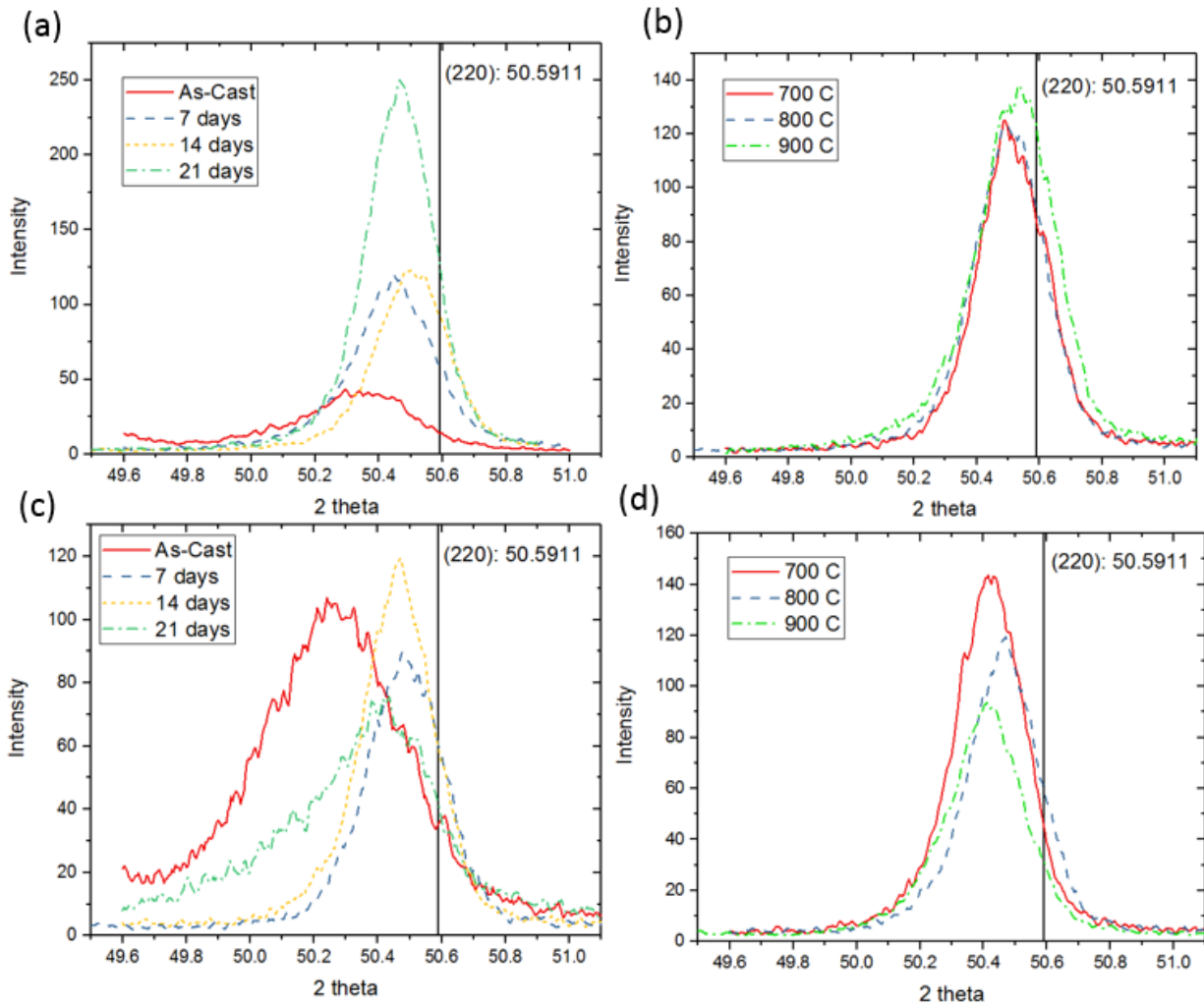


Figure 30: Theta differences for XRD of (220) plane for TiNiSn phase in (a) TiNiSn alloy with annealing duration; (b) TiNiSn alloy with annealing temperature; (c) TiNi_{1.15}Sn alloy with annealing duration; (d) TiNi_{1.15}Sn alloy with annealing temperature.

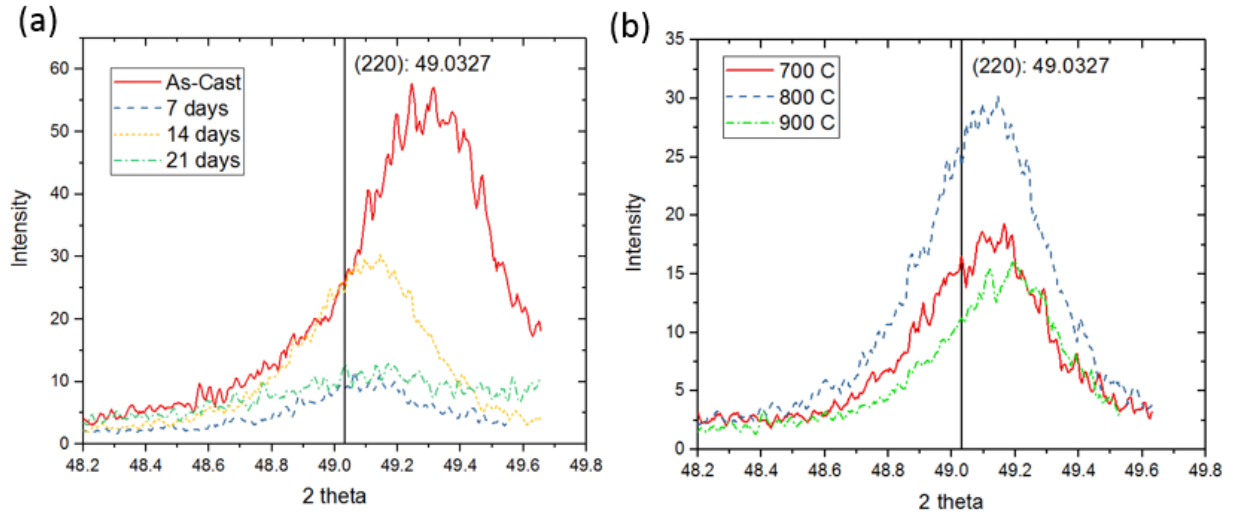


Figure 31: Theta differences for XRD of (220) plane for TiNi_2Sn phase in $\text{TiNi}_{1.15}\text{Sn}$ alloy (a) with annealing duration; (b) with annealing temperature.

The experimental values for Bragg angles compare well with only slight deviations from literature standards [43, 44]. Shifts in peaks are generally due to defects within the unit cells which cause a volume change. Lattice constant was calculated for TiNiSn and TiNi_2Sn ternary phases as a function of annealing duration and temperature in Figure 32 and 33.

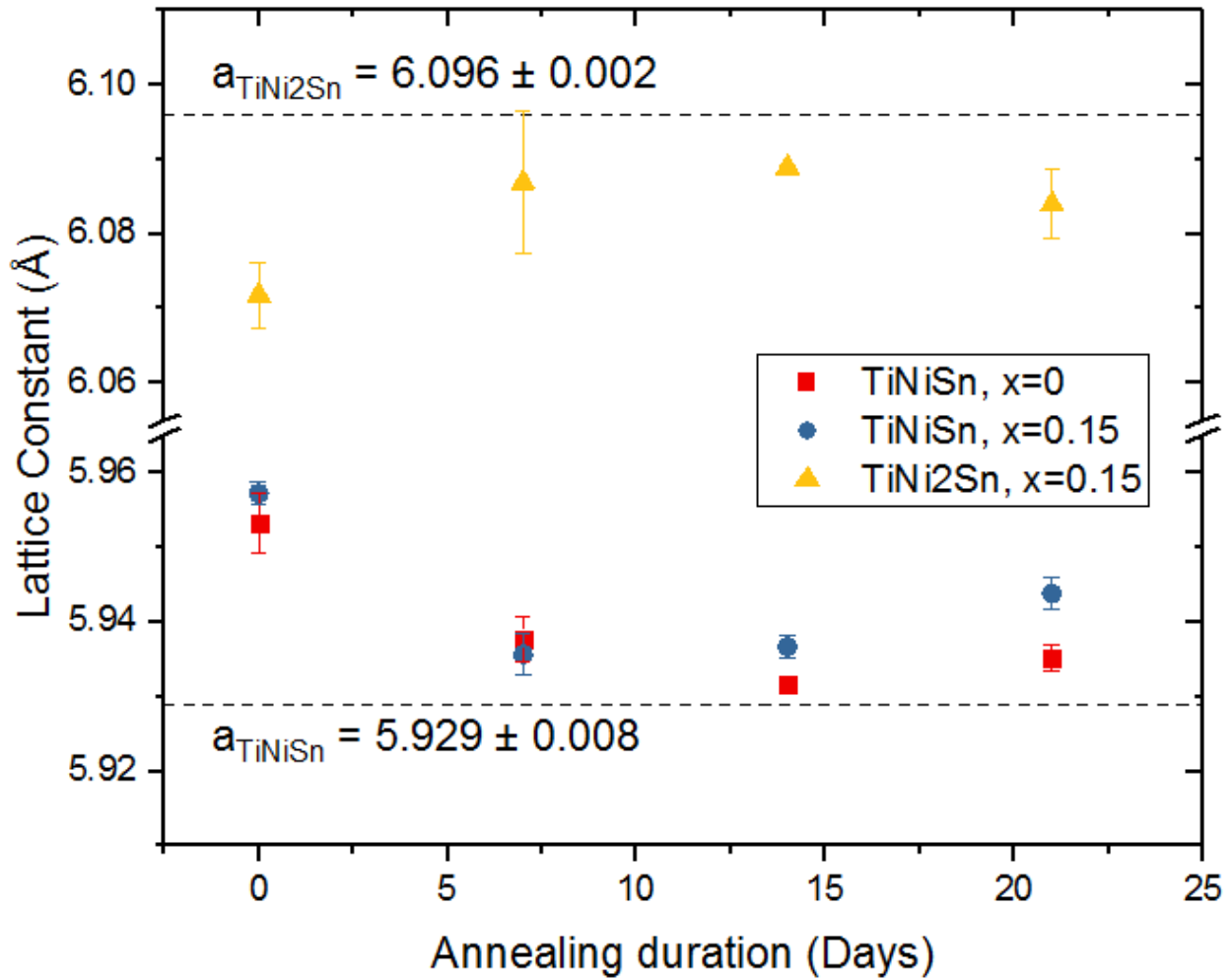


Figure 32: Changes in lattice constant with increasing annealing duration at 800 °C calculated from XRD.

The ternary phases present in the as-cast samples with no heat treatment (0 days annealing duration) show a considerable amount of disparity when compared to the ICDD standard lattice constant (dotted lines). With increasing annealing time, up to 21 days, the lattice constant for TiNiSn decreases and TiNi₂Sn increases as phase equilibrium is approached, but neither reach their theoretical value. Additionally, nickel doping increased the lattice constant of the TiNiSn phase comparatively.

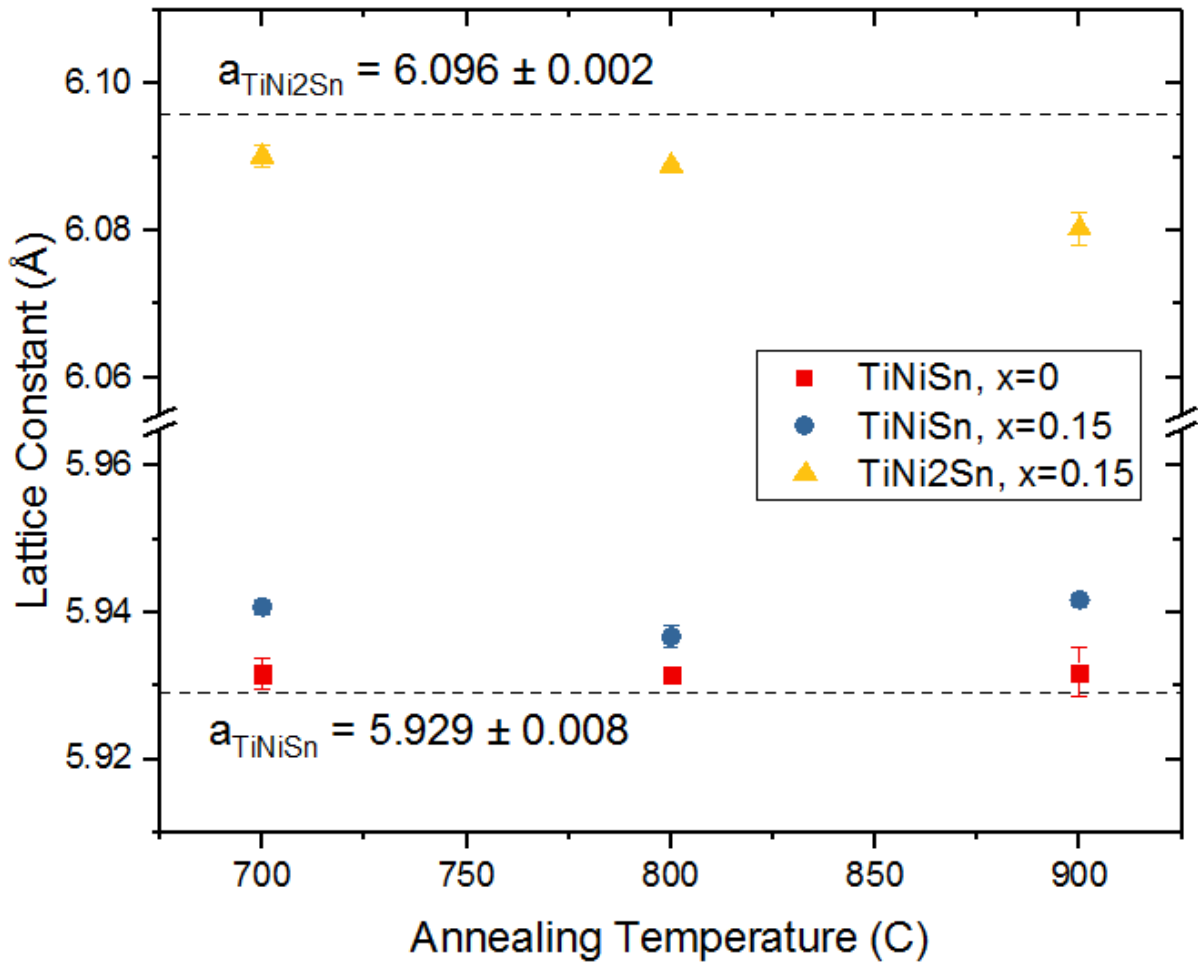


Figure 33: Changes in lattice constant with annealing temperature for two weeks calculated from XRD.

Similarly to Figure 32, differences in lattice constant from the standard value are seen for both ternary phases at all annealing temperatures. The lattice constant did not seem to change dramatically with a change in temperature. It can therefore be assumed that annealing time is a more critical parameter than temperature with regards to defect equilibrium and lattice constant.

5.7 Ni-defects in $TiNi_{1+x}Sn$ Compounds

Gürth et al completed a DFT analysis of $TiNi_{1+x}Sn$ compounds by increasingly filling the four stable voids with Ni atoms. They reported the enthalpy of formation at $T = 0$ K for $TiNiSn$ as -52.786 kJ/mol, while $TiNi_2Sn$ as -45.626 kJ/mol, meaning that $TiNiSn$ is most stable within

this central region of the phase diagram (assuming negligible entropic contribution). The stability of TiNiSn will have isoplethal solidification paths tend toward this phase [28].

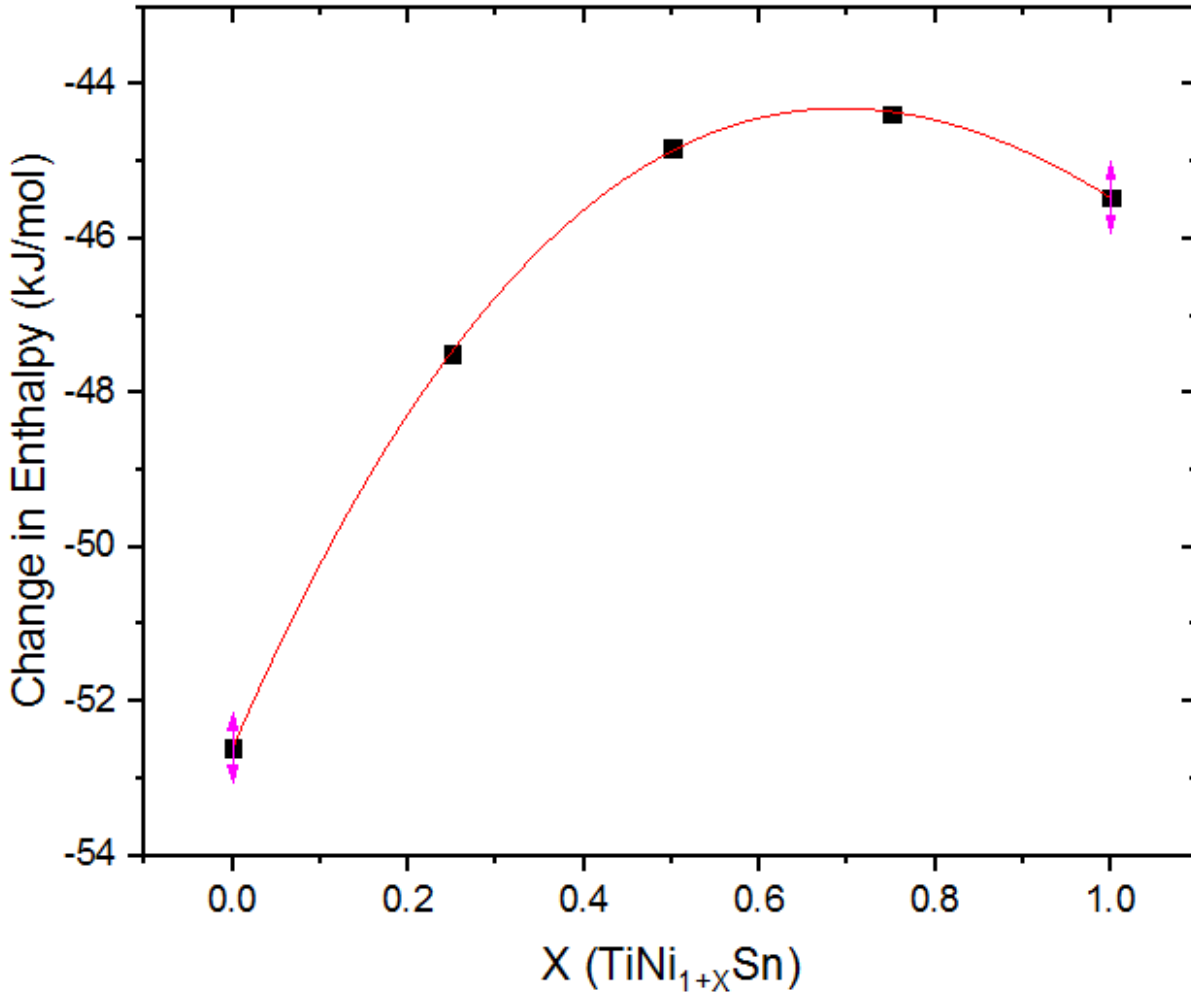


Figure 34: DFT values of the enthalpy of formation (ΔH_f) at $T = 0$ K for $\text{TiNi}_{1+x}\text{Sn}$ compounds [28].

TiNiSn continues to have the most negative enthalpy of formation with increasing Ni content up to approximately $X = 0.4$, where TiNi_2Sn (with Ni vacancies) becomes more stable. Realistically, each phase has a single phase homogeneity region with respect to Ni content and temperature where each phase exists separately and as a binary alloy between both homogeneity

regions. For example, at 1100 °C, TiNiSn exists as a single phase when $0 < X < 0.221$ while TiNi₂Sn is the sole phase when $0.656 < X < 1$ [28].

Hazama et al found that interstitial Ni defects are easily introduced into the natural vacancy sites within the TiNiSn unit cell and are only partially eliminated with heat treatment, which reduce the activation (band) gap for conduction [45]. An increase in lattice constant of TiNiSn implies that the unit cell has expanded and contains Ni defects. This agrees with the increase of lattice constant seen with added nickel content, which essentially provides additional nickel to fill available vacancies in the TiNiSn phase. Inversely, it was found that TiNi₂Sn contains a smaller lattice constant for all heat treatment durations. Additionally, a change to the TiNiSn lattice constant magnitude produces an inverse change to TiNi₂Sn.

A likely defect scenario is based on the homogeneity regions of TiNiSn and TiNi₂Sn stretching toward one another which allows for small stable variances in Ni content on the tetrahedral sites. Immediately after melting, TiNi_{1+x}Sn samples will contain randomly distributed interstitial Ni defects at the vacancy sites. Based on DFE calculations by Hazama et

al [46], the lowest defect formation energy and change in lattice parameter was modeled, shown in Figure 35.

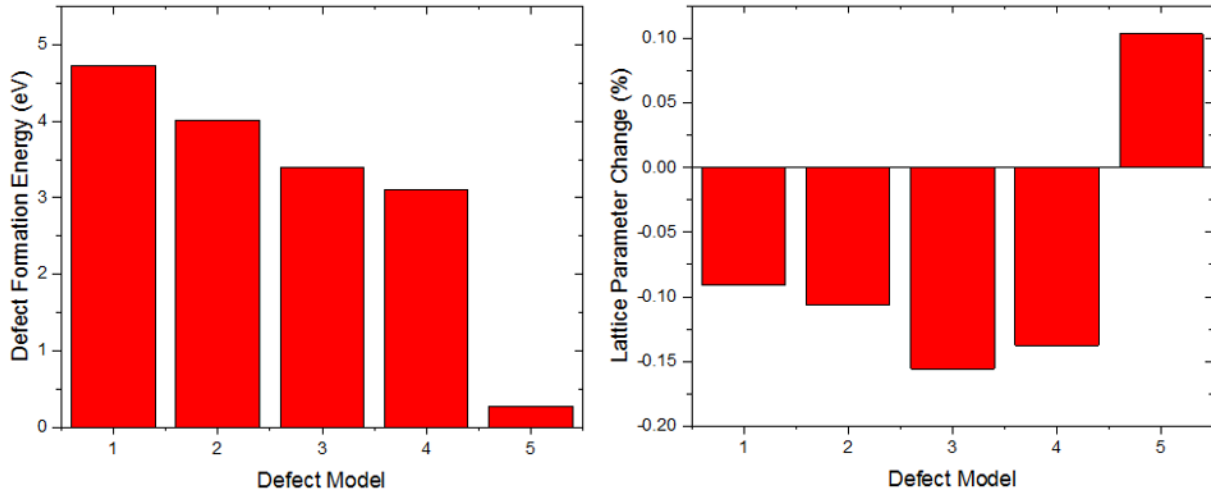


Figure 35: Defect formation energy and lattice parameter change of a TiNiSn perfect crystal for defect models: (1) Point defect at Sn-site, (2) Point defect at Ti-site, (3) Substitution of Ni for Ti atom, (4) Substitution of Ni for Sn atom, (5) Interstitial Ni atom in natural vacancy [46].

The lowest calculated defect formation energy compared to a TiNiSn perfect crystal was model 5, a Ni atom filling a vacancy within the half-Heusler unit cell. Model 5 was also the only defect model that produced an increase in lattice parameter of about 0.10%. From Figures 32 and 33, the change in lattice parameter for TiNiSn after annealing was +0.04% to 0.47%, while TiNi₂Sn changed by -0.09 to -0.40% based on annealing duration and temperature, correlating with Hazama's calculation.

With an annealing treatment (added thermal energy), Ni atoms diffuse due to an energetic drive to clump together to reduce lattice parameter and Gibbs energy of the system. Douglas et al [47] calculated the change in interstitial defect energy based on a theoretical TiNi_{1+x}Sn supercell, shown in Figure 36.

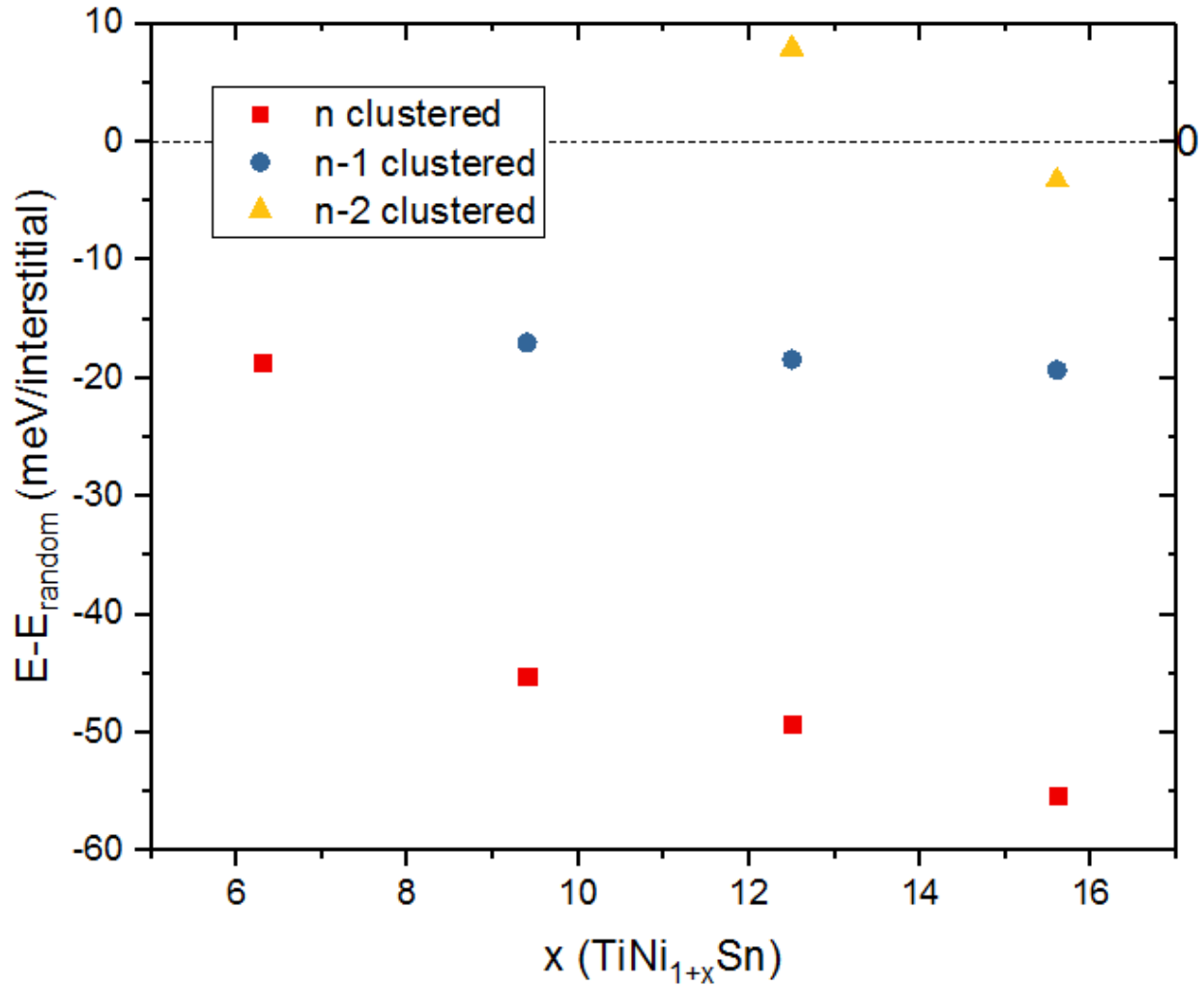


Figure 36: Difference in energy of Ni interstitial defect configuration from random distribution in $2 \times 2 \times 2$, $96+n$ atom, $\text{TiNi}_{1+x}\text{Sn}$ supercell where $n = 4$ [47].

Clustering of interstitial Ni atoms into a complete TiNi_2Sn was found to be lower in energy compared to a random distribution of Ni defects. The lowest energy state for the supercell at $n = 4$ was a single full-Heusler unit cell was surrounded by a half-Heusler lattice structure, but even with only 3 interstitial defects, clustering is still energetically favored [47].

Despite the drive to cluster together Ni defects to form TiNiSn and TiNi_2Sn , the lattice parameters calculated in this study never reached their standard values, even after three weeks of annealing. Kirievsky et al investigated the free energy of formation of TiNiSn and TiNi_2Sn at

T = 1027 °C based on Ni configuration within the unit cell and thermodynamic calculations, shown in Figure 37.

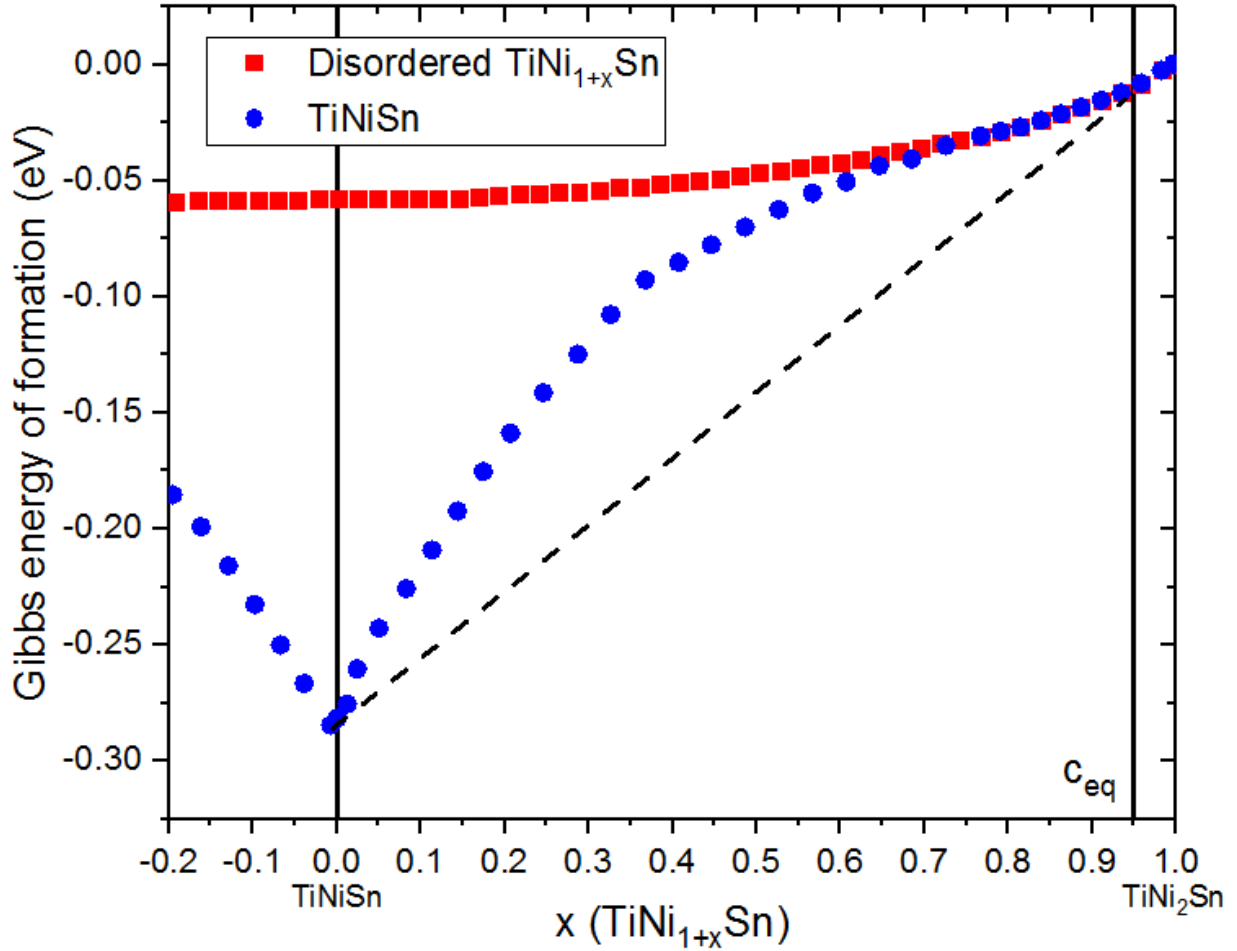


Figure 37: Free energy of formation of ordered TiNiSn and disordered Ti(Vacancy)_{1-x}Ni_{1+x}Sn solid solution at T = 1027 °C. The dotted line is the tangent line for composition equilibrium, c_{eq} [48].

At T = 1027 °C, a common tangent line can be drawn from the Gibbs energies of formation for perfect crystal TiNiSn and disordered Ti(Vacancy)_{1-x}Ni_{1+x}Sn in order to represent the equilibrium two-phase region. At approximately $x = 0.95$, the tangent line crosses both the ordered and disordered compositions, implying that an off-stoichiometric TiNi_{1.95}Sn phase can

be stable. The tangent line can be drawn at multiple temperatures to construct a binary phase diagram, shown in Figure 38.

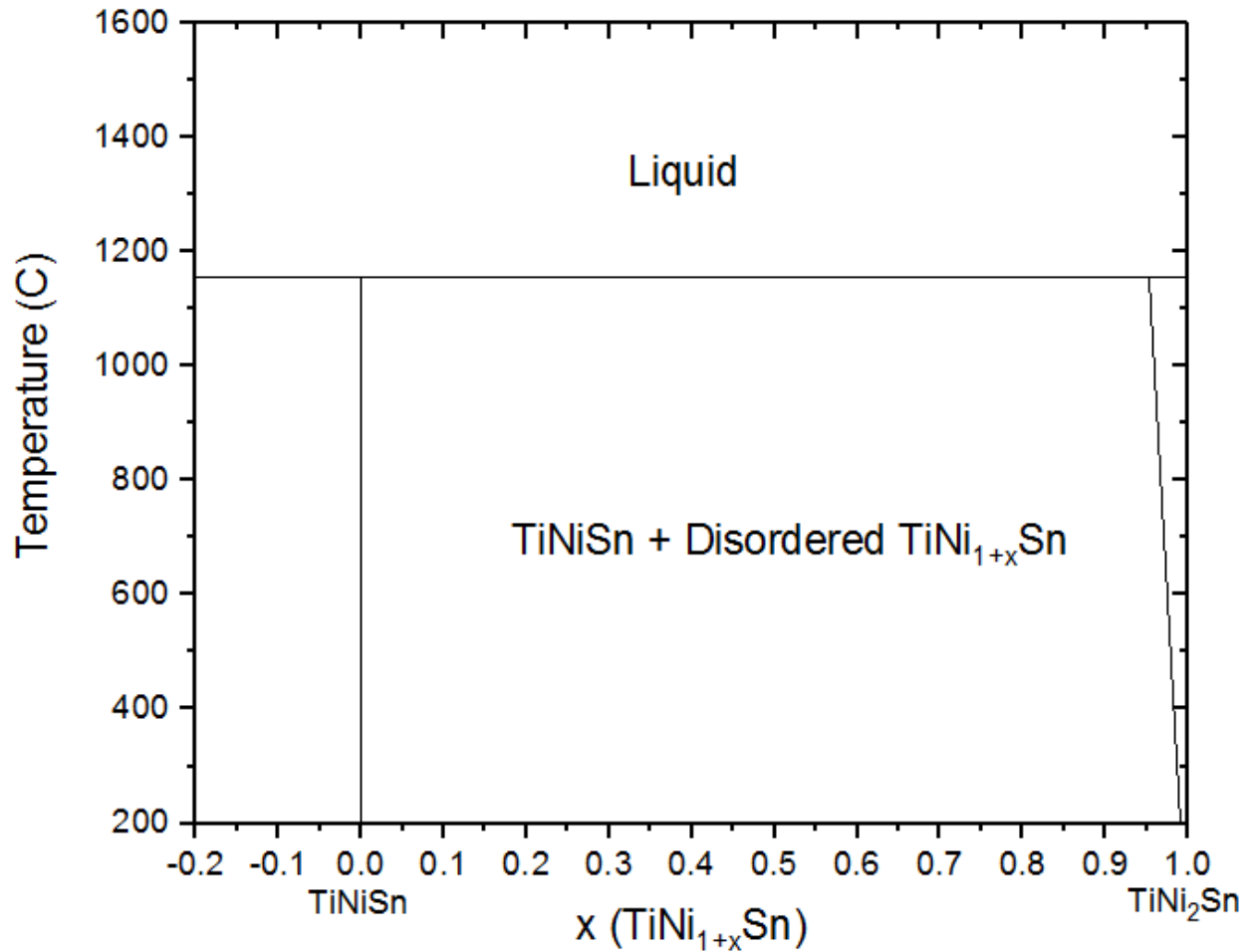


Figure 38: Binary phase diagram illustrating the stability of TiNiSn and disordered Ti(Vacancy)_{1-x}Ni_{1+x}Sn [48].

This phase diagram shows that a Ni-rich TiNiSn-based alloy will form a two-phase mixture of TiNiSn and disordered TiNi_{2-x}Sn, containing vacancy point defects in place of Ni atoms, during annealing. Due to the incomplete formation of TiNi₂Sn, it could be assumed that a small amount of Ni atoms will stay in the TiNiSn matrix as interstitial defects due to an insufficient driving force, based on the enthalpies of formation, for a completely ordered two-

phase compound. This would lead to the lattice parameters of TiNiSn and TiNi₂Sn not fully reaching their hypothetical standard values, even after three weeks of annealing.

5.8 Experimental Thermoelectric Properties of TiNiSn Alloy

Electrical conductivity, Seebeck coefficient, thermal conductivity, and figure of merit of TiNiSn alloy annealed for 3 weeks at 800 °C (condition #3) were measured using a ZT-Scanner instrument for simultaneous Harman-based measurements, illustrated in Figures 39 - 42 [42].

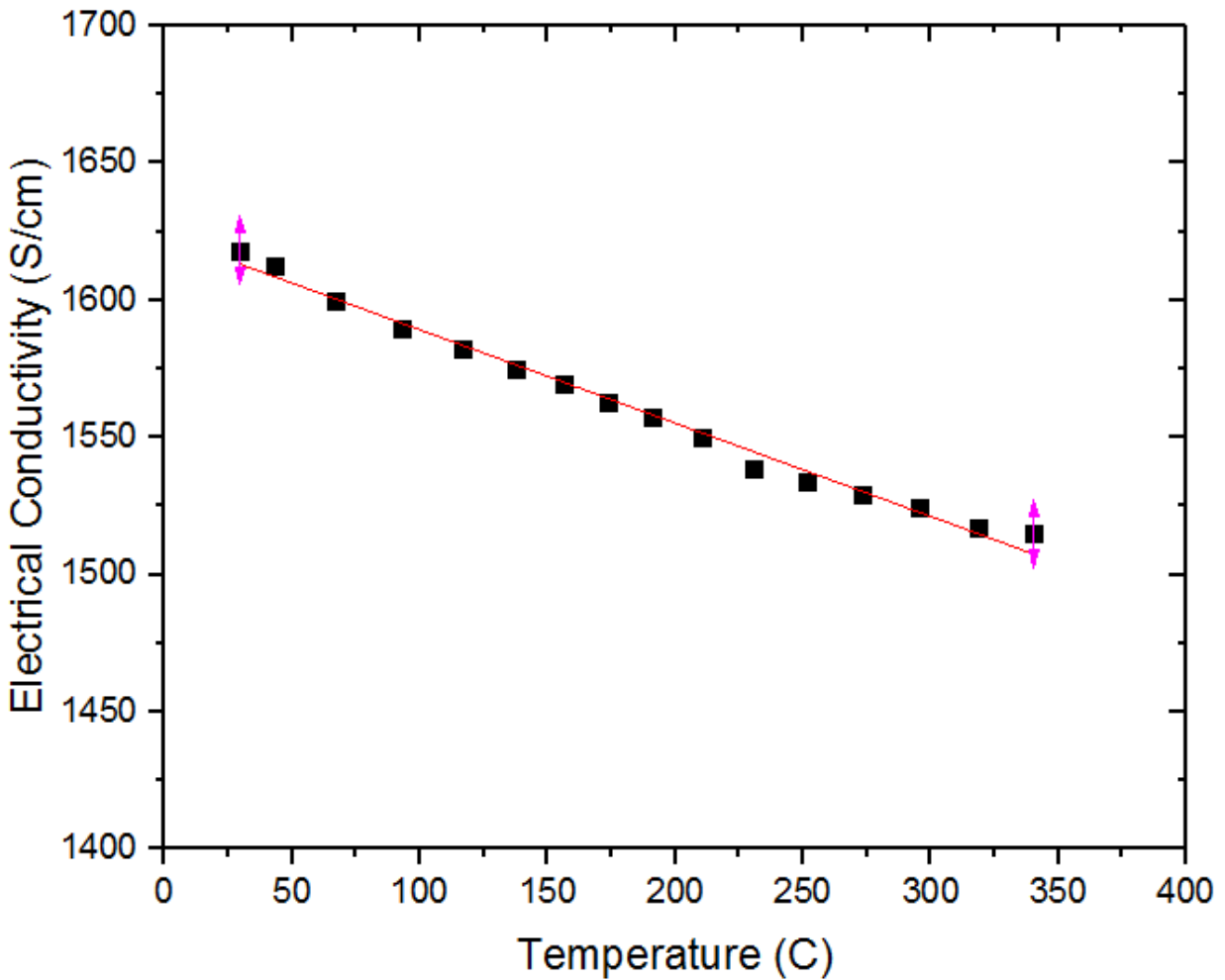


Figure 39: Experimental electrical conductivity of TiNiSn annealed for 3 weeks at 800 °C.

Electrical conductivity of the arc-melted and annealed (3 week at 800 °C) TiNiSn alloy was measured from 25 to 350 °C, shown in Figure 39. Conductivity decreased with increasing

temperature over this range. It was also found that this sample had a very large conductivity magnitude and compared well with other literature examples with high magnitudes from Figure 8. Such a high conductivity infers that this sample has metallic-like electronic structure and contains a small bandgap which enables electron promotion easily into the conduction band. Additionally, the lack of a densification process led to a comparatively larger grain size of the experimental sample which promoted less grain boundary defects, known to cause electron scattering and negatively affect conductivity.

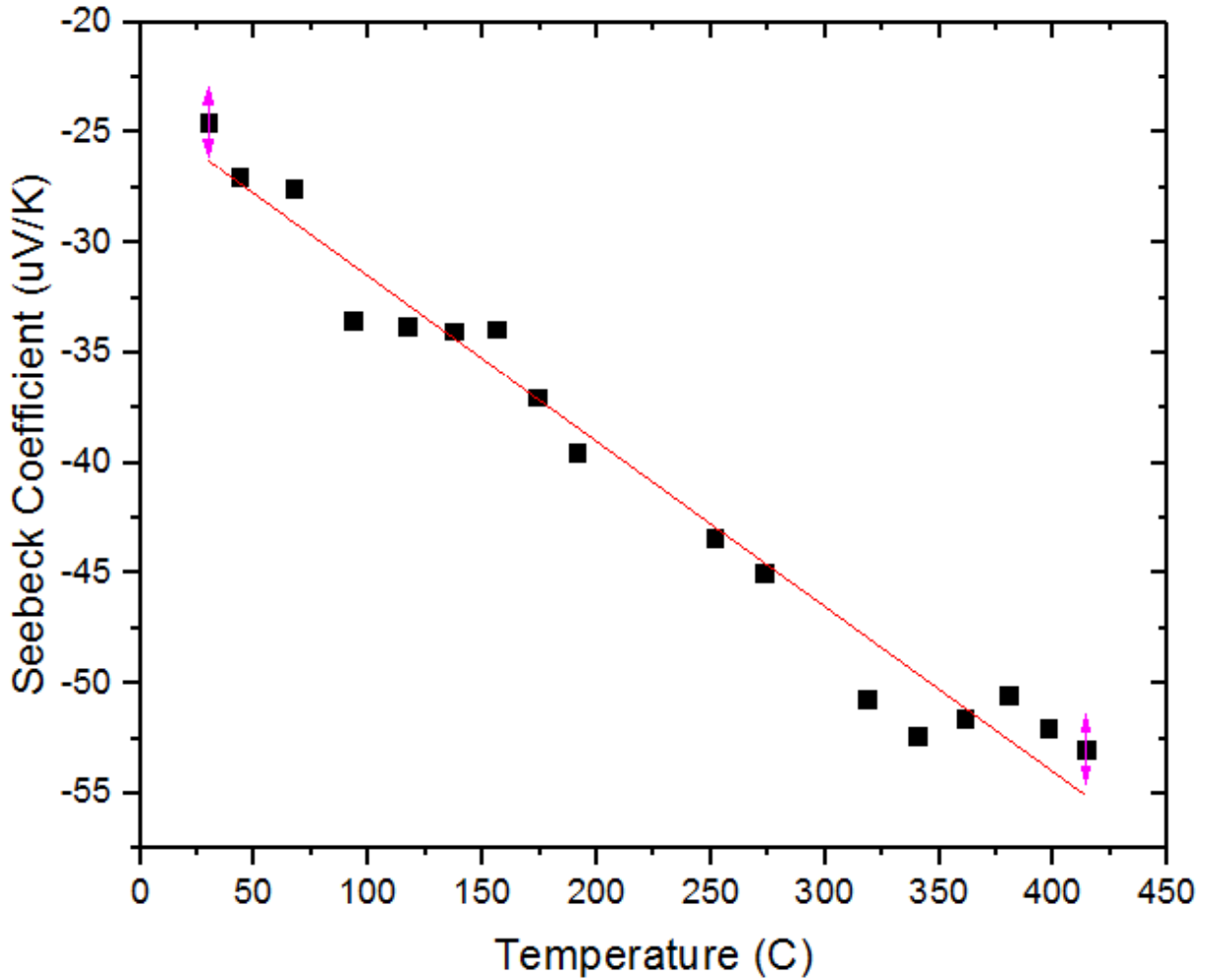


Figure 40: Experimental Seebeck coefficient of TiNiSn annealed for 3 weeks at 800 °C.

Seebeck coefficient of the TiNiSn alloy was measured from 25 to 450 °C in Figure 40, where the absolute magnitude was seen to increase linearly with temperature, which is the expected inverse behavior compared to electrical conductivity. Additionally, the absolute magnitude of Seebeck coefficient for the TiNiSn sample is near the minimum of the literature reviewed in Figure 9. This conforms to the reciprocal relationship established earlier where large electrical conductivities translate into small Seebeck coefficients based on the ease of opposite charge carrier promotion into the conduction band.

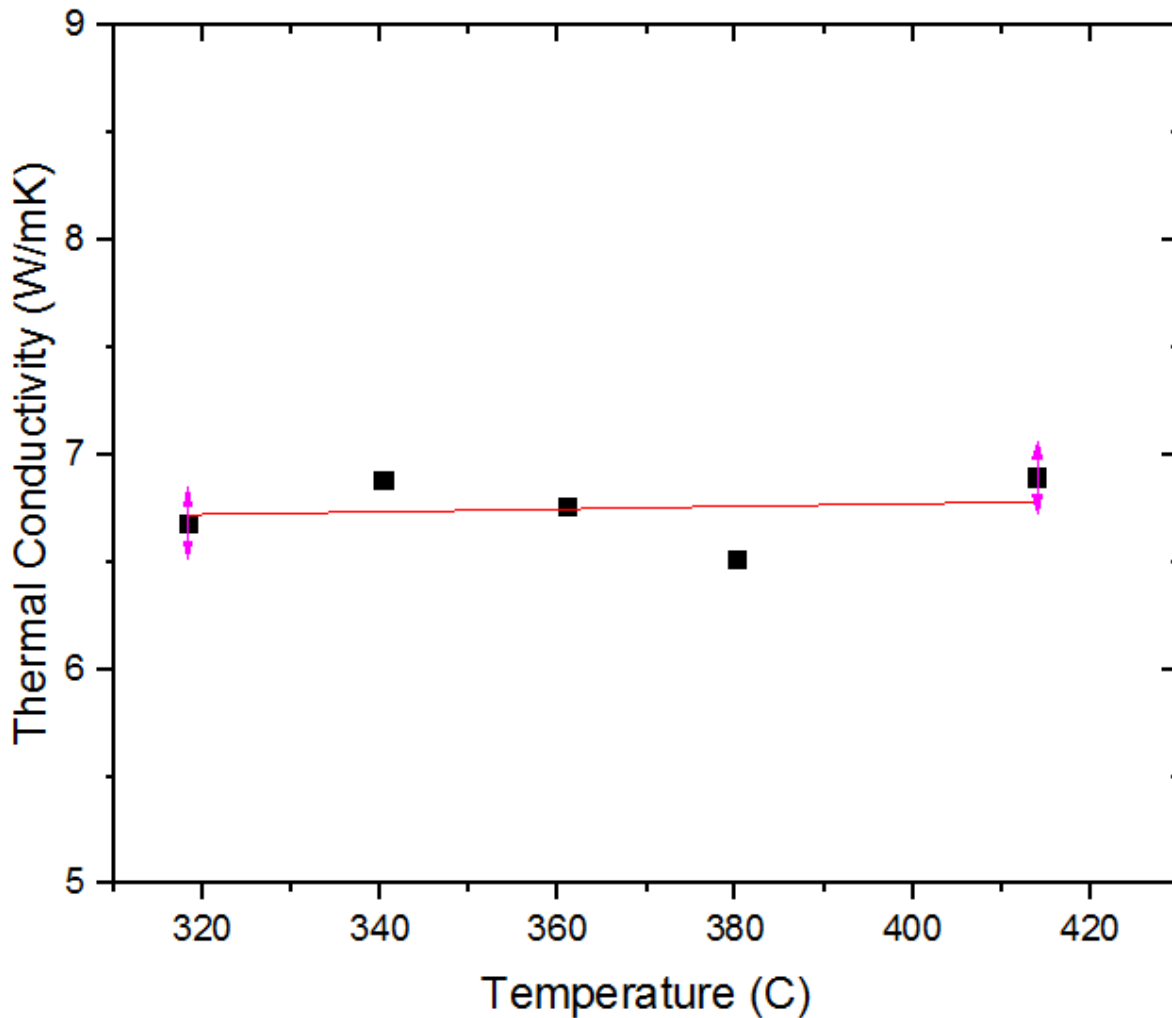


Figure 41: Experimental thermal conductivity of TiNiSn annealed for 3 weeks at 800 °C.

Thermal conductivity of TiNiSn was also measured as approximately 6.6 W/mK from 320 to 420 °C, shown in Figure 41. With varying synthesis method, literature values of TiNiSn alloys varied from 3 to 8 W/mK for the 25 to 425 °C range, in which this experiment falls into this range. Based on literature and this experiment, it can be determined that differences between synthesis method, morphology, or temperature for TiNiSn do not play a major role in significantly effecting thermal conductivity.

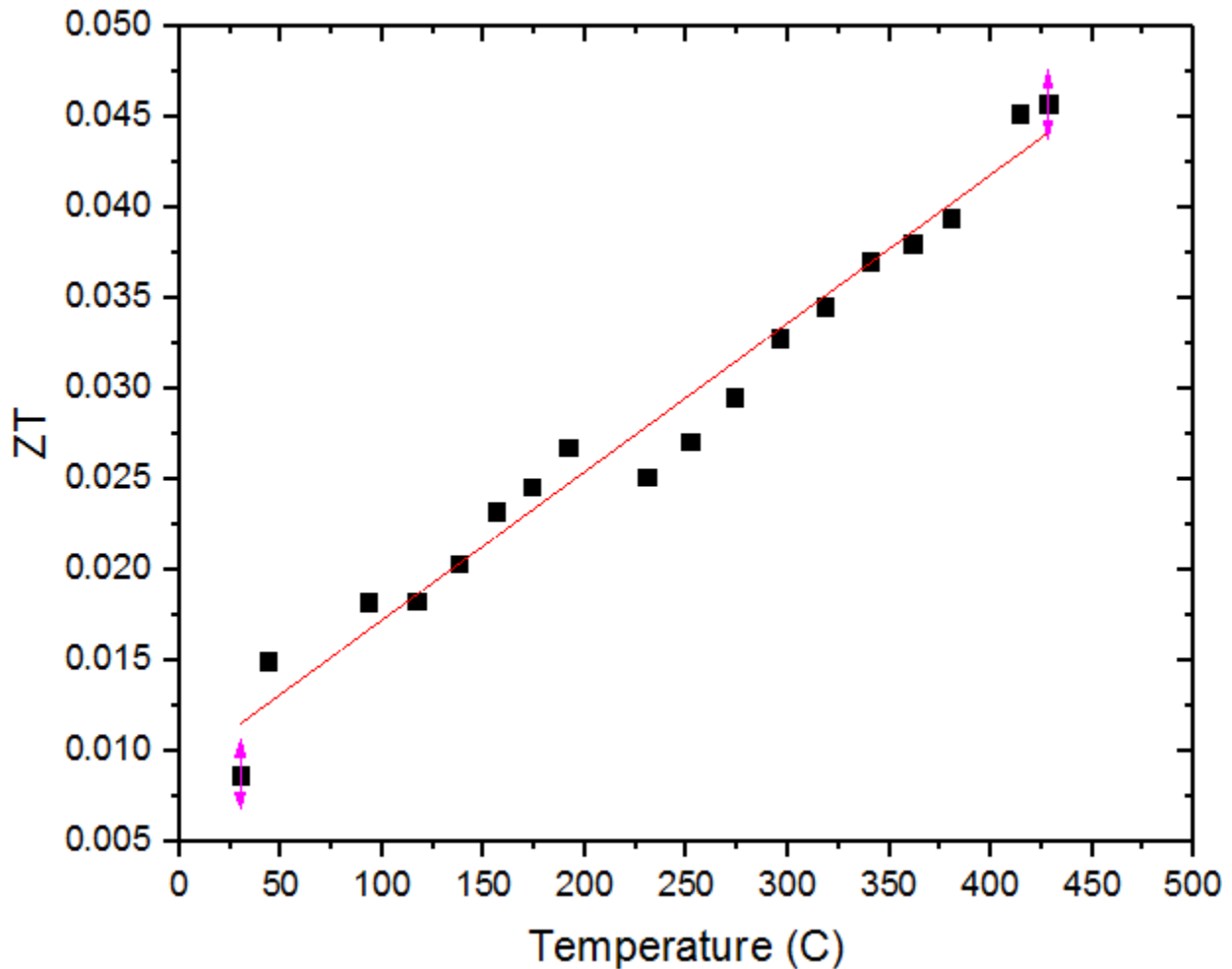


Figure 42: Calculated figure of merit of TiNiSn annealed for 3 weeks at 800 °C.

Using the measured electrical conductivity, Seebeck coefficient, and (extrapolated) thermal conductivity, the figure of merit, ZT, of arc-melted and annealed TiNiSn was calculated from 25 to 450 °C in Figure 42. ZT increased with temperature from 0.005 to 0.05, which is

approximately one order of magnitude lower than the reported ZT range of literature samples. This can be attributed to the experimental synthesis process used which enabled large grains and micro-porosity after annealing, leading to extreme cases of electrical conductivity and Seebeck coefficient in relation to literature.

5.9 Bandgap Calculation of Experimental TiNiSn

Increased thermal energy (i.e. temperature) gives rise to easier promotion of electrons to the conduction band. Bandgap of a semiconductor-like material can therefore be related to electrical conductivity using a temperature-dependent, Arrhenius-like relationship:

$$\sigma = \sigma_0 \exp\left(\frac{-E_g}{2kT}\right)$$

Where E_g is the activation energy, or bandgap, required for an electron to be promoted and k is the Boltzmann constant (8.617×10^{-5} eV/K) [49]. This equation can be changed into the form:

$$\ln(\sigma) = \ln(A) + \left(\frac{-E_g}{2k}\right)\left(\frac{1}{T}\right)$$

By plotting $\ln \sigma$ vs. $1/T$, the slope from a linear relationship, $E_g/2k$, can be used to determine the bandgap, shown below in Figure 43.

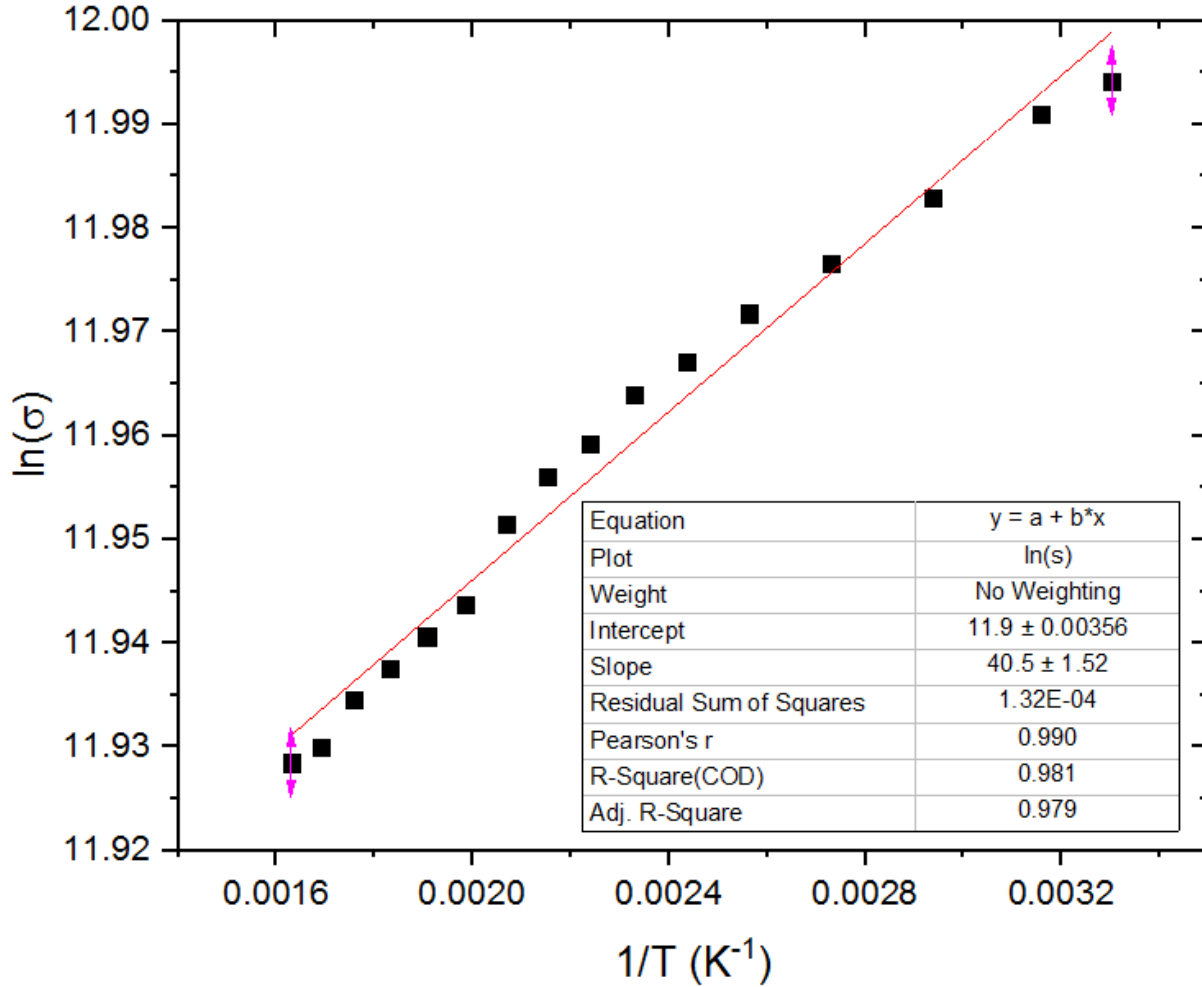


Figure 43: Linear relationship between $\ln(\sigma)$ and $1/T$ for bandgap determination.

The activation energy for conduction determined from the linear relationship in Figure 43 was calculated to be $-0.007 \pm 2.6 \times 10^{-4}$ eV. A bandgap of zero implies that the valence band and conduction band are overlapping, which is representative of a conductor or metal. Theoretical band gap of TiNiSn obtained using first-principle calculations is between 0.40 [45] and 0.51 eV [50], while the experimental bandgap in literature is generally much less (0.10 – 0.20 eV) [51]. Differences between theoretical and experimental bandgaps are attributed to the ease of atomic defects to occur with the natural vacancies within the TiNiSn unit cell [45, 52].

With increasing Ni-content, and therefore imperfections (higher interstitial defect concentration) within the TiNiSn crystal, the disordered TiNi_{2-x}Sn structure appears, causing bandgap and the semiconductor-like properties will diminish as the lattice parameter increases and the alloy becomes more metallic in nature [28]. It is theorized that the low/negative calculated bandgap of the alloy synthesized in this experiment emanates from interstitial defects within the crystal structure unit cell, which is in agreement with the lattice constant calculations. These defects are the primary contributor toward the diminished thermoelectric performance, exhibited by the low Seebeck coefficient magnitude, compared to other examples in literature.

CHAPTER 6 CONCLUSIONS

Samples of $\text{TiNi}_{1+x}\text{Sn}$ ($X = 0, 0.15$) were synthesized by an arc melting and annealing procedure and their phase distribution, thermoelectric properties, and lattice constant were studied as a function of annealing duration and temperature. Both compositions had an initial phase distribution consisting of many binary and ternary phases immediately after arc melting. For the TiNiSn ($X = 0$) alloy, pure TiNiSn phase with negligible impurity phases was synthesized after three weeks of annealing for $700 - 900$ °C. The $\text{TiNi}_{1.15}\text{Sn}$ alloy produced a two-phase mixture of TiNiSn and TiNi_2Sn after two weeks of annealing. Change in annealing temperature did not produce any significant change in phase equilibria for either composition. The electrical conductivity (1515 to 1618 S cm^{-1} from 30 to 340 °C), Seebeck coefficient (-25 to -53 $\mu\text{V K}^{-1}$ from 30 to 414 °C), thermal conductivity (6.68 to 6.90 $\text{W m}^{-1} \text{K}^{-1}$ from 318 to 414 °C), and thermoelectric figure of merit, ZT , (0.009 to 0.046 from 30 to 430 °C) of single phase TiNiSn was measured, implying metallic electronic conductance behavior. The calculated bandgap from the electrical conductivity was approximately 0 eV, inferring metallic behavior as well. Finally, lattice constants of TiNiSn and TiNi_2Sn phases differed from ICDD values (TiNiSn : $+0.04$ to 0.47% deviation, TiNi_2Sn : -0.09 to -0.40%) due to the ease of interstitial defects of Ni in the TiNiSn and TiNi_2Sn unit cells. Initial Ni interstitial defects after arc-melting are present due to the low energetic drive to diffuse and a quick solidification time. With an annealing heat treatment, a two-phase mixture of Ni-rich TiNiSn and Ni-deficient TiNi_2Sn was

produced, verified by the small differences in lattice constant from the ICDD standard. The primary differences between this study and literature were an exclusion of a densification synthesis step, a larger grain size, and significant porosity. When these factors are combined with the high electrical conductivity and low seebeck coefficient due to Ni-defects, this ultimately led to a less efficient thermoelectric TiNiSn alloy.

REFERENCES

- [1] "Independent Statistics & Analysis," U.S. Energy Information Administration, 1 April 2016. [Online]. Available: <https://www.eia.gov/tools/faqs/faq.cfm?id=427&t=3>. [Accessed 1 August 2016].
- [2] U.S. Department of Energy, "Waste Heat Recovery: Technology and Opportunities in U.S. Industry," BCS, Incorporated, 2008.
- [3] T. M. Tritt, M. G. Kanatzidis, G. D. Mahan and H. B. Lyon, "Thermoelectric Materials 1998 - The Next Generation Materials for Small-Scale Refrigeration and Power Generation Applications," *Materials Research Society*, vol. 545, 1998.
- [4] J. Yang and T. Caillat, "Thermoelectric Materials for Space and Automotive Power Generation," *MRS bulletin*, vol. 31, no. 03, pp. 224-229, 2006.
- [5] J. Yang and F. R. Stabler, "Automotive Applications of Thermoelectric Materials," *Journal of Electronic Materials*, vol. 38, no. 7, pp. 1245-1251, 2009.
- [6] U.S. Department of Energy, "TA 6.G: Direct Thermal Energy Conversion Materials, Devices, and Systems," 2015.
- [7] "What is the Seebeck Effect," innovateus, [Online]. Available: <http://www.innovateus.net/science/what-seebeck-effect>. [Accessed 4 August 2016].
- [8] S. H. Price, "The Peltier Effect and Thermoelectric Cooling," 26 March 2007. [Online]. Available: http://ffden-2.phys.uaf.edu/212_spring2007.web.dir/sedona_price/phys_212_webproj_peltier.html. [Accessed 4 August 2016].
- [9] H. W. Duckworth, in *Electricity and Magnetism*, New York, Holt, Rinehart and Winston, 1960, pp. 182-184.
- [10] V. Dhillon, "the physics of semi-conductors," 16 December 2013. [Online]. Available: http://www.vikdhillon.staff.shef.ac.uk/teaching/phy217/detectors/phy217_det_semiconductor.html. [Accessed 5 August 2016].

- [11] C. R. Nave, "Band Theory of Solids," Georgia State University, 2016. [Online]. Available: <http://hyperphysics.phy-astr.gsu.edu/hbase/solids/band.html>. [Accessed 5 August 2016].
- [12] G. Gottstein, *Physical Foundations of Materials Science*, Germany: Springer, 2004, pp. 439-443.
- [13] Ioffe Institute, "New Semiconductor Materials. Characteristics and Properties," Ioffe Physico-Technical Institute, 1998-2001. [Online]. Available: <http://www.ioffe.ru/SVA/NSM/>. [Accessed 5 August 2016].
- [14] J. M. Montes, F. G. Cuevas and J. Cintas, "Porosity effect of the electrical conductivity of sintered powder compacts," *Applied Physics A*, vol. 92, pp. 375-380, 2008.
- [15] L. Lu, Y. Shen, X. Chen, L. Qian and K. Lu, "Ultrahigh strength and high electrical conductivity in copper," *Science*, vol. 304, no. 5669, pp. 422-426, 2004.
- [16] University of Oslo Department of Physics, "Thermoelectrics," 28 November 2012. [Online]. Available: <http://www.mn.uio.no/fysikk/english/research/projects/bate/thermoelectricity/>. [Accessed 5 August 2016].
- [17] H.-S. Kim, Z. M. Gibbs, Y. Tang, H. Wang and G. J. Snyder, "Characterization of Lorenz number with Seebeck coefficient measurement," *APL Materials*, vol. 3, no. 041506, pp. 1-5, 2015.
- [18] Z. M. Gibbs, H. Kim, H. Wang and G. J. Snyder, "Band gap estimation from temperature dependent Seebeck measurement - Deviations from the $2e|S|_{\max}T_{\max}$ relation," *Applied Physics Letters*, vol. 106, no. 022112, 2015.
- [19] G. V. Chester and A. Thellung, "The Law of Wiedemann and Franz," *Proceedings of the Physical Society*, vol. 77, no. 5, pp. 1005-1013, 1961.
- [20] R. P. Chasmar and R. Stratton, "The Thermoelectric Figure of Merit and its Relation to Thermoelectric Generators," *Journal of Electronics and Control*, vol. 7, pp. 52-72, 1959.
- [21] R. M. Penner and L. E. Greene, "Solar Heat To Electric Power Generation," UC Irvine, 2010. [Online]. Available: <http://cfse.ps.uci.edu/research/solarheat.electric.shtml>. [Accessed 9 August 2016].
- [22] D. Crane, J. LaGrandeur, V. Jovovic, M. Ranalli, M. Adldinger, E. Poliquin, J. Dean, D. Kossakovski, B. Mazar and C. Maranville, "TEG On-Vehicle Performance and Model Validation and What It Means for Further TEG Development," *Journal of Electronic Materials*, vol. 42, no. 7, pp. 1582-1591, 2013.

- [23] W. Liu, Q. Jie, H. S. Kim and Z. Ren, "Current progress and future challenges in thermoelectric power generation: From materials to devices," *Acta Materialia*, vol. 87, pp. 357-376, 2015.
- [24] A. Schmitz, J. de Boor, K. Mull and E. Müller, "Tailoring the mechanical properties of thermoelectric lead telluride by alloying with non-doping calcium," *Journal of Materials Science*, vol. 51, no. 14, pp. 6933-6943, 2016.
- [25] I. Galanakis, Heusler Alloys: Properties, Growth, Applications, vol. 222, C. Felser and A. Hirohata, Eds., Springer, 2015, pp. 3-36.
- [26] Y. W. Chai and Y. Kimura, "Microstructure evolution of nanoprecipitates in half-Heusler TiNiSn alloys," *Acta Materialia*, vol. 61, no. 18, pp. 6684-6697, 2013.
- [27] J. Krez and B. Balke, "Thermoelectric Heusler Compounds," in *Heusler Alloys: Properties, Growth, Applications*, Springer, 2016, pp. 249-265.
- [28] M. Gürth, A. Grytsiv, J. Vrestal, V. V. Romaka, G. Giester, E. Bauer and P. Rogl, "On the constitution and thermodynamic modelling of the system Ti-Ni-Sn," *RSC Advances*, vol. 5, pp. 92270-92291, 2015.
- [29] J. E. Douglas, C. S. Birkel, N. Verma, V. M. Miller, M. Miao, G. D. Stucky, T. M. Pollock and R. Seshadri, "Phase stability and property evolution of biphasic Ti-Ni-Sn alloys for use in thermoelectric applications," *Journal of Applied Physics*, vol. 115, no. 043720, 2014.
- [30] L. Zhao, B. Zhang, W. Liu, H. Zhang and J. Li, "Enhanced thermoelectric properties of bismuth sulfide polycrystals prepared by mechanical alloying and spark plasma synthesis," *Journal of Solid State Chemistry*, vol. 181, no. 12, pp. 3278-3282, 2008.
- [31] M. Zou, J. Li, B. Du, D. Liu and T. Kita, "Fabrication and thermoelectric properties of fine-grained TiNiSn compounds," *Journal of Solid State Chemistry*, vol. 182, no. 11, pp. 3138-3142, 2009.
- [32] Z. A. Munir, U. Anselmi-Tamburini and M. Ohyanagi, "The effect of electric field and pressure on the synthesis and consolidation of materials: A review of the spark plasma sintering method," *J Mater Sci*, vol. 41, pp. 763-777, 2006.
- [33] Y. Gelbstein, N. Tal, A. Yarmek, Y. Rosenberg, M. P. Dariel, S. Ouardi, B. Balke, C. Felser and M. Köhne, "Thermoelectric properties of spark plasma sintered composites based on TiNiSn half-Heusler alloys," *Journal of Materials Research*, vol. 26, no. 15, pp. 1919-1924, 2011.
- [34] E. Fromm and H. Jehn, "Electromagnetic forces and power absorption in levitation melting," *Brit. J. Appl. Phys.*, vol. 16, pp. 653-663, 1965.

- [35] J. E. Douglas, C. S. Birkel, M. Miao, C. J. Torbet, G. D. Stucky, T. M. Pollock and R. Seshadri, "Enhanced thermoelectric properties of bulk TiNiSn via formation of a TiNi₂Sn second phase," *Applied Physics Letters*, vol. 101.18, no. 183902, 2012.
- [36] R. L. Coble, "Sintering Crystalline Solids. I. Intermediate and Final State Diffusion Models," *Journal of Applied Physics*, vol. 32, no. 5, pp. 787-792, 1961.
- [37] F. B. Swinkels, D. S. Wilkinson, E. Arzt and M. F. Ashby, "Mechanism of hot-isostatic pressing," *Acta metall.*, vol. 31, no. 11, pp. 1829-1840, 1983.
- [38] S. Kim, Y. Kimura and Y. Mishima, "High temperature thermoelectric properties of TiNiSn-based half-Heusler compounds," *Intermetallics*, vol. 15, no. 3, pp. 349-356, 2007.
- [39] C. S. Birkel, W. G. Zeier, J. E. Douglas, B. R. Lettiere, C. E. Mills, G. Seward, A. Birkel, M. L. Snedaker, Y. Zhang, G. J. Snyder, T. M. Pollock, R. Seshadri and G. D. Stucky, "Rapid Microwave Preparation of Thermoelectric TiNiSn and TiCoSb Half-Heusler Compounds," *Chemistry of Materials*, vol. 24, no. 13, pp. 2558-2565, 2012.
- [40] G. Gottstein, *Physical Foundations of Materials Science*, Berlin: Springer, 2004, pp. 303-356.
- [41] S. H. Avner, *Introduction to Physical Metallurgy*, Singapore: McGraw-Hill, 1974, pp. 129-145.
- [42] D. Vasilevskiy, J. M. Simard, R. A. Masut and S. Turenne, "System for Simultaneous Harman-Based Measurement of All Thermoelectric Properties, from 240 to 720 K, by Use of a Novel Calibration Procedure," *Journal of Electronic Materials*, vol. 44, no. 6, pp. 1733-1742, 2015.
- [43] "PDF 03-065-4322," ICDD, 2015.
- [44] "PDF 04-001-5022," ICDD, 2015.
- [45] H. Hazama, R. Asahi, M. Matsubara and T. Takeuchi, "Study of Electronic Structure and Defect Formation in Ti_{1-x}Ni_{1+x}Sn Half-Heusler Alloys," *Journal of Electronic Materials*, vol. 39, no. 9, pp. 1549-1553, 2010.
- [46] H. Hazama, M. Matsubara, R. Asahi and T. Takeuchi, "Improvement of thermoelectric properties for half-Heusler TiNiSn by interstitial Ni defects," *Journal of Applied Physics*, vol. 110, no. 063710, 2011.
- [47] J. E. Douglas, P. A. Chater, C. M. Brown, T. M. Pollock and R. Seshadri, "Nanoscale structural heterogeneity in Ni-rich half-Heusler TiNiSn," *Journal of Applied Physics*, vol. 116, no. 163514, 2014.

- [48] K. Kirievsky, Y. Gelbstein and D. Fuks, "Phase separation and antisite defects in the thermoelectric TiNiSn half-Heusler alloys," *Journal of Solid State Chemistry*, vol. 203, pp. 247-254, 2013.
- [49] D. Patidar, K. S. Rathore, N. S. Saxena, K. Sharma and T. P. Sharma, "Energy Band Gap and Conductivity Measurement of CdSe Thin Films," *Chalcogenide Letters*, vol. 5, no. 2, pp. 21-25, 2008.
- [50] S. Ögüt and K. M. Rabe, "Band gap and stability in the ternary intermetallic compounds NiSnM (M = Ti, Zr, Hf): A first-principles study," *Physical Review B*, vol. 51, no. 16, pp. 10443-10453, 1995.
- [51] T. Katayama, S. W. Kim, Y. Kimura and Y. Mishima, "The Effects of Quaternary Additions on Thermoelectric Properties of TiNiSn-Based Half-Heusler Alloys," *Journal of Electronic Materials*, vol. 32, no. 11, pp. 1160-1165, 2003.
- [52] V. A. Romaka, P. Rogl, V. V. Romaka, E. K. Hlil, Y. V. Stadnyk and S. M. Budgerak, "Features of a priori Heavy Doping of the n-TiNiSn Intermetallic Semiconductor," *Semiconductors*, vol. 45, no. 7, pp. 850-856, 2011.

APPENDIX A – Lattice Constants

Table 3: Calculated lattice constant (Å) from XRD for TiNiSn ternary phase with X = 0 after annealing at 800 °C.

<i>Days</i>	<i>Run 1</i>		<i>Run 2</i>		<i>Run 3</i>		a_{avg}	σ_a
	<i>d</i>	<i>a</i>	<i>d</i>	<i>a</i>	<i>d</i>	<i>a</i>		
0	2.104	5.950	2.106	5.958	2.104	5.952	5.953	0.004
7	2.099	5.937	2.098	5.935	2.100	5.941	5.938	0.003
14	2.097	5.930	2.097	5.932	2.097	5.932	5.932	0.001
21	2.098	5.935	2.099	5.937	2.098	5.934	5.935	0.002

Table 4: Calculated lattice constants (Å) from XRD for TiNiSn ternary phase at X=0.15 after annealing at 800 °C.

<i>Days</i>	<i>Run 1</i>		<i>Run 2</i>		<i>Run 3</i>		a_{avg}	σ_a
	<i>d</i>	<i>a</i>	<i>d</i>	<i>a</i>	<i>d</i>	<i>a</i>		
0	2.106	5.958	2.107	5.958	2.106	5.955	5.957	0.002
7	2.097	5.933	2.099	5.938	2.099	5.936	5.936	0.003
14	2.098	5.935	2.099	5.938	2.099	5.938	5.937	0.001
21	2.102	5.944	2.102	5.946	2.101	5.942	5.944	0.002

Table 5: Calculated lattice constants (\AA) from XRD for TiNi₂Sn ternary phase at X=0.15 after annealing at 800 °C.

	<i>Run 1</i>		<i>Run 2</i>		<i>Run 3</i>			
<i>Days</i>	<i>d</i>	<i>a</i>	<i>d</i>	<i>a</i>	<i>d</i>	<i>a</i>	<i>a_{avg}</i>	<i>σ_a</i>
0	2.145	6.067	2.148	6.075	2.147	6.073	6.072	0.004
7	2.153	6.089	2.148	6.077	2.155	6.095	6.087	0.009
14	2.153	6.089	2.153	6.089	2.153	6.089	6.089	0.000
21	2.150	6.082	2.150	6.081	2.153	6.089	6.084	0.005

Table 6: Calculated lattice constants (\AA) from XRD for TiNiSn ternary phase at X=0 after annealing for 14 days.

	<i>Run 1</i>		<i>Run 2</i>		<i>Run 3</i>			
<i>Temperature, °C</i>	<i>d</i>	<i>a</i>	<i>d</i>	<i>a</i>	<i>d</i>	<i>a</i>	<i>a_{avg}</i>	<i>σ_a</i>
700	2.096	5.930	2.098	5.934	2.097	5.932	5.932	0.002
800	2.097	5.930	2.097	5.932	2.097	5.932	5.932	0.001
900	2.096	5.928	2.098	5.934	2.098	5.934	5.932	0.003

Table 7: Calculated lattice constants (\AA) from XRD for TiNiSn ternary phase at X=0.15 after annealing for 14 days.

<i>Temperature, °C</i>	<i>Run 1</i>		<i>Run 2</i>		<i>Run 3</i>		a_{avg}	σ_a
	<i>d</i>	<i>a</i>	<i>d</i>	<i>a</i>	<i>d</i>	<i>a</i>		
700	2.100	5.940	2.100	5.941	2.101	5.942	5.941	0.001
800	2.098	5.935	2.099	5.938	2.099	5.938	5.937	0.001
900	2.100	5.941	2.101	5.942	2.101	5.942	5.942	0.001

Table 8: Calculated lattice constants (\AA) from XRD for TiNi₂Sn ternary phase at X=0.15 after annealing for 14 days.

<i>Temperature, °C</i>	<i>Run 1</i>		<i>Run 2</i>		<i>Run 3</i>		a_{avg}	σ_a
	<i>d</i>	<i>a</i>	<i>d</i>	<i>a</i>	<i>d</i>	<i>a</i>		
700	2.153	6.089	2.154	6.091	2.153	6.091	6.090	0.001
800	2.153	6.089	2.153	6.089	2.153	6.089	6.089	0.000
900	2.150	6.082	2.149	6.078	2.150	6.081	6.080	0.002

APPENDIX B – Final Elemental Compositions

Table 9: Elemental mole fraction from EDS for TiNiSn samples, shown in Figure 13.

<i>Condition #</i>	<i>Ti</i>	<i>Sn</i>	<i>Ni</i>
0	0.316	0.317	0.367
1	0.319	0.335	0.346
2	0.364	0.323	0.313
3	0.334	0.328	0.338
4	0.335	0.327	0.338
5	0.341	0.330	0.329

Table 10: Elemental mole fraction from EDS for TiNi_{1.15}Sn samples, shown in Figure 13.

<i>Condition #</i>	<i>Ti</i>	<i>Sn</i>	<i>Ni</i>
0	0.317	0.302	0.381
1	0.329	0.319	0.352
2	0.32	0.316	0.364
3	0.314	0.316	0.370
4	0.335	0.319	0.347
5	0.313	0.321	0.366